UNIVERSITÀ DEGLI STUDI DI NAPOLI "FEDERICO II"

FACOLTÀ DI INGEGNERIA

DIPARTIMENTO DI INGEGNERIA AEROSPAZIALE

Corso di Dottorato in Ingegneria Aerospaziale, Navale e della Qualità

XXV Ciclo

Multi-Step Estimation Approach for Aerospace Vehicle System Identification from Flight Data

Autore: Antonio Vitale

Tutor Aziendale: Dr. Federico Corraro

Tutor Universitario: Chiar.mo Prof. Michele Grassi

Coordinatore: Chiar.mo Prof. Luigi De Luca

To my wife Teresa
and my kids Gaetano and Anita
with love

ABSTRACT

System identification from flight data is an essential task in aerospace field, both for research and industrial activities. Indeed, ground based tests are not fully exhaustive of the vehicle behaviour and in-flight experimentation is often mandatory. In particular, there is a specific interest in obtaining vehicle model characteristics from flight data, in order to better understand theoretical predictions of physical phenomena, to validate wind-tunnel test results and to get more accurate and reliable mathematical models of the vehicle. The availability of these models is one of the critical items in order to guarantee the competitiveness of the aerospace industry, because it allows designing flight control law, evaluating vehicle performance and handling qualities, performing fault diagnosis and reconfiguration, developing high fidelity simulators, while reducing the flight test time and therefore reducing cost, risks and time to market of new products.

Although in the last decades several methodologies have been developed and many applications have been successful demonstrated, there are still open problems and challenges in system identification, mainly related to model complexity, high bandwidth requirements, constraints on flight test manoeuvres due to safety reason, dynamically unstable response, accurate characterisation of model uncertainties.

In the present work an innovative system identification methodology is described, which is suitable for dealing with some of the above listed challenges. The proposed methodology is implemented in the framework of a multi-step approach, which decomposes the complex starting identification problem in simplified sub-problems and allows specifying a suitable estimation technique compliant with each sub-problem objective, exploiting the advantage of both time-domain and frequency-domain methods. The straightforward combination of several estimation techniques brings to an identified model which is applicable in a wide frequency range. Furthermore, the proposed methodology is suitable to deal with problems where identification manoeuvres are minimised, indeed the identification can be executed only for the sub-model which is in fact identifiable. Another relevant peculiarity of the proposed approach concerns the exploitation of all the available a priori information and the rigorous management of all the uncertainties involved in the system identification procedure. As a result, a reliable, complete, and structured statistical characterisation of the identified model could be obtained.

Proposed methodology is applied in this thesis to determine the dynamical characteristics of rotorcraft vehicles and the transonic aerodynamic model of an atmospheric re-entry space demonstrator. Its effectiveness is demonstrated through numerical assessments, which enhanced the capability to catch the true values of the model parameters and to reproduce the phenomena of interest. Moreover, the application to actual flight data of the CIRA FTB1 re-entry demonstrator allowed to validate and refine the available pre-flight aerodynamic model of the vehicle, in terms of nominal values update and significant reduction on model uncertainties. These results justifies the importance of flight tests and, in particular, of system identification from flight data. The availability of an updated aerodynamic model represents a fundamental step for the development of the upgraded version of the Guidance, Navigation and Control system for the next missions of the same configuration, where the accuracy of estimates and the reliability of the model over an expanded flight envelope will be carefully analysed and assessed.

All the activities hereafter reported have been basically performed at the Italian Aerospace Research Centre (CIRA), where the author is the scientific coordinator of the Modelling and Simulation Laboratory, with the collaboration, advice and support of University "Federico II" that hosted the PhD period.

ACKNOWLEDGEMENTS

TABLE OF CONTENTS

1 PREFACE

1.1 List of Figures

1.2 List of Tables

1.3   List of Acronyms

ADB	Aerodynamic Database
ADC	Air Data Computer
ADS	Air Data System
AGARD	Advisory Group for Aerospace Research and Development
BFR	Body-fixed reference frame
CFD	Computational Fluid Dynamics
CIRA	Italian Aerospace Research Centre (Centro Italiano Ricerche Aerospaziali)
CoM	Centre of Mass
COTS	Commercial-Off-the-Shelf
CRB	Cramer–Rao Bound
DoF	Degrees of Freedom
DLR	German Aerospace Centre
DTFT	Dropped Transonic Flight Test
ECMWF	European Centre for Medium-Range Weather Forecasts
EKF	Extended Kalman Filter
FCS	Flight Control System
FTB	Flying Test Bed
FTR	Fourier Transform Regression
GM	Gauss-Markov
HYSY	Hydraulic System
IAS	Indicated Air Speed
IMU	Inertial Measurement Unit
LS	Least Square
MAG	Magnetometer
MIMO	Multi Input Multi Output
MLE	Maximum Likelihood Estimation
NASA	National Aeronautics and Space Administration
NED	North East Down reference frame
NLR	National Aerospace Laboratory of the Netherlands
RMS	Root Mean Square
RPM	Rounds Per Minute
TAEM	Terminal Area Energy Management

TAS	True Air Speed
TIC	Theil's Inequality Coefficient
UKF	Unscented Kalman Filter
USV	Unmanned Space Vehicle
UT	Unscented Transformation
WGS	World Geodetic System

1.4 List of Symbols

A	Regressor matrix
A_i, $B_{i,j}$	Unknown parameters related to main rotor flapping dynamics
a_0	Coning flap deflection [deg]
a_1	Longitudinal flap deflection [deg]
(a_x, a_y, a_z)	CoM acceleration components in body axes [m·s^{-2}, m·s^{-2}, m·s^{-2}]
b	Lateral aerodynamic reference length [m]
b_1	Lateral flap deflection [deg]
C	Vector of aerodynamic force and moment dimensionless coefficients
c	Longitudinal aerodynamic reference length [m]
$\mathbf{C_M} \equiv (C_l, C_m, C_n)$	Dimensionless aerodynamic moment coefficients in body axes
$\mathbf{C_F} \equiv (C_X, C_Y, C_Z)$	Dimensionless aerodynamic force coefficients in body axes
$\mathbf{D}_M$	Dispersion matrix
F	External forces vector [N]
F^i_{hk}	Static characteristic function
$\mathbf{F}_M$	Information matrix (also named Fisher matrix)
(F_X, F_Y, F_Z)	Components in Body axes of the external force [N, N, N]
g	Gravitational acceleration [m·s^{-2}]
G^i_{hk}	Rotational characteristic function
H	Sigmoidal function
I	Inertial matrix [kg·m^2]
(i_θ, i_ϕ)	Longitudinal and lateral tilt angles of the main rotor shaft with respect to the vehicle body axes [rad]
J	Cost function
$\mathbf{K}_F$	Kalman filter gain
M	External moments vector [N·m]
M	Mach number
(M_X, M_Y, M_Z)	Components in Body axes of the external moment [N·m, N·m, N·m]
m	Vehicle mass [kg]
n	Load factors
N_b	Number of blades of the main rotor
N_F	Dimension of filter state vector

N_T	Total number of measurement sampling available in the time frame [0, T]
(p, q, r)	Components of the angular velocity of the vehicle with respect to the NED reference frame, expressed in the Body reference frame [rad·s^{-1}, rad·s^{-1}, rad·s^{-1}]
P	Covariance matrix
P_s	Static pressure [Pa]
Q	Process noise covariance matrix
$\overline{q}$	Dynamic pressure [Pa]
R	Measurement noise covariance matrix
$\mathbf{R}_{NED}^{B}$	Rotation matrix from NED reference frame to BRF
$\mathbf{R}_{W}^{B}$	Rotation matrix from Wind reference frame to BRF
$\mathbf{R}_{S}^{r}$	Rotation matrix from Non-Rotating Shaft reference frame to Rotating Shaft reference frame
$\mathbf{R}_{B}^{S}$	Rotation matrix from BRF to Non-Rotating Shaft reference frame
S	Reference aerodynamic area [m^2]
t	time [s]
T_s	Static temperature [K]
U	Control input vector
(u, v, w)	Components of the CoM velocity with respect to the NED reference frame, expressed in the Body reference Frame [m·s^{-1}, m·s^{-1}, m·s^{-1}]
$(u_{wind}, v_{wind}, w_{wind})$	Components of wind speed in body axes [m·s^{-1}, m·s^{-1}, m·s^{-1}]
V	Centre of mass velocity [m·s^{-1}]
$\mathbf{V_{TAS}}$	True air speed [m·s^{-1}]
$\mathbf{V_{wind}}$	Wind speed [m·s^{-1}]
W_i	Weight related to ith sigma point
$\overline{\mathbf{x}}_{k}^{-}$	Predicted estimation of filter state vector at time t_k
$\overline{\mathbf{x}}_{k}^{+}$	Corrected estimation of filter state vector at time t_k
$\mathbf{X_V}$	Vehicle state vector
(X, Y, Z)	Generic system of coordinate axis, [m, m, m]
(x, y, z)	CoM position with respect to the NED reference frame [m, m, m]
(X_S, Y_S, Z_S)	Non-Rotating Shaft system of coordinate axis, [m, m, m]
(X_r, Y_r, Z_r)	Rotating Shaft system of coordinate axis, [m, m, m]
Y	Model output vector

$\mathbf{z}$	Flight measurement vector
α	Angle of attack [rad]
α_{ip}, β_{ip}	Characteristic parameters of second order periodic stochastic model
β	Sideslip angle [rad]
β_f	Flapping angle in multi-blade coordinates [rad]
β_{fi}	Flapping angle of the ith blade [rad]
β_0	Coning mode of the rotor [rad]
β_{1c}	Longitudinal tilt mode of the rotor in multi-blade coordinates [rad]
β_{1s}	Lateral tilt mode of the rotor in multi-blade coordinates [rad]
χ_i	Sigma point
Δt	Sampling time step [s]
δ_a	Ailerons deflection [deg]
δ_e	Elevons deflection [deg]
δ_r	Rudders deflection [deg]
λ	Unscented transformation scale factor
$\boldsymbol{\eta}$	Process noise vector
$\boldsymbol{\nu}$	Measurement noise vector
$\boldsymbol{\Theta}_\mathbf{p}$	Unknown model parameters
$\boldsymbol{\theta}^D$	Vector of unknown parameters related to aerodynamic drag coefficient
$\boldsymbol{\theta}_\mathbf{FX}$	Vector of unknown parameters of the rotorcraft model related to external force along X body axis
$\boldsymbol{\theta}_\mathbf{FY}$	Vector of unknown parameters of the rotorcraft model related to external force along Y body axis
$\boldsymbol{\theta}_\mathbf{FZ}$	Vector of unknown parameters of the rotorcraft model related to external force along Z body axis
$\boldsymbol{\theta}_\mathbf{MX}$	Vector of unknown parameters of the rotorcraft model related to external moment along X body axis
$\boldsymbol{\theta}_\mathbf{MY}$	Vector of unknown parameters of the rotorcraft model related to external moment along Y body axis
$\boldsymbol{\theta}_\mathbf{MZ}$	Vector of unknown parameters of the rotorcraft model related to external moment along Z body axis
$\boldsymbol{\theta}^L$	Vector of unknown parameters related to aerodynamic lift coefficient
$\boldsymbol{\theta}^l$	Vector of unknown parameters related to aerodynamic roll moment coefficient

$\boldsymbol{\theta}^m$	Vector of unknown parameters related to aerodynamic pitch moment coefficient
$\boldsymbol{\theta}^n$	Vector of unknown parameters related to aerodynamic yaw moment coefficient
$\boldsymbol{\theta}^Y$	Vector of unknown parameters related to aerodynamic lateral force coefficient
ϑ	Unknown aerodynamic gain
$(\vartheta_{1s}, \vartheta_{1c}, \vartheta_0, \vartheta_{TR})$	Rotorcraft commands: longitudinal cyclic [deg], lateral cyclic [deg], main rotor collective [deg] and tail rotor collective [deg], respectively
ψ	Blade Azimuth Angle [rad]
(Φ, Θ, Ψ)	BFR Euler angles (roll, pitch and yaw, respectively) with respect to NED reference frame [rad, rad, rad]
Ω_R	Main rotor angular speed [rad·s^{-1}]
$\boldsymbol{\omega}$	Vehicle angular velocity [rad·s^{-1}]
ω	Pulsation [Hz]

Subscript

0	Initial time
ADB	Pre-flight aerodynamic database
B	Body reference frame
BAS	Baseline
clean	Clean configuration
F	Filter
MC	Monte Carlo
NED	NED reference frame
sub	Subsonic
sup	Supersonic
W	Wind reference frame
∞	Free stream

Superscript

$\cdot$	Time derivative

^	Dimensionless
‾	Estimation
~	Fourier transform
a	Augmented
T	Transpose

2 INTRODUCTION

Flight data analyses are essential tasks in aerospace field, both for research and industrial activities. Indeed, ground based experiments are not fully exhaustive of the vehicle behaviour and in-flight experimentation is often mandatory. In particular, there is a specific interest in obtaining vehicle model characteristics from flight data, in order to better understand theoretical predictions of physical phenomena, to validate wind-tunnel test results and to get more accurate and reliable mathematical models of the vehicle. These objectives can be reached by performing vehicle's model identification from flight data. In fact, system identification is the process of determining an adequate mathematical model structure, usually containing differential equations, which includes unknown parameters to be estimated from flight measurements. The process comprehends not only the model postulating and parameters value determining, but also performing suitable flight tests, and gathering system inputs and outputs measurements [B1].

The availability of an accurate model of the vehicle is required to design flight control law, evaluate vehicle performance and handling qualities, perform fault diagnosis and reconfiguration, develop high fidelity simulators [B2], [B3], while reducing the flight test time and therefore reducing cost, risks and time to market of new products [B1]: hence system identification from flight data is one of the critical items in order to guarantee the competitiveness of the aerospace industry.

Flight vehicle system identification has been pursued by almost every organization dealing with the subject of atmospheric flight. The first attempt to apply parameters estimation principle to a flight vehicle was performed by Norton and Warner in 1919 [B4]. The scope of their investigation was the determination of aerodynamic parameters from various flight manoeuvres, flown at certain airspeeds. They utilized a basic idea of equating the lift force to the weight of the test aircraft and drag to the thrust force, assuming that weight and thrust were known for the test aircraft. The evolution of system identification applied to flight vehicles has been continuously expanding, developing several methodologies and applications. The major contributions in the last decades have resulted from NASA Dryden [B3] and Langley [B5] research centres, US army Aeroflight-dynamics at NASA Ames [B2], Institute of Flight Systems at DLR [B1], [B6], Technical University of Delft [B7] and NLR [B8], [B9].

2.1 Survey of System Identification Techniques from Flight Data

System Identification techniques can be classified according to several criteria, one of them being the domain in which the estimation is performed. Therefore we can distinguish between frequency domain and time domain techniques.

Frequency domain identification uses spectral methods to determine frequency responses between selected input and output pairs. The MIMO frequency response matrix constitutes a nonparametric model of the aircraft response, since it fully characterises the input-to-output behaviour without the need for defining a priori the model structure or determining the model parameters. An important by-product of this analysis is the coherence function, which provides key information about the frequency response accuracy [B2]. The nonparametric modelling results support many direct applications, including the design and analysis of flight control systems, stability margin determination, piloted handling-qualities analysis, and the validation and improvement of simulation models. When the dynamics contain nonlinear behaviour, the identified frequency response function represents the linear model that best approximates the nonlinear behaviour of the system [B10]. To obtain analytical model of linear input to output transfer function, least squares fitting techniques are used in the frequency domain to match the Bode plot of the frequency response. Since this fitting procedure is carried out after the frequency response is extracted, the order of the model transfer function can be carefully selected to avoid an over-parameterised model. The semi-logarithm frequency format of the Bode plot presentation, and subsequent transfer function fit, makes the identified models most accurate at mid and high frequency. The low frequency and steady state response prediction is generally not very good [B11]. Frequency domain techniques are also suitable for unstable model identification [B12]. In recent years, frequency domain estimation techniques, such as the Fourier Transform Regression (FTR) [B13], have been introduced to directly identify parametric model, too. They are also applicable to real-time estimation problems.

In the past decades however, with the increased computation capability of modern computers, the focus has changed from frequency domain to time domain analysis [B14]. Time domain identification first requires the definition of a model, which may be linear or nonlinear. Model formulation involves considerations about the model structure, selection of significant parameters and inclusion of important nonlinearities [B1]. Time domain techniques yield a MIMO model that is appropriate for application in stability and control analysis, simulation and

control system design. Moreover if the identified model is represented in the state space form, then stability and control derivatives are explicitly estimated. Time domain identification inherently weights low frequency dynamics much greater than high frequency ones [B11], for that reason the identified model is accurate at low and mid frequency.

Much of the published works on rotorcraft system identification, which is one of the application presented in this thesis, deals primarily with frequency domain methods [B2], although some relevant works used time-domain techniques, too [B15].

Concerning re-entry vehicle model identification, which is also faced in the thesis, the few published works exploit time domain methods. The Maximum Likelihood Estimation (MLE) [B16] technique, which is by far the most commonly used technique for estimating parameters from flight data, was applied to identify the model of the Space Shuttle [B17] and of the Phoenix re-entry demonstrator [B1], whereas the aerodynamics in subsonic regime of the Japanese ALFLEX re-entry demonstrator was identified by means of the Least Square (LS) estimation techniques [B18]. The latter was historically the first method used for parameters estimation, introduced more than 200 years ago [B19]. In recent years, for aerospace applications, system identification has been also formulated and solved in the time domain as filtering problem [B20], [B21], [B22], [B23], [B24], mainly using the Kalman filter.

The above mentioned techniques, that is, FTR, MLE, LS, together with a nonlinear implementation of the Kalman filter, are detailed described in section 4.2. A multitude of other different techniques for flight vehicle model identification are proposed in the literature [B1]. They are not discussed here for the sake of brevity. The huge amount of publications on system identification confirms that it is still a challenging topic for research activities.

Whatever the applied estimation methodology is, if parametric identification is performed, then the Quad-M approach can be used to carry out the identification process. This approach, proposed some years ago by DLR [B1], is represented in Figure 2.1. It is related to the four basic elements of system identification, namely:

- Manoeuvres: to design a suitable flight test, selecting the manoeuvres that provide maximum sensitivities of the vehicle reactions with respect to the unknown parameters

[B25], [B26]. A basic and obvious principle is "if a particular dynamic characteristic is not in the data, don't expect to be able to identify it in the model" [B1].

- Measurements: to acquire, by means of flight test instrumentations [B27], both the input controls and the vehicle's reaction on the given input; the quality of the overall identification process is strongly influenced by the accuracy of the measurement equipment [B28].

- Models: to define a suitable parametric model structure, based on physical consideration and other a priori information (such as wind tunnel tests for the aerodynamic model), and to select the identifiable parameters. The model selection plays a central role in the flight vehicle system identification [B1].

- Methods: to develop or select one or more methodologies in order to fulfil model identification. Every estimation method has particular advantages and disadvantages over the others. There is no direct answer to the best method, its choice is dictated by the engineering anticipation of the problem.
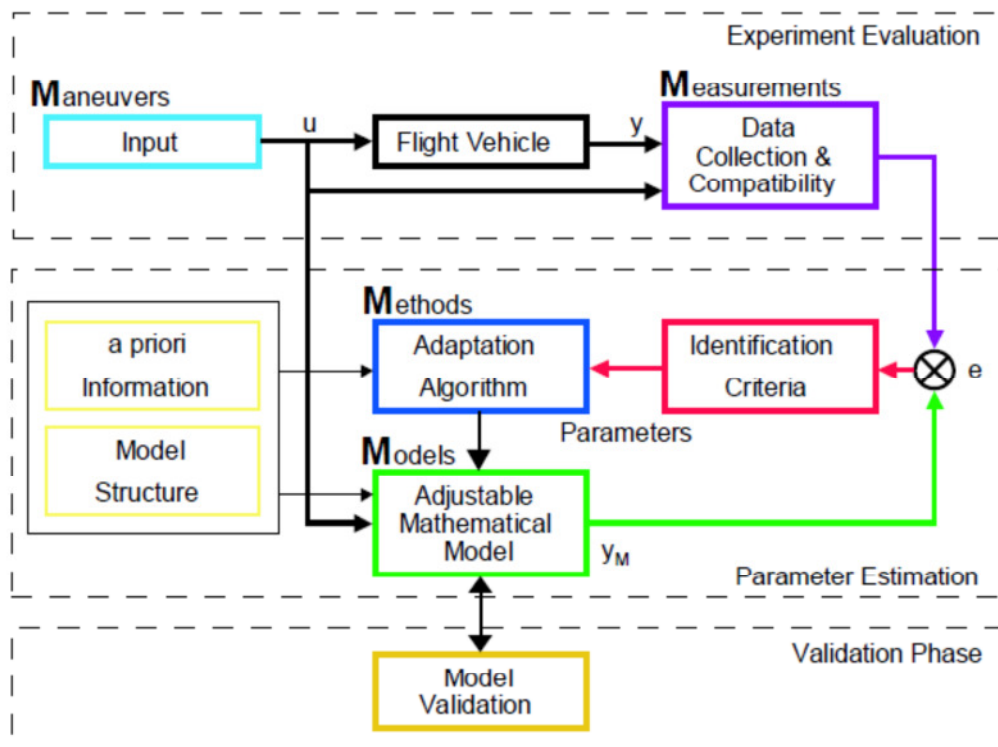
Figure 2.1 – Schematic representation of the Quad-M identification approach [B1]

Finally, the identified model must be validated in order to test whether it is sufficiently accurate for the intended purposes of its use. The last two points listed above, as well as the model validation, are dealt with in this thesis.

2.2   Motivation and Objectives of the Work

Although many methodologies have been developed and applications have been successful demonstrated, there are still special problems and challenges in system identification. Prime areas of research are related to:

- Model complexity, [B1], [B29], [B30], which could be needed to describe flexible aircraft behaviour, highly nonlinear coupled multi-body vehicle, nonlinear aerodynamic effects.

- High bandwidth requirements [B2], related to coupled slow flight mechanics scales and faster aero-elastic ones.

- Constraints on flight test manoeuvres due to safety reason [AR1], [AR2], which are typical of re-entry missions and vehicle in ground proximity, or low manoeuvrable vehicles [AR3].

- Dynamically unstable response [B15], which characterises rotorcraft vehicles.

- Accurate characterisation of model uncertainties [B29], [B31], which is needed to design robust flight control system and evaluate vehicle performance in off-nominal conditions [AR4], [AR5], [AR6].

Other challenges are not strictly related to system identification, but they affect the quality of identification results. An example is the reduced signal to noise ratio in the flight data, which is generally exhibited by rotorcraft data gathered at low speed or hover [B1], [B2]. The problem often affects the air data measurements [B29], and can be solved through specific advances on data acquisition and processing systems [AR7].

The objective of this thesis is to develop an innovative identification approach suitable for dealing with some of the above listed system identification challenges. To this end, the following problems are formulated and solved: system identification strategy definition, model structure

selection, flight path reconstruction and optimal vehicle state estimation based on the available sensors set, parameters estimation, model uncertainty characterisation. The proposed approach is applied to:

- Model Identification of an atmospheric re-entry space demonstrator in the TAEM trajectory phase, that is in subsonic, transonic and low supersonic regimes, without performing specific identification manoeuvres.
- Identification of highly nonlinear coupled multi-body rotorcraft model, applicable for simulation in wide frequency range.

The thesis also presents the results of numerical assessment of the proposed system identification methodology, performed through simulated flight data, and its application to actual flight data of the CIRA FTB1 re-entry demonstrator.

All the activities hereafter reported have been basically performed at the Italian Aerospace Research Centre (CIRA), where the author is the scientific coordinator of the Modelling and Simulation Laboratory, with the collaboration, advice and support of University "Federico II" that hosted the PhD period.

2.3 Structure of the Thesis

The thesis is structured as follows. After the present introductive chapter, which also includes a short overview on system identification state of the art, the system identification problem is mathematically formulated in chapter 3. The proposed system identification methodology is presented in chapter 4, where the applied estimation techniques are also described. Chapters 5 and 6 describe the customisation of the proposed methodology to two specific aerospace applications, that is, the aerodynamic model identification of an atmospheric re-entry space demonstrator and the identification of a rotorcraft model. Next, the identification methodology is validated through simulated data for the selected applications, and the numerical assessment results are presented and discussed in chapter 7. Finally, the aerodynamic model identification from actual flight data of the CIRA FTB1 re-entry demonstrator is reported in chapter 8. The last chapter contains a summary of results and some concluding remarks.

3 PROBLEM FORMULATION

In the context of system identification, vehicle dynamics can be represented as a stochastic process in continuous state space form. The time evolution of the vehicle state vector $\mathbf{X_V}$, together with the time history of output vector $\mathbf{Y}$, could be computed through the follows equations [B1]

Eq. 1 $\qquad \dot{\mathbf{X}}_{\mathbf{V}}(t) = f\left(\mathbf{X}_{\mathbf{V}}(t), \mathbf{U}(t), \mathbf{\Theta}_{\mathbf{p}}, \mathbf{\eta}(t)\right)$

Eq. 2 $\qquad \mathbf{X}_{\mathbf{V}}(t_0) = \mathbf{X}_{\mathbf{V0}}$

Eq. 3 $\qquad \mathbf{Y}(t) = h(\mathbf{X}_{\mathbf{V}}(t), \mathbf{v}(t))$

where f and h are generic nonlinear real-valued vectorial functions; t_0 and $\mathbf{X_{V0}}$ are the initial mission time and the initial state vector value, respectively; $\mathbf{U}$ is the control input vector, the elements of which depend on the vehicle type and configuration; $\mathbf{\eta}$ and $\mathbf{v}$ are process and measurement noises, respectively, which are usually assumed zero mean Gaussian noise characterised by their covariance matrices; finally $\mathbf{\Theta_p}$ is a vector of model parameters, which are unknown or affected by wide uncertainties.

Unknown or uncertain parameters could concern several characteristics of the vehicle such as, for example, mass, inertia, centre of mass location, or be related to specific dynamic phenomena of vehicle subsystems, as it happens for the flap and lag dynamics of the rotor blade of a rotorcraft. However, the most relevant model uncertainty is usually associated to aerodynamic phenomena. Indeed, aerodynamic parameters are evaluated before flight using CFD analysis and wind tunnel tests, but their values are affected by wide uncertainty ranges (especially in some flight regimes, such as transonic), which should be reduced analysing flight data. In some cases the structure of the model is not completely known, too, and it should be determined and validated through the flight tests.

System Identification aims at determining the structure of the model represented by the function f, if it is unknown, and the values of the parameters $\mathbf{\Theta_p}$ (parameters estimation) from the analysis of measurements of control inputs $\mathbf{U}$ and model outputs $\mathbf{Y}$, which are gathered in flight during

specific tests. Although the state vector is not mentioned explicitly, it appears in the above description implicitly, because the outputs are function of internal system state variables.

4 PROPOSED SYSTEM IDENTIFICATION METHODOLOGY

4.1 Multi-Step Estimation Approach

In order to solve the system identification problem in the cases of high model complexity and/or strong constraints on flight test manoeuvres, the application of the classical decomposition approach is proposed in this thesis [AR1]. The starting complex problem is decomposed in simplified sub-problems, with the aim to firstly isolate the part of the model which is affected by uncertain structure and/or parameters (the uncertain sub-model), next to estimate the input and output of this sub-model, and finally to perform system identification limited to the uncertain sub-model. This strategy is denoted as multi-step estimation approach for system identification and the estimation sub-problems are denoted as identification steps.

Further than reducing the complexity of the starting problem, the main advantages of the proposed approach are:

- It permits to select a suitable estimation methodology to solve each sub-problem, exploiting in such a way the advantages of several identification techniques, which can also work in different domain (time and frequency) [AR8].

- It is specifically suited to deal with problems where identification manoeuvres are minimised and dynamic excitation is poor, indeed the identification can be carried out only for the sub-model which is in fact identifiable [AR9].

Moreover, if the estimation uncertainties related to each identification step are rigorously managed and propagated, then a reliable, complete, and structured statistical characterisation of the identified model could be obtained [AR1].

The proposed multi-step approach could be mathematically detailed starting from and Eq. 1 to Eq. 3, which could be re-arranged in the following form

Eq. 4 $\quad \dot{\mathbf{X}}_{V1}(t) = f_1(\mathbf{X}_{V1}(t), \mathbf{C}(t), \boldsymbol{\eta_1}(t))$

Eq. 5 $\quad \dot{\mathbf{X}}_{V2}(t) = f_2(\mathbf{X}_{V1}(t), \mathbf{X}_{V2}(t), \mathbf{U}(t), \boldsymbol{\Theta}_{P1} \boldsymbol{\eta_2}(t))$

Eq. 6 $\quad \mathbf{X_V}(t_0) = \begin{bmatrix} \mathbf{X_{V1}}(t_0) \\ \mathbf{X_{V2}}(t_0) \end{bmatrix} = \mathbf{X_{V0}}$

Eq. 7 $\quad \mathbf{Y}(t) = h(\mathbf{X_{V1}}(t), \mathbf{X_{V2}}(t), \mathbf{v}(t))$

Eq. 8 $\quad \mathbf{C}(t) = l(\mathbf{X_{V1}}(t), \mathbf{X_{V2}}(t), \mathbf{U}(t), \mathbf{\Theta_{P2}})$

The vehicle state vector $\mathbf{X_V}$ is partitioned in two subset: $\mathbf{X_{V1}}$ and $\mathbf{X_{V2}}$. The dynamics of $\mathbf{X_{V1}}$ are defined by equations which don't include explicitly any unknown parameters, but they depend on unknown input vector $\mathbf{C}$. Typically, these equations derive from the principles of the Newtonian mechanics for the description of the body motion. Instead, the $\mathbf{X_{V2}}$ dynamic equations are affected by the unknown parameters $\mathbf{\Theta_{P1}}$. Eq. 8 represents a static sub-model, whose output $\mathbf{C}$ depends on the complete vehicle state vector, the control inputs and the uncertain parameters $\mathbf{\Theta_{P2}}$. Usually $\mathbf{C}$ is the vector of force and moment acting on the vehicle, the unknowns are force and moment parameters, and the nonlinear real-valued function l translates the force and moment model. The uncertain sub-model is then defined by Eq. 5 and Eq. 8.

In the present thesis the models of two different vehicles are identified. In the case of re-entry space vehicle, the identification only concerns the aerodynamic model, whose structure (represented by the function l) should be defined before performing the estimation of the unknown parameters. Therefore the subset $\mathbf{X_{V2}}$ is empty, as well as $\mathbf{\Theta_{P1}}$, and Eq. 5 is not taken into account. On the contrary, the rotorcraft model also includes uncertain parameters which affect the dynamics of the vehicle states. Therefore the complete formulation of Eq. 4 to Eq. 8 should be adopted and both the structure of functions f_2 and l should be determined before carrying out the evaluation of the parameters. In both cases, the definition or selection of a suitable model structure is an extremely important stage in the overall system identification approach from flight data. A good model, at the minimum, would give insight into the applicable physical phenomena, explain the force and moment coefficients on the trajectory, have a capability to predict the vehicle behaviour in the neighbourhood of the flight trajectory. The model structure selection is of course strictly related to the vehicle characteristic but it also depends on the model purpose. For example, rotorcraft is generally modelled for simulation purposes as nonlinear multi-body dynamic system, characterised by strong coupling between the dynamics of rotor blades and air flow passing through the rotor (inflow) with those of the

fuselage, control system and engine [B2]. Therefore, rotorcraft simulation models are built by means of a component by component detailed physical description of main rotor, tail rotor, fuselage, empennage-horizontal stabilizer and fin-vertical stabilizer. In contrast to the simulation approach, FCS design and validation requires simplified global model, characterised by lumped parameters, and details about individual rotorcraft components are not relevant.

After the determination of the models structures, which are based on physical principles and engineering judgement, the multi-step approach performs system identification through the following steps, in each of them the best suitable estimation methodology is applied:

- Flight path reconstruction, that is, the estimation of the time histories of state vector subset X_{V1} and of the input $\mathbf{C}$ along the whole flight test. This step is carried out without using Eq. 5 and Eq. 8, and it usually also allows obtaining information on some relevant environmental parameters (such as wind velocity, air temperature and pressure) experienced by the vehicle during the flight test. The flight path reconstruction is formulated as a nonlinear filtering problem and solved by using the Unscented Kalman Filter methodology.

- Estimation of the identifiable parameters values and of the related estimation uncertainties. It is executed using the models represented by Eq. 5 and Eq. 8, the flight measurements and the results of the flight path reconstruction. This step could be further decomposed in sub-steps, which carry out independent estimation of unknown parameters related to state vehicle dynamics and/or of each component of the force model. Several estimation methodologies can be applied to this step, working both in the time domain (such as Unscented Kalman Filter, Maximum Likelihood Estimation, Least Squares) and in the frequency domain (such as Fourier Transform Regression).

4.2 Estimation Techniques

As discussed in chapter 2, several estimation methodologies are reported in the literature for aeronautical applications. Few of them have been selected to be integrated in the proposed multi-step approach for the examined system identification problems. A short description of these methodologies is presented in this section, further details could be found in the listed references.

4.2.1 Unscented Kalman Filter

The Unscented Kalman Filter (UKF) [B32] is a nonlinear filtering technique based on the concept of Unscented Transformation (UT), which is an analytical method for propagating a probability distribution through a nonlinear transformation. In more details, the UT allows estimating the mean and the covariance of the nonlinear function by computing the weighted mean and covariance of a discrete set of function values, obtained propagating through the function a set of points (named sigma points) deterministically chosen in the domain of the function. Based on the UT, the UKF provides at least second order accurate evaluations of the first two statistical moments of the unknowns [B32], enabling a complete and structured statistical characterisation of the estimated variables and leading to a reliable evaluation of the uncertainties on the estimations. In recent times, UKF has been proposed as a valid alternative to the Extended Kalman Filter (EKF) for nonlinear filtering, receiving great attention in navigation, parameter estimation, and dual estimation problems [B24]. Like all the Kalman filters, the UKF performs the estimation in two sequential phases: first a dynamic model is used for time propagation of the estimation (prediction phase); next, at each time step, the available flight measurements are compared with the prediction (that is, the dynamic model outputs) to refine the estimation (correction phase).

The UT is applied in the prediction phase of the filter. Several implementation of the UT, and consequently of the UKF are available in the literature [B24], [B33], [B34], characterised by different number of sigma points, weights and free parameters, with the aim to limit the spreading of sigma points in high order systems, or to provide improved accuracy in the evaluation of higher order statistical moments. In this thesis a non-augmented version of the UKF algorithm with additive process and measurements noises is adopted [AR8], [AR9], [AR10], in order to reduce the number of sigma points [B24]. Different formulations are not expected to introduce significant improvements in the algorithm performance, while they could increase the computational effort. In order to avoid losing information on the effect of process noise on the outputs, two concatenated Unscented Transformations are performed during the prediction phase, to account for the propagation throughout the nonlinear process and measurement equations [B35], [B36].

Since flight measurements are available at discrete sampling time, the discrete formulation of the UKF is used. The process and measurement noises are assumed additive. The generic filter model is expressed through

Eq. 9 $\quad \mathbf{X}_F\left(t_{k+1}\right) = f_F\left(\mathbf{X}_F\left(t_k\right), \mathbf{U}_F\left(t_k\right)\right) + \boldsymbol{\eta}$

Eq. 10 $\quad \mathbf{Y}_F\left(t_k\right) = h_F\left(\mathbf{X}_F\left(t_k\right)\right) + \boldsymbol{\nu}$

where $\mathbf{X}_F$, $\mathbf{Y}_F$ and $\mathbf{U}_F$ are filter model state vector, output vector and input vector, respectively, and t_k is discrete time, $\boldsymbol{\eta}$ and $\boldsymbol{\nu}$ are process and measurement noises. Eq. 9 represent the dynamic equation, whereas Eq. 10 is the output or measurement equation. The filter state vector should include all the unknowns to be estimated. Let's denote with N_F the filter state vector dimension, with $\bar{\mathbf{x}}_k^-$ the predicted estimation based on the filter model, and with $\bar{\mathbf{x}}_k^+$ the estimation corrected by using the available measurements.

The prediction phase is composed of the following steps [AR11], [B36]:

1P. First generation of $2*N_F+1$ sigma points ($\boldsymbol{\chi}_i$) and related weights (W_i), based on the current estimate of the filter state vector and related covariance matrix

Eq. 11
$$\begin{aligned} \boldsymbol{\chi}_i &= \bar{\mathbf{x}}_{k-1}^+ + \left(\sqrt{\lambda \mathbf{P}_{k-1}^+}\right)_i; & i &= 1..N_F \\ \boldsymbol{\chi}_0 &= \bar{\mathbf{x}}_{k-1}^+; \\ \boldsymbol{\chi}_{i+N_a} &= \bar{\mathbf{x}}_{k-1}^+ - \left(\sqrt{\lambda \mathbf{P}_{k-1}^+}\right)_i; & i &= 1..N_F \end{aligned}$$

Eq. 12
$$\begin{aligned} W_0 &= 1 - \frac{N_F}{\lambda} \\ W_i &= \frac{1-W_0}{2N_F} = \frac{1}{2\lambda}; & i &= 1..2N_F \end{aligned}$$

where $\mathbf{P}_{k-1}^+$ is the available estimation of the state vector covariance matrix and λ is a scale factor which can be tuned to capture high order statistics.

2P. Propagation of the sigma points through the process equation

Eq. 13 $\quad \mathbf{X}_{Fi} = f_F\left(\boldsymbol{\chi}_i, \mathbf{U}_F\left(t_k\right)\right)$

3P. Prediction of the filter state vector, computed as weighted mean of the propagated sigma points

Eq. 14 $\qquad \bar{\mathbf{x}}_k^- = \sum_i W_i \cdot \mathbf{X}_{Fi}$

4P. Prediction of the covariance matrix of the filter state. It is computed as summation of two terms: the first one is the weighted variance of the propagated sigma points (step 2P) with respect to the state vector prediction (step 3P); the second term is the process noise covariance matrix $\mathbf{Q}$ (because additive process noise is assumed)

Eq. 15 $\qquad \mathbf{P}_k^- = \sum_i W_i \cdot \left(\mathbf{X}_{Fi} - \bar{\mathbf{x}}_k^- \right) \cdot \left(\mathbf{X}_{Fi} - \bar{\mathbf{x}}_k^- \right)^T + \mathbf{Q}$

5P. Second generation of sigma points and related weights, based on the predicted filter state vector (step 3P) and covariance matrix (step 4P). Eq. 11 and Eq. 12 are used again where $\bar{x}_{k-1}^+$ and $\mathbf{P}_{k-1}^+$ are replaced by $\bar{x}_k^-$ and $\mathbf{P}_k^-$, respectively.

6P. Propagation of the sigma points through the measurement equation

Eq. 16 $\qquad \mathbf{Y}_{Fi} = h_F \left(\boldsymbol{\chi}_i \right)$

7P. Prediction of the filter outputs, computed as weighted mean of the propagated sigma points

Eq. 17 $\qquad \bar{\mathbf{y}}_k = \sum_i W_i \cdot \mathbf{Y}_{Fi}$

8P. Prediction of the covariance matrix of the filter outputs. It is computed as summation of two terms: the first one is the weighted variance of the propagated sigma points (step 6P) with respect to the filter outputs prediction (step 7P); the second term is the measurements noise covariance matrix $\mathbf{R}$ (because additive measurement noise is assumed)

Eq. 18 $\qquad \mathbf{P}_{yy} = \sum_i W_i \cdot \left(\mathbf{Y}_{Fi} - \bar{\mathbf{y}}_k \right) \cdot \left(\mathbf{Y}_{Fi} - \bar{\mathbf{y}}_k \right)^T + \mathbf{R}$

9P. Prediction of the state-output correlation matrix. It is computed as the weighted deviation of the sigma points propagated through the process equation (step 2P) with respect to the

predicted state vector (step 3P) times the deviation of the sigma points propagated through the measurement equation (step 6P) with respect to the predicted filter outputs (step 7P)

Eq. 19 $\qquad \mathbf{P}_{xy} = \sum_i W_i \cdot \left(\mathbf{X}_{Fi} - \overline{\mathbf{x}}_k^- \right) \cdot \left(\mathbf{Y}_{Fi} - \overline{\mathbf{y}}_k \right)^T$

The correction phase requires in input the measurements, denoted by $\mathbf{z}_k$, and is carried out as follows:

1C. Computation of the Kalman filter gain. It depends on filter output covariance matrix (step 8P) and state-output correlation matrix (step 9P)

Eq. 20 $\qquad \mathbf{K}_F = \mathbf{P}_{xy} \cdot inv\left(\mathbf{P}_{yy} \right)$

2C. Correction of the predicted filter state

Eq. 21 $\qquad \overline{\mathbf{x}}_k^+ = \overline{\mathbf{x}}_k^- + \mathbf{K}_F \cdot \left(\mathbf{z}_k - \overline{\mathbf{y}}_k \right)$

3C. Correction of the predicted covariance matrix of the filter state.

Eq. 22 $\qquad \mathbf{P}_k^+ = \mathbf{P}_k^- - \mathbf{K}_F \cdot \mathbf{P}_{yy} \cdot \mathbf{K}_F^T$

It is worthy to note that since the unknown to be estimated by the UKF should be included in the filter state vector $\mathbf{X_F}$, then the dynamics of each unknown should be modelled and included into the model filter represented by Eq. 9.

4.2.2 Least Square

The Least Square (LS) technique provides the estimation of unknown parameters by minimizing the sum of square differences between measured data and corresponding values provided by the parametric model, which includes the uncertainties [B37]. The technique has the advantage to be simple and it doesn't require a starting guess for the unknowns. Moreover, measured data gathered during different tests can be concatenated and managed as a unique data set to be processed.

LS is usually applied in the time domain to static model which are linear with respect to the unknown parameters, such as

$$\text{Eq. 23} \quad \mathbf{Z} = \mathbf{A} \cdot \mathbf{\Theta}$$

In the above relation, the terms of the regressors matrix **A** and the vector **Z** are directly measured at different time instants or computed from the available measurements. If the examined time frame is long enough, the number of equations is bigger than the number of the unknowns, and the least square solution can be computed in closed form by minimisation of following cost function:

$$\text{Eq. 24} \quad J = \frac{1}{2}(\mathbf{Z} - \mathbf{A\Theta})^{T}(\mathbf{Z} - \mathbf{A\Theta})$$

The estimation which minimize *J* is

$$\text{Eq. 25} \quad \hat{\mathbf{\Theta}} = \left[\mathbf{A}^{T}\mathbf{A}\right]^{-1}\left(\mathbf{A}^{T}\mathbf{Z}\right)$$

4.2.3 Maximum Likelihood Estimation

Maximum Likelihood Estimation (MLE) [B38] is by far the most commonly used technique for estimating parameters from flight data. It works in the time domain and computes the values of the unknowns by optimising a cost function called likelihood function.

Let's represent the stochastic dynamic system through Eq. 1 to Eq. 3. Therefore **Y** is the predicted output vector of the model. Let's further denote with **z** a vector of independent flight measurements gathered in N_T time instants t_k. The likelihood function is defined as [B31]

$$\text{Eq. 26} \quad L(\mathbf{\Theta_P}) = \text{Pr}(\mathbf{Y} \mid \mathbf{\Theta_P})_{Y=z}$$

where $\text{Pr}(\mathbf{Y} \mid \mathbf{\Theta_P})_{Y=z}$ is the probability to realize the measurements vector **z** given the value $\mathbf{\Theta_P}$ of the parameters vector. The likelihood function is thus a measurement of the relative plausibility of the measured response for each value of $\mathbf{\Theta_P}$; it represents the probability density function of the measured variables and not of the parameters. The maximum likelihood estimate $\overline{\mathbf{\Theta}}_{\mathbf{P}\,MLE}$ of $\mathbf{\Theta_P}$ is defined as the value of the parameters that maximizes the likelihood function; in other words it is the value that makes the measured data most plausible.

Because of the exponential nature of many density functions, the logarithm of the likelihood function is generally optimized, obtaining the same optimal solution, that is [B1]

$$\text{Eq. 27} \quad \overline{\mathbf{\Theta}}_{\mathbf{P}\,MLE} = \arg\left\{ \min_{\mathbf{\Theta}_{\mathbf{P}}}\left[-\log(L(\mathbf{\Theta}_{\mathbf{P}}))\right]\right\}$$

In order to apply this estimation method to the vehicle dynamic model, the likelihood function should be defined. Let's assume the following hypotheses:

- the input U to the system is generated independently of the system output;
- the measurement error is Gaussian, zero mean, statistically independent at different time instant, and characterised by known covariance matrix **R;**
- the process noise is negligible.

In these hypotheses the following cost function should be minimised to obtain the MLE estimation [B1]

$$\text{Eq. 28} \quad J(\mathbf{\Theta}_{\mathbf{P}}) = \frac{1}{2}\sum_{k=1}^{N_T}\left[\mathbf{z}(t_k) - \mathbf{Y}(t_k)\right]^T \mathbf{R}^{-1}\left[\mathbf{z}(t_k) - \mathbf{Y}(t_k)\right]$$

There isn't any closed form analytical solution for this optimisation problem, therefore numerical methods are applied. Usually, second order optimisation methods are exploited to solve unconstrained or constrained optimisation problem [B1], [B16], [B31]. An initial guess for the unknown parameters is requested in this formulation to perform the estimation.

Concerning the accuracy of the estimation, the MLE is asymptotically efficient in the sense of achieving the Cramer-Rao lower bound. It follows that the parameter error covariance matrix is given by the inverse of the Fisher information matrix $\mathbf{F}_M$ [B1]

$$\text{Eq. 29} \quad \mathbf{D}_M = \mathbf{F}_M^{-1} = \left[\sum_{i=1}^{N_T}\left[\left(\frac{\partial \mathbf{Y}(t_i)}{\partial \mathbf{\Theta}_P}\right)^T \mathbf{R}^{-1}\left(\frac{\partial \mathbf{Y}(t_i)}{\partial \mathbf{\Theta}_P}\right)\right]\right]^{-1}$$

$$\text{Eq. 30} \quad \sigma_{\vartheta_k} = \sqrt{D_M(k,k)}$$

Eq. 31
$$\rho_{\vartheta_k \vartheta_j} = \frac{D_M(k,j)}{\sqrt{D_M(k,k) \cdot D_M(j,j)}}$$

where $\vartheta_k \in \boldsymbol{\Theta}_\mathbf{P}$, $D_M(k,j)$ is the generic element of the dispersion matrix $\mathbf{D}_M$, σ_{ϑ_k} and $\rho_{\vartheta_k \vartheta_j}$ are the standard deviations and the correlation coefficients of the estimates, respectively.

It is worthy to note that the MLE could be applied also if the process noise is not negligible or the measurement noise covariance matrix is not known [B1].

4.2.4 Fourier Transform Regression

The Fourier Transform Regression (FTR) is a LS technique in the frequency domain, which estimates the unknown parameters by minimizing the sum of square differences between measured data and corresponding values provided by the model on a selected frequency range [B39]. This technique is applicable to linear and nonlinear system, however linear in the unknown parameters, and to static and dynamic model. It doesn't require an initial guess for the unknown parameters. Moreover, since the method is not iterative and the estimation computational burden is low, it can also be used for real-time estimation [B40], [B41], [B42].

The technique is based on the optimisation of a cost function defined in the frequency domain. Let's define the finite Fourier transform of generic a signal s(t)

Eq. 32
$$\tilde{s}(\omega) \equiv \int_o^T s(t)e^{-j\omega t}dt \approx \Delta t \sum_{i=0}^{N_T-1} s_i e^{-j\omega t_i}$$

where Δt is the sampling time step and the subscript i denotes that the variable is evaluated at the time $i \cdot \Delta t$. Next N_T is the total number of measurements available in the examined time interval, that is [0, T], and ω denotes the pulsation. The discrete Fourier transform is defined as:

Eq. 33
$$S(\omega) \equiv \sum_{i=0}^{N_T-1} s_i e^{-j\omega t_i}$$

and consequently

Eq. 34
$$\tilde{s}(\omega) \approx S(\omega)\Delta t$$

If a nonlinear dynamic system is linear with respect to the unknown parameters Θ, then it can be put in the form

Eq. 35 $\qquad \dot{\mathbf{X}} = f_1(\mathbf{X}, \mathbf{U}) \cdot \Theta + f_2(\mathbf{X}, \mathbf{U})$

If the measurements of input vector $\mathbf{U}$ and state vector $\mathbf{X}$ are available, then the function f_1 and f_2 can also be considered as measurements (because they are computed from the measurements), and their discrete Fourier transforms $\mathbf{F}_1(\omega)$ and $\mathbf{F}_2(\omega)$ can be computed. Equations (33) can be rewritten in the frequency domain

Eq. 36 $\qquad j\omega \mathbf{X}(\omega) = \mathbf{F}_1(\omega) \cdot \Theta + \mathbf{F}_2(\omega)$

and rearranged in the form

Eq. 37 $\qquad \mathbf{Z}(\omega) = \mathbf{A}(\omega) \cdot \Theta$

The above relation can be sampled in the frequency domain in n_f points, with $n_z \cdot n_f > N_P$, where n_z and N_P are $\mathbf{Z}$ and Θ dimensions, respectively. In such a way, a linear system in $n_z \cdot n_f$ equations and N_P unknowns is obtained, which can be solved in closed form by minimisation of following cost function (least square solution):

Eq. 38 $\qquad J = \dfrac{1}{2}(\mathbf{Z} - \mathbf{A}\Theta)^T (\mathbf{Z} - \mathbf{A}\Theta)$

where apex T indicates a complex conjugate transpose. The estimation which minimize J is

Eq. 39 $\qquad \overline{\Theta} = \left[\mathrm{Re}(\mathbf{A}^T \mathbf{A})\right]^{-1} \mathrm{Re}(\mathbf{A}^T \mathbf{Z})$

where Re indicates the real part of the complex number.

An estimation error associated to $\overline{\Theta}$ can be also computed through

Eq. 40 $\qquad \mathrm{cov}(\overline{\Theta}) \equiv E\left\{(\overline{\Theta} - \Theta)(\overline{\Theta} - \Theta)^T\right\} = \dfrac{1}{(n_f - N_p)}\left[(\mathbf{Z} - \mathbf{A}\overline{\Theta})^T (\mathbf{Z} - \mathbf{A}\overline{\Theta})\right]\left[\mathrm{Re}(\mathbf{A}^T \mathbf{A})\right]^{-1}$

4.3 Validation Methodologies

Model validation is the process of testing whether the identified model is sufficiently accurate for the intended purposes. Several methodologies can be used for the validation of the model obtained from the analysis of flight data, and for the assessment of the applied estimation strategy and techniques.

It is useful to distinguish if model identification is carried out analysing simulated flight data or actual flight measurements. In the first case the validation can be executed in order to assess the identification techniques performance, whereas in the latter case the validation is needed to evaluate the identified model quality.

If simulated flight data are examined, the true values of the model parameters and the true time histories of model inputs and outputs are known. The assessment of the estimation techniques can be carried out as follows:

1.V   The estimated parameters are compared with their true values, in order to check the estimation accuracy [AR12].

2.V   The estimation error on the parameters (that is, the difference between estimated and true parameters) is compared with the uncertainty on the estimation, which is also provided by the identification process, in order to ascertain the reliability of the estimation stochastic characterisation [AR12].

3.V   The flight mission is simulated twice using the true model and the identified one. In both cases the same inputs and disturbances are provided to the models. The outputs obtained in these two simulations are compared in order to evaluate the capability of the identified model to reproduce the phenomena of interest and to provide an acceptable fit in experiments [AR13]. The comparison can be qualitative or quantitative and it can be performed along the flight trajectory whose data are used for the identification of the model (internal validation) or along a different trajectory (cross validation or acid test) [B1], [B43]. The Theil's Inequality Coefficient (TIC) is used as quantitative metric for the comparison [AR2]. The TIC associated to the ith model outputs is defined as [B1]

Eq. 41

$$TIC = \frac{\sqrt{\frac{1}{N}\sum_{k=1}^{N}[z_i(t_k) - Y_i(t_k)]^2}}{\sqrt{\frac{1}{N}\sum_{k=1}^{N}[z_i(t_k)]^2} + \sqrt{\frac{1}{N}\sum_{k=1}^{N}[Y_i(t_k)]^2}}$$

where Y_i is the identified model output and z_i the corresponding flight measurement (actual or simulated). TIC = 0 means perfect fit, whereas TIC = 1 corresponds to the case of maximum inequality. In general TIC < 0.25 indicates that the identified model is able to fit the experiments.

In case of actual flight data, the true values of parameters are not known, and the methodology 3.V is only applicable for the validation of the model, where the identified model outputs are compared with the corresponding flight measurements.

5 MODEL IDENTIFICATION OF AN ATMOSPHERIC RE-ENTRY SPACE VEHICLE

In this chapter the methodology proposed in this thesis is customized for model identification of an atmospheric re-entry space vehicle in the terminal area energy management (TAEM) phase of its trajectory, that is in subsonic, transonic and supersonic flight regimes. System identification of an atmospheric re-entry space vehicle is very challenging, mainly because [AR9]:

1. The aerodynamic behaviour of a re-entry vehicle is characterised by a complex flow structure that produces significant variations of all the aerodynamic coefficients depending on Mach number and angle of attack. It makes it difficult to model the vehicle aerodynamics, particularly in transonic regime.

2. Experimental re-entry missions are typically performed once, providing a limited number of suitable data, and the experiment cannot be repeated in the short term. Therefore, it is difficult to refine the vehicle model in the whole flight envelope.

3. Due to safety constraints, manoeuvres specifically suited to the purpose of model identification are minimised.

The first two issues call for structured parametric models, where the flow field characteristics in the regimes of interest are represented with adequate accuracy. The selected aerodynamic model structure [AR14] is presented in section 5.1.2. On the other hand, the third topic above requires that as much as possible information is extracted from low excitation inputs, and it is thus related to the effectiveness of the adopted identification methodology. The multi-step estimation approach is well suited to face this problem due to its peculiarities.

5.1 Flight Mechanics Model

The classical laws of Newtonian mechanics are utilized to describe the equations of motion of a re-entry vehicle, assuming the following hypotheses:

1. The vehicle is a 6 degrees of freedom rigid body.

2. The mass and inertia of the vehicle are constant.

Since we are only interested to the last phase of the re-entry (from Mach number about 3 to 0.2), which lasts few minutes, the hypothesis of flat non-rotating Earth could also be assumed and the NED reference system could be considered an inertial reference frame. The motion of a rigid body with respect to an inertial reference frame is characterised by the action of external forces and moments. Both the equations of motion and the expression of the external forces and moments are described in this section.

5.1.1 Rigid Body Dynamics

The equations of motion can be established in terms of translational and angular accelerations as a consequence of the external forces **F** and moments **M** applied to the centre of mass, by applying Newton's Second Law

Eq. 42 $\mathbf{F} = m\dot{\mathbf{V}}$

Eq. 43 $\mathbf{M} = \mathbf{I}\dot{\boldsymbol{\omega}}$

where m and **I** are the vehicle mass and inertial matrix, respectively; **V** is the CoM inertial velocity and **ω** the vehicle angular velocity with respect to the inertial reference frame.

The dynamic equations can be written in Body reference frame as follows

Eq. 44 $\mathbf{F} = m\dot{\mathbf{V}} + \boldsymbol{\omega} \times m\dot{\mathbf{V}}$

Eq. 45 $\mathbf{M} = \mathbf{I}\dot{\boldsymbol{\omega}} + \boldsymbol{\omega} \times \mathbf{I}\boldsymbol{\omega}$

Let's introduce the following symbols:

- u, v, w are the components of the velocity **V** with respect to the NED reference frame, and expressed in the Body reference Frame;

- p, q, r are the components of the angular velocity **ω** with respect to the NED reference frame, and expressed in the Body reference frame;

- Φ, Θ, Ψ are the Euler angles which define the vehicle altitude with respect to the NED reference frame;

- F_X, F_Y, F_Z are the components in Body reference frame of the resultant force applied on the vehicle;

- M_X, M_Y, M_Z are the components in Body reference frame of the resultant moment applied on the vehicle.

The equations or motion in body axes are [B16], [B44], [B45], [B46], [B47]:

Eq. 46 $\quad \dot{u} = \dfrac{F_X}{m} - qw + rv$

Eq. 47 $\quad \dot{v} = \dfrac{F_Y}{m} - ru + pw$

Eq. 48 $\quad \dot{w} = \dfrac{F_Z}{m} - pv + qu$

Eq. 49 $\quad \dot{p}I_X - \dot{q}I_{XY} - \dot{r}I_{XZ} = M_X + qr(I_Y - I_Z) + (q^2 - r^2)I_{YZ} + pqI_{XZ} - rpI_{XY}$

Eq. 50 $\quad -\dot{p}I_{XY} + \dot{q}I_Y - \dot{r}I_{YZ} = M_Y + rp(I_Z - I_X) + (r^2 - p^2)I_{XZ} + qrI_{XY} - pqI_{YZ}$

Eq. 51 $\quad -\dot{p}I_{XZ} - \dot{q}I_{YZ} + \dot{r}I_Z = M_Z + pq(I_X - I_Y) + (p^2 - q^2)I_{XY} + rpI_{YZ} - qrI_{XZ}$

The external forces and moments are modelled as follows [AR15]

Eq. 52 $\quad F_X = \bar{q}S C_X - mg\sin\Theta$

Eq. 53 $\quad F_Y = \bar{q}S C_Y + mg\sin\Phi\cos\Theta$

Eq. 54 $\quad F_Z = \bar{q}S C_Z + mg\cos\Phi\cos\Theta$

Eq. 55 $\quad M_X = \bar{q}Sb C_l$

Eq. 56 $\quad M_Y = \bar{q}Sc C_m$

Eq. 57 $\quad M_Z = \bar{q}Sb C_n$

where *S*, *c* and *b* are the reference aerodynamic area, longitudinal length and lateral length, respectively; *g* is the gravitational acceleration and $\bar{q}$ is the dynamic pressure; (C_X, C_Y, C_Z) and (C_l, C_m, C_n) are the dimensionless aerodynamic force and moment coefficients, respectively, expressed in body axes.

Eq. 46 to Eq. 51 represent the explicit formulation of Eq. 4. Concerning Eq. 52 to Eq. 57, some considerations are worthy to note:

- The thrust force is not explicitly mentioned, because in the case of re-entry vehicle, the vehicle is not propelled.

- The absence of an engine or other rotating mass allows neglecting the gyroscopic moments.

- The aerodynamic coefficients are expressed in body axes, whereas the aerodynamic model usually provides them in wind axes. The reference system transformation can be performed by using the rotation matrix defined by Eq. 132 in Appendix A.

- The aerodynamic coefficients are computed by means of the aerodynamic model, which should be identified from flight data. The structure of this model is described in details in the next section.

Eq. 46 - Eq. 51 are coupled to the following kinematic relations, which allows computing the vehicle position (*x*, *y*, *z*) and attitude with respect to the NED reference frame

$$\text{Eq. 58} \quad \dot{\Phi} = p + q \tan\Theta \sin\Phi + r \tan\Theta \cos\Phi$$

$$\text{Eq. 59} \quad \dot{\Theta} = q \cos\Phi - r \sin\Phi$$

$$\text{Eq. 60} \quad \dot{\Psi} = r \sec\Theta \cos\Phi + q \sec\Theta \sin\Phi$$

$$\text{Eq. 61} \quad \dot{x} = u \cos\Psi \cos\Theta + v(\cos\Psi \sin\Theta \sin\Phi - \sin\Psi \cos\Phi) + w(\cos\Psi \sin\Theta \cos\Phi + \sin\Psi \sin\Phi)$$

$$\text{Eq. 62} \quad \dot{y} = u \sin\Psi \cos\Theta + v(\sin\Psi \sin\Theta \sin\Phi + \cos\Psi \cos\Phi) + w(\sin\Psi \sin\Theta \cos\Phi - \cos\Psi \sin\Phi)$$

$$\text{Eq. 63} \quad \dot{z} = -u \sin\Theta + v \cos\Psi \cos\Theta \sin\Phi + w \cos\Theta \cos\Phi$$

Finally, the flight mechanics model is completed by some static relations introduced to compute relevant air data which are needed to evaluate the aerodynamic coefficient along the trajectory

$$\text{Eq. 64} \quad \mathbf{V_{TAS}} = \mathbf{V} - \mathbf{V_{wind}}$$

$$\text{Eq. 65} \quad \overline{q} = \frac{1}{2} V_{TAS}^2 \frac{P_S}{287.05 \cdot T_S}$$

$$\text{Eq. 66} \quad \alpha = \tan^{-1}\left(\frac{w - w_{wind}}{u - u_{wind}}\right)$$

$$\text{Eq. 67} \quad \beta = \sin^{-1}\left(\frac{v - v_{wind}}{\sqrt{(u - u_{wind})^2 + (v - v_{wind})^2 + (w - w_{wind})^2}}\right)$$

$$\text{Eq. 68} \quad M = \frac{V_{TAS}}{20.0468\sqrt{T_s}}$$

where M is the Mach number, T_s and P_s are the static temperature and pressure, respectively, $\mathbf{V_{TAS}}$ and $\mathbf{V_{wind}} \equiv (u_{wind}, v_{wind}, w_{wind})$ are true air speed and wind speed.

5.1.2 Aerodynamic Model

The expression of the aerodynamic coefficients present in Eq. 52 to Eq. 57 should be defined before performing parameters estimation.

Structured models, where the aerodynamic coefficients are expressed using polynomial functions of Mach number, aerodynamic angles and control surfaces deflection, are usually proposed in the literature for the purpose of re-entry vehicle system identification [B48], [B49]. In some cases, this polynomial functions are used to correct tabular aerodynamic database computed through CFD analysis or wind tunnel tests, by means of flight data analysis [B1]. These corrections can be incremental deltas on aerodynamic derivatives already included into the database [B17] or new additive terms, which make the aerodynamic coefficients dependent from new variables or combination of variables [B50]. Statistical methods are applied to identify which are the relevant terms to be included in the model [B49], [B51]. Since these models are not based upon first

principles, they cannot, in general, be applied outside of the region of the flight envelope where flight trials are undertaken.

A different approach is based on the definition of a structure of the aerodynamic model based on physical principles. In this case several challenging problems have to be faced [AR1]. The first of them arises from the variations of the flow structure about the vehicle, which depends on the current vehicle state variables and on some of their time derivatives. The simultaneous effect of all these quantities produces a pressure distribution on the aircraft surface, which depends on such variables in a complex fashion [B52]. Because of this complexity, the determination of reasonable expressions of the aerodynamic coefficients, in terms of the state variables, can be very difficult. Although the aerodynamic performances of several lifting vehicles, such as HL-10, HL-20, X-33, and X-38, have only recently been analysed [B53], [B54], the methodologies for calculating the aerodynamic characteristics of lifting bodies in subsonic, transonic, and supersonic regimes do not provide the same level of accuracy that is obtained for the classical wing-body configurations. This is apparent, in particular, for what concerns the variations of the lateral and directional coefficients with respect to aerodynamic angles and Mach number [B55]. In fact, the simultaneous effects of lateral flow, body angular rates, and fluid compressibility can determine complex situations, where these coefficients exhibit nontrivial, non-monotonic variations. The second problem is of a mathematical nature and regards the use of a tabular aerodynamic coefficiis database. If the aerodynamic coefficients are known for assigned values of the state variables, the accuracy of the coefficient values out of the data points (calculated through an interpolation procedure) depends on the adopted interpolation method and on the number of independent variables. Because these coefficients depend on quite a large number of state variables, the interpolation provides in general poor accuracy [B56], especially for the transonic variations of the lateral and directional coefficients at null sideslip angle, roll and yaw rates. Last, but not least, the aerodynamic controls, which influence the aerodynamic coefficients in conjunction with all the variables, determine a further difficulty for the determination of the aerodynamic coefficients of a lifting body.

The model used in the present work provides a continuous and regular analytical representation of dimensionless aerodynamic force and moment coefficients acting on the vehicle in the three regimes of subsonic, transonic and supersonic flow. The detailed definition of this model, firstly proposed by de Divitiis, is reported in [AR14]. It is based on the Kirchoff theorem, which in

origin was formulated for incompressible streams and is based on the linear property of the continuity equation. This theorem states that, for an incompressible flow, the local fluid velocity around an obstacle is a linear function of the characteristic velocities of the problem. To study the vehicle aerodynamics in the compressible regimes, the Kirchoff theorem is properly extended to the compressible streams, taking into account that the local velocity depends on the fluid compressibility through the von Kármán equation. The model allows expressing each aerodynamic coefficient as nonlinear function of Mach number, aerodynamic angles, control effectors deflections, angular rates, and a set of constant aerodynamic parameters. The nonlinear behaviour stems from the effect of Mach number in the transonic regime and from the aerodynamic characteristics of the examined vehicle, which is characterised by low aspect ratio lifting-body configuration.

Each aerodynamic coefficient is expressed as summation of the clean configuration contribution and the effects of the controls. The unsteady effects are assumed negligible. The expressions for clean configuration aerodynamic force coefficients in wind axes and moment coefficients in the body frame are [AR1]

Eq. 69
$$C_{clean}^D = \left(F_{uu}^D \cos^2 \alpha + F_{uw}^D \cos \alpha \sin \alpha + F_{ww}^D \sin^2 \alpha\right)\cos^2 \beta + F_{vv}^D \sin^2 \beta + \\ + \left(G_{uq}^D \cos \alpha \cos \beta + G_{wq}^D \sin \alpha \cos \beta\right)\widehat{q} + \left(G_{vr}^D \widehat{r} + G_{vp}^D \widehat{p}\right)\sin \beta$$

Eq. 70
$$C_{clean}^Y = \left(F_{uv}^Y \cos \alpha + F_{vw}^Y \sin \alpha\right)\sin \beta \cos \beta + \\ + \left(G_{up}^Y \widehat{p} + G_{ur}^Y \widehat{r}\right)\cos \alpha \cos \beta + G_{vq}^Y \widehat{r} \sin \beta \widehat{q} + \left(G_{wp}^Y \widehat{p} + G_{wr}^Y \widehat{r}\right)\sin \alpha \cos \beta$$

Eq. 71
$$C_{clean}^L = \left(F_{uu}^L \cos^2 \alpha + F_{uw}^L \cos \alpha \sin \alpha + F_{ww}^L \sin^2 \alpha\right)\cos^2 \beta + F_{vv}^L \sin^2 \beta + \\ + \left(G_{uq}^L \cos \alpha \cos \beta + G_{wq}^L \sin \alpha \cos \beta\right)\widehat{q} + \left(G_{vr}^L \widehat{r} + G_{vp}^L \widehat{p}\right)\sin \beta$$

Eq. 72
$$C_{clean}^l = \left(F_{uv}^l \cos \alpha + F_{vw}^l \sin \alpha\right)\sin \beta \cos \beta + \\ + \left(G_{vp}^l \widehat{p} + G_{vr}^l \widehat{r}\right)\cos \alpha \cos \beta + G_{vq}^l \sin \beta \widehat{q} + \left(G_{wp}^l \widehat{p} + G_{wr}^l \widehat{r}\right)\sin \alpha \cos \beta$$

Eq. 73
$$C_{clean}^m = \left(F_{uu}^m \cos^2 \alpha + F_{uw}^m \cos \alpha \sin \alpha + F_{ww}^m \sin^2 \alpha\right)\cos^2 \beta + F_{vv}^m \sin^2 \beta + \\ + \left(G_{uq}^m \cos \alpha \cos \beta + G_{wq}^m \sin \alpha \cos \beta\right)\widehat{q} + \left(G_{vr}^m \widehat{r} + G_{vp}^m \widehat{p}\right)\sin \beta$$

Eq. 74
$$C_{clean}^n = \left(F_{uv}^n \cos \alpha + F_{vw}^n \sin \alpha\right)\sin \beta \cos \beta + \\ + \left(G_{vp}^n \widehat{p} + G_{vr}^n \widehat{r}\right)\cos \alpha \cos \beta + G_{vq}^n \sin \beta \widehat{q} + \left(G_{wp}^n \widehat{p} + G_{wr}^n \widehat{r}\right)\sin \alpha \cos \beta$$

where $\widehat{\boldsymbol{\omega}} \equiv (\hat{p}, \hat{q}, \hat{r}) = \boldsymbol{\omega}\, c/V$ is the dimensionless angular velocity. It is worthy to note that since the examined vehicle is symmetric with respect to the longitudinal plane, each longitudinal aerodynamic coefficient is an even function of β, whereas the lateral-directional coefficients are odd functions of β. F_{hk}^{i} and G_{hk}^{i} are called static and rotational characteristic functions, respectively. They are the second-order derivatives of the generic aerodynamic coefficient and depend on free stream Mach number (M_∞) as follows

$$\text{Eq. 75} \quad F(M_\infty) = \vartheta_{sub} H_{sub} \frac{\sqrt{k_1 + k_2}\left(1 + k_3 M_\infty^2 + k_4 M_\infty^3\right)}{\sqrt{k_2 + k_1 \left|1 - M_\infty^{k_5}\right|^2}} + \vartheta_{sup} H_{sup} \frac{1 + k_6 M_\infty^{k_7}}{1 + k_8 M_\infty^{k_9}}$$

where the indexes *i*, *h* and *k* have been omitted, and the same structure holds for G_{hk}^{i}, too. $\vartheta_{sub}, \vartheta_{sup}, k_1, ..., k_9$ are aerodynamic constant parameters. H_{sub} and H_{sup} are two sigmoidal functions of free stream Mach number

$$\text{Eq. 76} \quad H_{sub}(M_\infty) = \frac{\tanh 50(1 - M_\infty) + 1}{2}$$

$$\text{Eq. 77} \quad H_{sup}(M_\infty) = \frac{\tanh 50(M_\infty - 1) + 1}{2}$$

Eq. 75 incorporates two addends: the first one gives the variation of the aerodynamic coefficients in the subsonic regime, whereas the second one describes the supersonic region. Indeed, H_{sub} is 1 if $M_\infty \leq 0.95$ and 0 if $M_\infty \geq 1.05$, whereas H_{sup} is 0 if $M_\infty \leq 0.95$ and 1 if $M_\infty \geq 1.05$. In transonic regime both the sigmoidal functions assume values between 0 and 1 and the combination of the subsonic and the supersonic contributions provides the aerodynamic coefficients in the transonic regime.

The examined re-entry vehicle has two sets of aerodynamic effectors: the elevons, that provide both pitch control when deflected symmetrically (δ_e) and roll control when deflected asymmetrically (δ_a), and the rudders, that deflect only symmetrically (δ_r) to allow yaw control. The rotation of the aerodynamic control surfaces modifies the vehicle geometry, which in turn determines a variation of the aerodynamic force and moment coefficients. The coefficients variations are [AR14]

Eq. 78 $\quad \Delta C_i^e (M_\infty, \alpha, \delta_e) = F_{e1}^i (M_\infty) \delta_e + F_{e2}^i (M_\infty) \delta_e \alpha + F_{e3}^i (M_\infty) \delta_e^n$

Eq. 79 $\quad \Delta C_j^a (M_\infty, \alpha, \delta_a) = F_{a1}^j (M_\infty) \delta_a + F_{a2}^j (M_\infty) \delta_a \alpha + F_{a3}^j (M_\infty) \delta_a^2$

Eq. 80 $\quad \Delta C_j^r (M_\infty, \alpha, \delta_r) = F_{r1}^j (M_\infty) \delta_r + F_{r2}^j (M_\infty) \delta_r \alpha + F_{r3}^j (M_\infty) \delta_r^2$

where $i = D, L, m,$ and $j = Y, l, n$. Indeed, the effects of the elevator on the lateral aerodynamic coefficients, which can occur for $\beta \neq 0$, are not taken into account in the present analysis. Similarly, the effects of the ailerons and of the rudders on the longitudinal aerodynamic coefficients are considered negligible. In the above equations, the first and the second terms on the right hand sides represent, respectively, the linear effect of the control and the combined effect of control and angle of attack, whereas the third addend is the nonlinear term. In Eq. 78 the exponent n varies, depending on the coefficient: it is assumed equal to 2 for C_D, whereas it values 3 for C_L and C_m. The functions $F_{e1}^i (M_\infty)$, $F_{e2}^i (M_\infty)$, $F_{e3}^i (M_\infty)$, $F_{a1}^j (M_\infty)$, $F_{a2}^j (M_\infty)$, $F_{a3}^j (M_\infty)$, $F_{r1}^j (M_\infty)$, $F_{r2}^j (M_\infty)$, $F_{r3}^j (M_\infty)$ are called elevator, ailerons and rudder characteristic functions. Their analytical structure is assumed to be described by equation Eq. 75.

In conclusion the following relations hold for the aerodynamic longitudinal coefficients C_i, $i = \{D, L, m\}$

Eq. 81
$$C_i = \left(F_1^i \cos^2 \alpha + F_2^i \cos \alpha \sin \alpha + F_3^i \sin^2 \alpha \right) \cos^2 \beta + F_4^i \sin^2 \beta +$$
$$+ \left(F_5^i \cos \alpha \cos \beta + F_6^i \sin \alpha \cos \beta \right) \widehat{q} + \left(F_7^i \widehat{r} + F_8^i \widehat{p} \right) \sin \beta + F_9^i \delta_e + F_{10}^i \delta_e \alpha + F_{11}^i \delta_e^n$$

and for the lateral aerodynamic coefficients C_i, $i = \{Y, l, n\}$

Eq. 82
$$C_i = \left(F_1^i \cos \alpha + F_2^i \sin \alpha \right) \sin \beta \cos \beta + \left(F_3^i \widehat{p} + F_4^i \widehat{r} \right) \cdot \cos \alpha \cos \beta + F_5^i \sin \beta \widehat{q} +$$
$$+ \left(F_6^i \widehat{p} + F_7^i \widehat{r} \right) \cdot \sin \alpha \cos \beta + F_{12}^i \delta_a + F_{13}^i \delta_a \alpha + F_{14}^i \delta_a^3 + F_{15}^i \delta_r + F_{16}^i \delta_r \alpha + F_{17}^i \delta_r^3$$

Each addendum in these equations contains a function of M_∞ expressed through Eq. 75, which also depends on a vector of free model parameters

Eq. 83 $\quad \boldsymbol{\theta}_\mathbf{i}^i = \left[\vartheta_{sub}, \vartheta_{sup}, k_1, ..., k_9 \right]$

and

Eq. 84 $\boldsymbol{\theta}^i = \left[\boldsymbol{\theta}^i_1, ..., \boldsymbol{\theta}^i_{Q(C_i)}\right]$

with $l = \left[1, ..., Q(C_i)\right]$, being $Q(C_i)$ the total number of addends for the coefficient C_i ($i = D, Y, L, l, m, n$).

Eq. 81 and Eq. 82 represent the explicit form of Eq. 8 and the unknown parameters vector $\boldsymbol{\Theta}_{\mathbf{P2}}$ to be estimated from flight data is a subset of $\boldsymbol{\Theta} = \left(\boldsymbol{\theta}^D, \boldsymbol{\theta}^Y, \boldsymbol{\theta}^L, \boldsymbol{\theta}^l, \boldsymbol{\theta}^m, \boldsymbol{\theta}^n\right)$. The subset is determined on the basis of an identifiability analysis.

All the parameters of the aerodynamic model are firstly determined before flight, fitting a pre-flight tabular aerodynamic database (ADB), built upon wind-tunnel test data and computational fluid dynamics analysis [B57]. This ADB covers a wide envelope of flight conditions and provides aerodynamic coefficients in tabular form. Uncertainty of predictions was also estimated, taking into consideration random experimental errors (repeatability), systematic experimental errors (known and not removable errors) and CFD errors (effect of computational grid, convergence, level of turbulence modelling, boundary conditions, etc.).

The pre-flight estimation is carried out through a least square (LS) method, which for each aerodynamic coefficient, is applied to the following optimisation problem:

Eq. 85 $\min\limits_{\vartheta_i} J_i = \min\limits_{\vartheta_i} \sum\limits_{i=1}^{M_p} \left[\left(C_k^i\right)_{ADB} - C_k^i\right]^2, \qquad i = D, Y, L, l, m, n$

where C_{ik} and $(C_{ik})_{ADB}$ are the aerodynamic coefficients calculated in M_p points of the flight envelope, with the proposed model and the pre-flight aerodynamic database, respectively. J_i is the goal function, defined for each aerodynamic coefficient, for which the arguments are the free parameters $\boldsymbol{\theta}^i$ given by Eq. 84. To take into account the combined effects of all the vehicle state variables and those of the controls, the coefficients C_{ik} and $(C_{ik})_{ADB}$ are calculated in a wide range of variation of these variables.

In the following of the thesis, the model obtained through pre-flight estimation is called pre-flight analytical aerodynamic model

5.2 Identification Strategy and Techniques

A two-step estimation strategy [AR9], [B58] is applied to solve the re-entry vehicle model identification problem, as illustrated in Figure 5.1 [AR1].
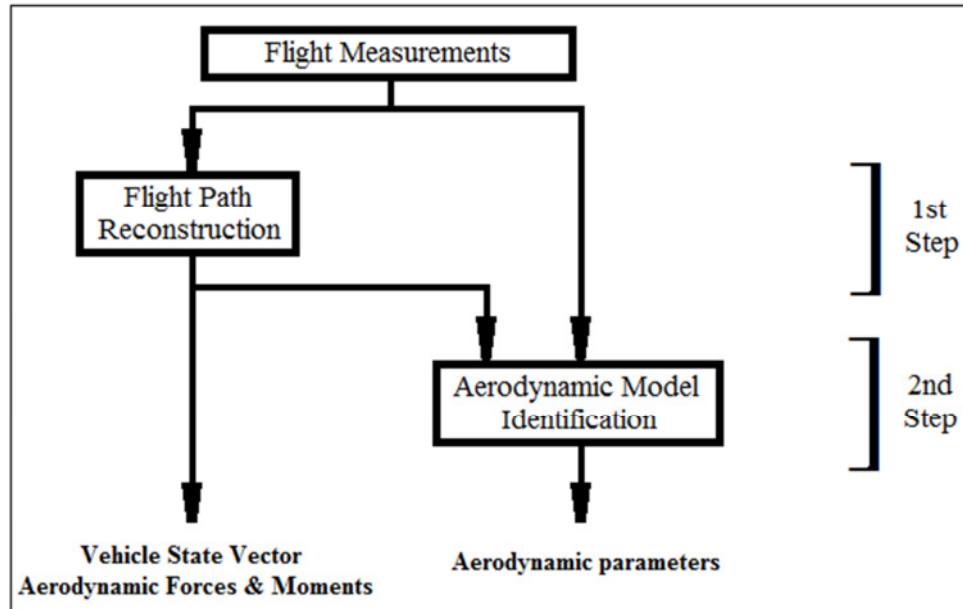
Figure 5.1 - Identification strategy

The first step is formulated as a nonlinear filtering problem and provides the estimation of vehicle state vector, aerodynamic coefficients and some atmospheric properties (such as local wind experienced during the mission). The nonlinearity stems from the vehicle nonlinear equations of motion. It is worthy to remark that in this step the time histories of global aerodynamic coefficients along the flight trajectory are only estimated and not the aerodynamic model. These time histories have a twofold role, being necessary both as input for the second identification step and for the validation of the available pre-flight aerodynamic database.

The second step receives in input the vehicle filtered state vector, the aerodynamic coefficients and related uncertainties calculated in the previous step, and delivers an estimation for the subset of the identifiable parameters of the aerodynamic model, that is selected using a sensitivity analysis. When the estimation is carried out, the uncertainties on vehicle state and aerodynamic coefficients computed in the first estimation step are treated as measurement noise and they are rigorously propagated through the second step. In this way, the identification process provides the nominal value and the related estimation uncertainty of the aerodynamic parameters, and

guarantees an accurate and reliable characterisation of the identified aerodynamic model, by using all the available pre-flight information and in-flight gathered data.

Before starting the first identification step, a compatibility check is performed using kinematic relations [B1], in order to check the flight measurements consistency and the correctness of the measurement errors characterisation. To this end, Eq. 46 to Eq. 48 are recast in the form:

Eq. 86 $\qquad \dot{u} = a_X - qw + rv$

Eq. 87 $\qquad \dot{v} = a_Y - ru + pw$

Eq. 88 $\qquad \dot{w} = a_Z - pv + qu$

where a_x, a_y, a_z are the CoM acceleration components in body axes. Next, time integration of Eq. 86 to Eq. 88 and Eq. 58 to Eq. 60 is carried out. The flight measurements of acceleration and angular rate components are provided in input to the integration, together with the starting values of velocity and Euler angles. In output the integrator delivers the time histories of velocity and Euler angles, which are compared to their flight measurements. Each flight measurement is characterised by an uncertainty, defined by the technical specification of the sensors. If the difference between integration output and related flight measurement is lower than the measurement uncertainty along the considered flight segment and for all the considered variables, then the measurements set is considered consistent and it can be used for system identification, according to the identification step described in details in the following sub-sections.

5.2.1 First Identification Step

First identification step is solved using the Unscented Kalman Filter according to the hypotheses and implementation described in section 4.2.1.

The prediction phase of the estimation requires the definition of the filter dynamic model, whose state vector should include all the unknowns to be estimated. This model is stochastic and should be suitably characterised through the definition of some properties, such as model order, correlation time, process and measurements noises variance, that could affect the filter convergence. Most of them are specified in a rigorous way, as shown in this section. The

remaining parameters are considered as free variables for the filter design, and they are tuned when the identification procedure is preliminarily carried out on simulated data. The adopted filter's model is sketched in Figure 5.2.
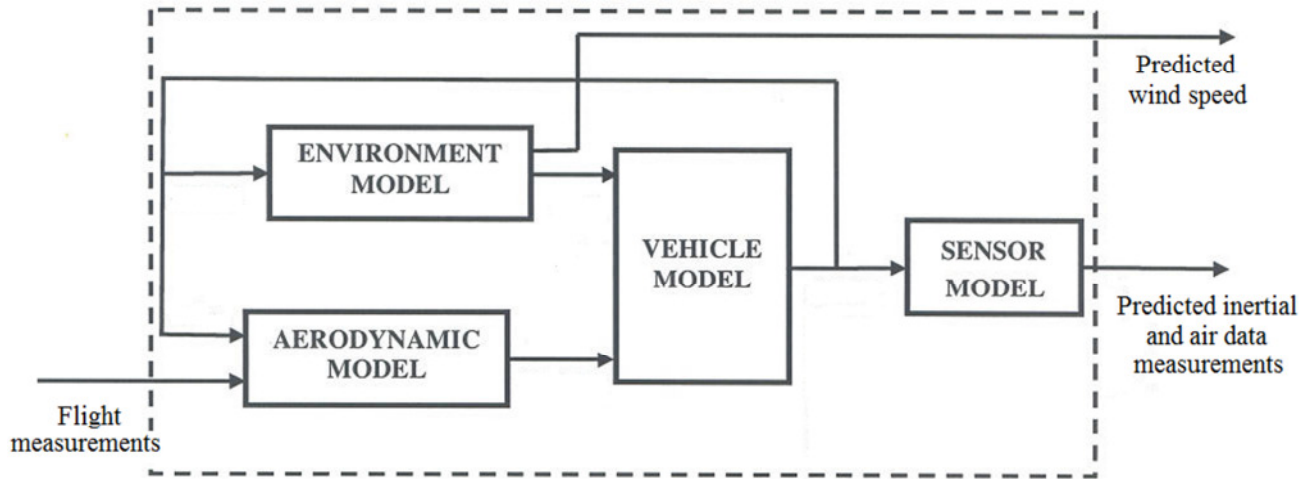
Figure 5.2 – Filter's model

The model is composed of four main blocks: Vehicle model, Environment model, Aerodynamic model, Sensor model.

The Vehicle model is based on the classical 6 DoF rigid body nonlinear equations of motion (Eq. 46 to Eq. 51), therefore its state vector is composed of CoM position and velocity components, attitude angles, and angular rates. The model is characterised by an additive process noise, whose variance is a free design parameter of the filter. However its value is set very low, due to high confidence in the vehicle model.

The Aerodynamic model provides force ($\mathbf{C_F}$) and moment ($\mathbf{C_M}$) coefficients in body axes. They are transformed in dimensional force and moment and sent in input to the vehicle equations of motion. More in detail, the aerodynamic coefficients are computed as summation of baseline deterministic components ($\mathbf{C}_{\textbf{F-}BAS}$, $\mathbf{C}_{\textbf{M-}BAS}$) and corrections ($\Delta\mathbf{C}_F, \Delta\mathbf{C}_M$) resulting from stochastic processes [AR1], [AR9], [AR16]:

Eq. 89 $\qquad \mathbf{C_F} = \mathbf{C}_{\textbf{F}-BAS} + \Delta\mathbf{C}_F$

Eq. 90 $\qquad \mathbf{C_M} = \mathbf{C}_{\textbf{M}-BAS} + \Delta\mathbf{C_M}$

The former are evaluated from the in-flight measurements of load factors **n**, angular rates **ω**, and dynamic pressure $\bar{q}$, namely

Eq. 91 $\mathbf{C}_{\mathbf{F}-BAS} = -\dfrac{\left(m \cdot \mathbf{n}|\mathbf{g}|\right)}{\bar{q}S}$

Eq. 92 $\mathbf{C}_{\mathbf{M}-BAS} = \dfrac{\mathbf{I}\dot{\boldsymbol{\omega}} + \boldsymbol{\omega} \times \mathbf{I}\boldsymbol{\omega}}{\bar{q}SL}$

where $\dot{\boldsymbol{\omega}}$ is obtained by numerical differentiation of **ω** and *L* represents the aerodynamic reference length, which coincides with *c* for the pitching moment coefficient and with *b* for the lateral-directional moment coefficients.

The corrections to the baseline aerodynamic coefficients are the unknowns to be estimated by the filter, therefore they are included into the filter state vector and their dynamics are modelled through Gauss-Markov (GM) stochastic processes. GM models are introduced [AR1], [AR9], because they fit a large number of physical processes with reasonable accuracy and simple mathematical description [B59]. The model's order and parameters could be evaluated for each unknown variable by analysing the autocorrelation function of a realization of the variable along the mission trajectory [B60]. This analysis is performed in simulation before flight, taking advantage of the a priori information provided by the available pre-flight aerodynamic database. For the re-entry mission identification problem, as many as 2,000 Monte Carlo simulations were carried out considering uncertainties on aerodynamics, inertia, vehicle initial state, sensors and actuators characteristics, and environmental disturbances. For each simulation, the aerodynamic corrections are evaluated as differences between true aerodynamics (known in simulation) and baseline aerodynamic terms, provided by Eq. 91 and Eq. 92, and the related autocorrelation functions are computed. Finally, for each aerodynamic coefficient a mean normalized autocorrelation function is evaluated.

Figure 5.3 shows the normalized mean autocorrelation for lateral force correction, the other force corrections have similar behaviour. This autocorrelation is typical of first-order GM process, therefore first order GM model is selected for the correction to force coefficients. They are modelled through the following equation [B60]

Eq. 93 $\Delta \dot{\mathbf{C}}_F = -\dfrac{1}{\tau} \Delta \mathbf{C}_F + \mathbf{w}_F$

where τ is the correlation time, computed as 1/3 of the time delay where the normalized autocorrelation function has a value of 0.05 [B59]. $\mathbf{w}_F$ is the process noise, with standard deviation $\boldsymbol{\sigma}_{WF}$. The ith component of $\boldsymbol{\sigma}_{WF}$, denoted with σ_{WFi}, is computed as [B59]

Eq. 94 $\sigma^2_{WFi} = 2\sigma^2_{Fi-MC} \big/ \tau_i$

where σ_{Fi-MC} is the standard deviation of the simulated trajectories of the correction to the ith aerodynamic force coefficient, computed in the aforementioned Monte Carlo analysis, and τ_i is the related correlation time.
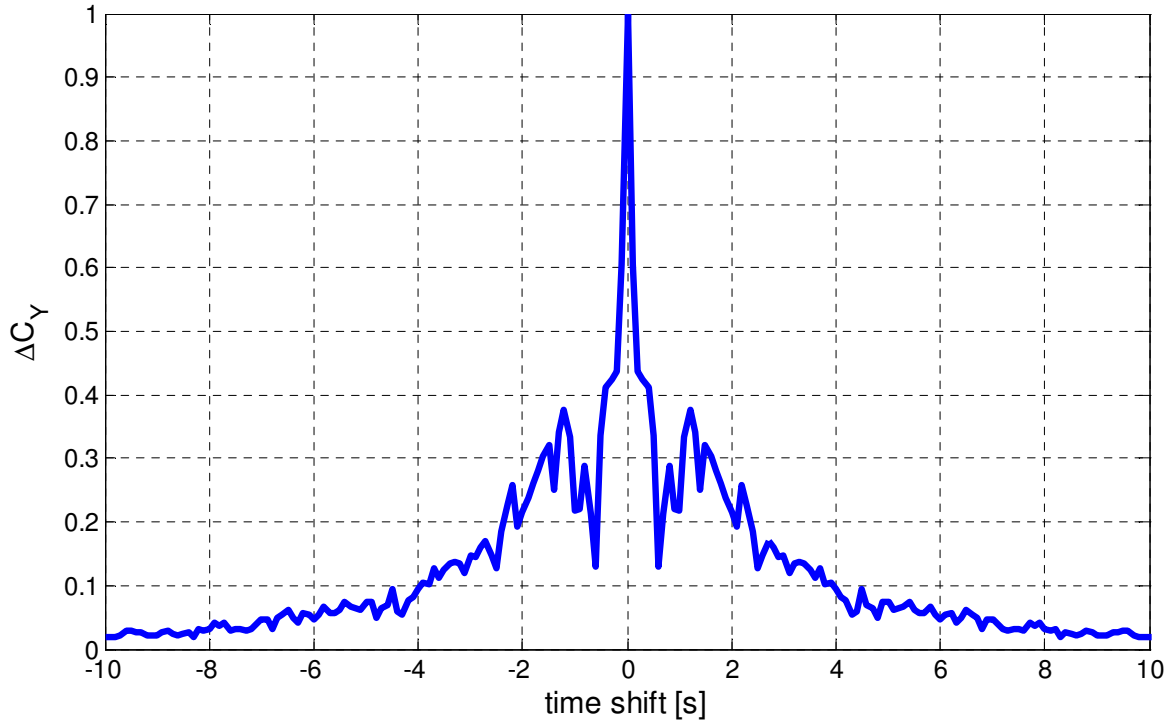
Figure 5.3 – Mean normalized autocorrelation for the correction to the baseline lateral force aerodynamic coefficient

The autocorrelation functions of the pitching moment correction is presented in Figure 5.4. It has an impulsive shape, typical of a zero-order GM processes. Similar results hold for the other moment coefficients. Accordingly, we get [B60]

Eq. 95 $\Delta \dot{\mathbf{C}}_M = \mathbf{w}_M$

where $\mathbf{w}_M$ is the process noise, whose standard deviation coincides with the standard deviation of the simulated trajectories of the corrections to the aerodynamic moment coefficients computed in the aforementioned Monte Carlo analysis [B59], namely

Eq. 96 $\qquad \boldsymbol{\sigma}_{WM} = \boldsymbol{\sigma}_{M-MC}$
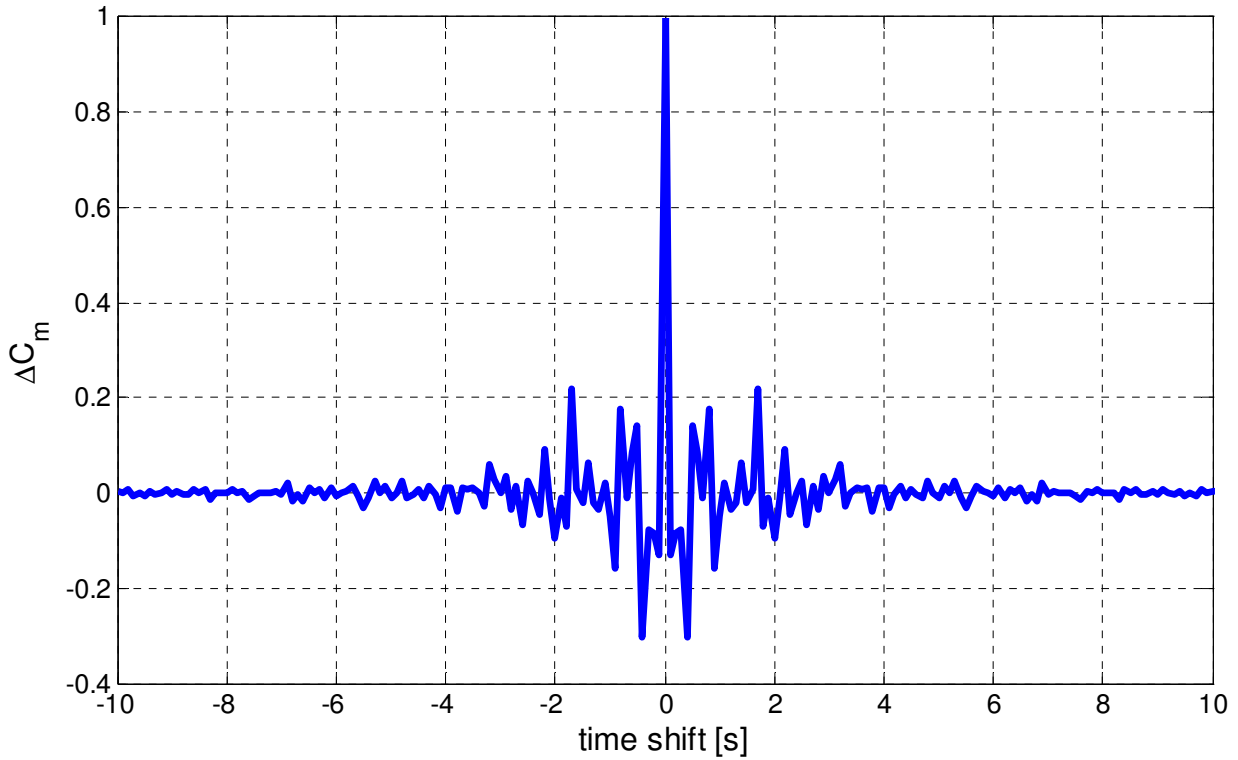
Figure 5.4 – Mean normalized autocorrelation for the correction to the baseline pitching moment aerodynamic coefficient

The Environment model is composed of the gravitational model and the atmospheric model. The first one is based on the WGS84 (World Geodetic System) [B61] and it is used to compute the gravitational acceleration as a function of vehicle position. The latter is based on the meteorological forecast data of the European Centre for Medium-Range Weather Forecasts (ECMWF) [B62], that provides, for a selected location and date, the baseline profiles for wind velocity, air temperature and pressure. High frequency corrections to these baseline trajectories are estimated by the filter and their dynamic behaviour is again modelled by means of Gauss-Markov models.

For the examined case study, which is described in details in sections 7.1 and 8, the order and statistical characterisation of the GM models adopted for the wind correction are assessed

through the analysis of flight data collected during the ascent phase of the experimental CIRA Dropped Transonic Flight Test missions, when the vehicle is carried by a balloon at the release altitude. We assume that, in the ascent phase, the horizontal components of wind velocity in the NED reference frame are almost coincident with the corresponding components of the CoM measured velocity (balloon transported by the wind) and that the wind does not change in the time frame between ascent and descent phases. Under these hypotheses, the high frequency correction versus altitude is determined (and stored in a lookup table) as the difference between the CoM velocity measured during the ascent phase and the wind speed given by the ECMWF. Then the table is queried with the altitude trajectory of the missions descent phase to get the correction time history during mission flight. The autocorrelation function of the correction is then evaluated. The normalized autocorrelation of the North component of wind correction for DTFT1 is shown in Figure 5.5 [AR12]; similar plot is obtained for the East component, too. The autocorrelation is typical of a first-order process, described by the model

$$\text{Eq. 97} \qquad \Delta\dot{V}_{wind\,i} = -\frac{1}{\tau_{wnd\,i}}\Delta V_{wnd\,i} + \eta_{wnd\,i} \;, \quad i = \{East, North\}$$

where τ_{wind} and η_{wind} are correlation time and process noise, respectively. The correlation time is equal to 1/3 of the time delay, where the normalized autocorrelation function has a value of 0.05. The process noise, characterised by its variance, is a free parameter for the UKF design. The obtained model has also been applied to the Down component of wind correction, where no information can be extracted from the ascent phase data. Since no a priori information was available on the high frequency corrections of static temperature (T_S) and pressure (P_S) with respect to ECMWF, we assume they can be described by a zero-order GM model

$$\text{Eq. 98} \qquad \Delta\dot{T}_S = \eta_{Ts}$$

$$\text{Eq. 99} \qquad \Delta\dot{P}_S = \eta_{Ps}$$

where the process noises η_{Ts} and η_{Ps} are again design parameter for the filter. The initial value of all the GM state is set to zero.

Concerning the wind velocity, the high frequency corrections are low pass filtered in order to compute their low frequency content. Since we assume that the low frequency content is

correctly provided by the ECMWF (that is, the low frequency component of wind velocity coincides with the baseline profile), the output of the low pass filter should be null, therefore it could be compared with a zero virtual measurement in the correction phase of the UKF. The variance of the process noise for the low pass filter model is set to very low value (with respect to the other process noises variance) due to the reliability of the model.
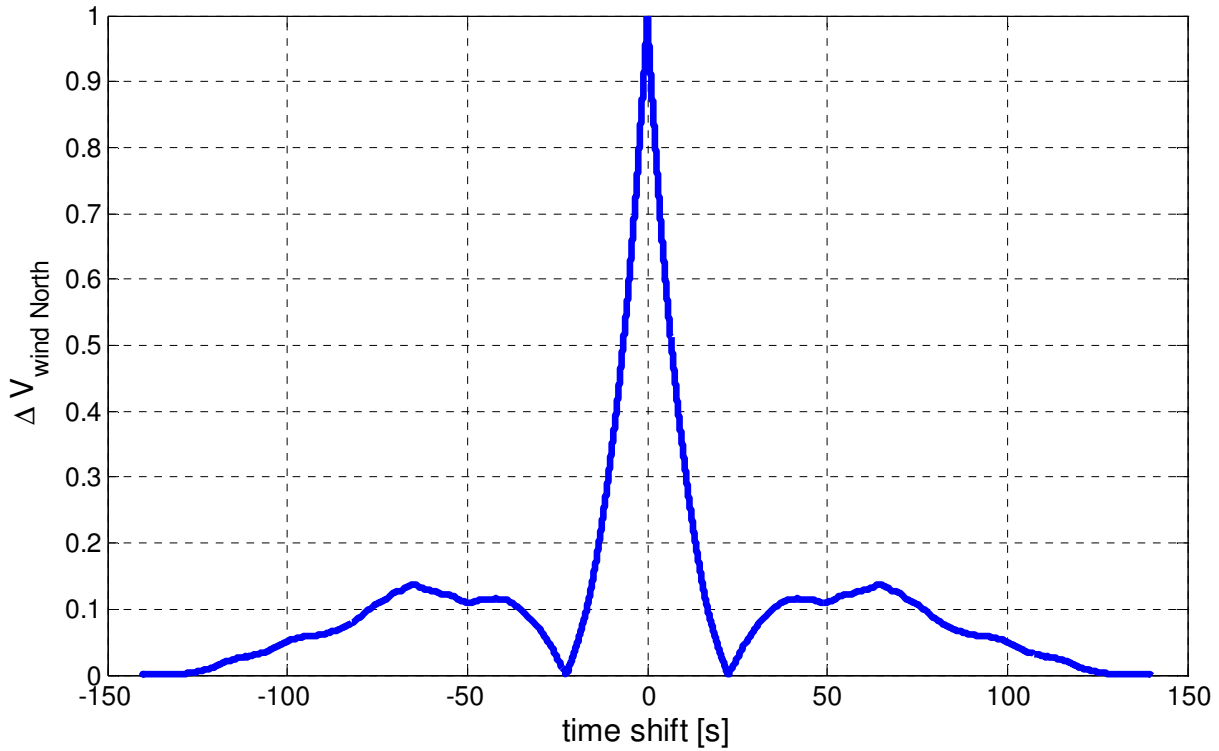
Figure 5.5 – Normalized autocorrelation function of correction on the North component of wind

Finally, the Sensor model is implemented to match the specifications of the actual on board sensors. It is composed of the measurements equations (Eq. 64 to Eq. 68) for the computation of aerodynamic angles, Mach number and dynamic pressure.

Globally the filter model has 25 states, that is, 12 states for the rigid vehicle, 6 from the aerodynamic coefficients (corrections to the six baseline trajectories) and 7 from the Environment model (corrections to the baseline trajectories of three wind components, atmospheric temperature and pressure, plus two states related to the low-pass filter).

Concerning the UKF correction phase, the predictions are updated using the flight measurements of CoM accelerations, angular rates, Euler angles, angles of attack and sideslip, Mach number.

Moreover, three null virtual measurements are considered. They are compared with the low pass filtered wind velocity corrections, as previously described. Flight measurements are defined by nominal values and uncertainty characterisations (measurement noise covariance matrix), which are provided by the sensors datasheet. The covariance matrix of the virtual null measurements coincides with the noise covariance matrix given by the ECMWF for the baseline low-frequency profiles of wind velocity.

It is worthy to note that the GM models, which describe the correction to the baseline aerodynamic coefficients trajectories, are only introduced to estimate the time histories of global aerodynamic coefficients along the mission trajectory. They do not represent the aerodynamic model to be identified, whose structure is instead defined in section 5.1.2.

In conclusion, the output of the first identification step is the estimation of the filter state vector time history and the related uncertainty characterisation, that is the nominal trajectories and uncertainty bounds of vehicle state, aerodynamic coefficients, and environment parameters (wind components, atmospheric temperature and pressure). All these estimation are provided in input to the second identification step.

5.2.2 Second Identification Step

The second identification step aims at identifying from flight data the aerodynamic model, whose structure is defined in section 5.1.2. This model includes many parameters and, taking into account the limited amount of available flight data, not all of them can be updated in post flight analysis. Therefore the attention is focused on a subset of those parameters, composed of all the gains ϑ_{sub} and ϑ_{sup} which are defined in Eq. 75. They appear in each addend on the right hand side of equations Eq. 81 and Eq. 82. Some of these gains, denoted as subset $\mathbf{\Theta_{P2}}$, is identifiable from the available flight measurements and then they are estimated. The other gains, as well as all the other parameters of the model, are kept equal to the pre-flight identified values.

The selection of the identifiable gains is performed considering the Cramer–Rao bounds (CRBs) [B1], [B31]. The CRB indicates the theoretically maximum accuracy of the estimate for an unknown parameter achievable from the analysis of flight data along an assigned trajectory. It can be considered as a measurement of the sensitivity of system outputs along a flight trajectory with respect to parameter variation. The CRBs can be used both for the optimisation of the

identification manoeuvres to be performed during flight test [B26], in order to increase the information content of the flight data, or for the selection of the identifiable parameters along a fixed trajectory [B31], [B63]. The last one is the application used in this thesis.

Let's denote with $\mathbf{\Theta}_G$ the set composed of all the of gains ϑ_{sub} and ϑ_{sup} included in the aerodynamic model. The CRB related to the generic gain $\vartheta_k \in \mathbf{\Theta}_G$, indicated with σ_{ϑ_k}, is computed through:

$$\text{Eq. 100} \qquad \mathbf{D}_M = \mathbf{F}_M^{-1} = \left[\sum_{i=1}^{N_T} \left[\left(\frac{\partial \mathbf{Y}(t_i)}{\partial \mathbf{\Theta}_G} \right)^T \mathbf{R}^{-1} \left(\frac{\partial \mathbf{Y}(t_i)}{\partial \mathbf{\Theta}_G} \right) \right] \right]^{-1}$$

$$\text{Eq. 101} \qquad \sigma_{\vartheta_k} = \sqrt{D_M(k,k)}$$

where $\mathbf{Y}$ is the output vector of the system to be identified, recorded in N_T time instants, denoted as t_i. $\mathbf{R}$ is the covariance matrix of measurement error on $\mathbf{Y}$. $\mathbf{F}_M$ represents the information matrix (also named Fisher matrix), $\mathbf{D}_M$ is the dispersion matrix and $D_M(k,k)$ is the kth element on the main diagonal of $\mathbf{D}_M$. Concerning the computation of the information matrix, in the examined case the output $\mathbf{Y}$ coincides with the vector composed by the aerodynamic coefficients. Since they are expressed by regular analytical functions, their derivatives with respect to each gain (that is, $\partial \mathbf{Y}(t_i)/\partial \mathbf{\Theta}_G$) can be analytically computed. These derivatives can be evaluated along the flight trajectories using the flight measurements of Mach number, aerodynamic angles, control effectors deflections and vehicle angular rate. The matrix $\mathbf{R}$ is composed of the aerodynamic coefficients variances, which are provided by the first estimation step. After the computation of $\mathbf{D}_M$, all the parameters which have σ_{ϑ_k} lower than a pre-fixed threshold are included in the identifiable subset, denoted as $\mathbf{\Theta}_{P2}$.

Once the set of identifiable unknown parameters has been selected, their values can be estimated.

Two different estimation methodologies can be applied in this identification step. Due to the structure of the aerodynamic model, in both cases parameters estimation is performed independently for each global aerodynamic coefficient and for subsonic and supersonic regime.

The first approach is based on the UKF [AR9]. It requires the definition of a model for the unknown parameters, to be used in the prediction phase of the filter. Let's denote with

- $\mathbf{\Theta}_{\mathbf{P2}}^{i}$ the vector of identifiable parameters related to the ith aerodynamic coefficient;

- $C_{i\text{-step1}}$ and P_{CiCi} the ith aerodynamic coefficient and the related variance estimated along the mission trajectory in the first identification step;

- **E** and $\mathbf{P}_{EE}$ the vector composed of estimation of aerodynamic angles, Mach number and angular velocity provided by the first identification step and the related covariance matrix;

- $\mathbf{\delta} = [\delta_e, \delta_a, \delta_r]$ and $\mathbf{P}_{\delta\delta}$ the vector of aerodynamic effector deflections, measured in flight, and the related covariance matrix.

The following filter model equations are used

Eq. 102 $\qquad \dot{\mathbf{\Theta}}_{\mathbf{P2}}^{i} = \mathbf{\eta}_{\Theta}^{i}$

Eq. 103 $\qquad res_i = C_{i-step1} - C_i(\mathbf{\Theta}_{\mathbf{P2}}, \mathbf{E}, \mathbf{\delta})$

Since the unknown parameters are constant, their dynamic equation (Eq. 102) is described by zero order GM process. The initial condition of this equation is the pre-flight value of the parameters. Covariance matrices of initial condition and process noise $\mathbf{\eta}_{\Theta}^{i}$ are design parameters to tune the filter.

Eq. 103 represents the filter output equation, which is based on the analytical aerodynamic model equations. In particular, C_i is computed through Eq. 81 and Eq. 82, and its difference with respect to first identification step of the coefficient along the trajectory is denoted as residual (res_i).

The UKF implementation presented in section 4.2.1 is adopted, with only one change: an augmented Unscented Transformation is applied only for the propagation of mean and covariance of the residual through the nonlinear output equation, that is step 5P of the prediction phase. In particular Eq. 11 is reformulated as follows

$$
\text{Eq. 104} \qquad
\boldsymbol{\chi}_i =
\begin{bmatrix}
\overline{\boldsymbol{\Theta}}_{P2}^{i}(t_{k-}) \\
C_{i-step1}(t_k) \\
\mathbf{E}(t_k) \\
\boldsymbol{\delta}(t_k)
\end{bmatrix}
+ \left(\sqrt{\lambda \mathbf{P}_k^{a-}} \right)_i ; \qquad i = 1..N_F
$$

$$
\boldsymbol{\chi}_0 =
\begin{bmatrix}
\overline{\boldsymbol{\Theta}}_{P2}^{i}(t_{k-}) \\
C_{i-step1}(t_k) \\
\mathbf{E}(t_k) \\
\boldsymbol{\delta}(t_k)
\end{bmatrix} ;
$$

$$
\boldsymbol{\chi}_{i+N_a} =
\begin{bmatrix}
\overline{\boldsymbol{\Theta}}_{P2}^{i}(t_{k-}) \\
C_{i-step1}(t_k) \\
\mathbf{E}(t_k) \\
\boldsymbol{\delta}(t_k)
\end{bmatrix}
- \left(\sqrt{\lambda \mathbf{P}_k^{a-}} \right)_i ; \qquad i = 1..N_F
$$

where $\overline{\boldsymbol{\Theta}}_{P2}^{i}(t_{k-})$ is the filter prediction of the unknown parameters at time t_k, and the other symbols represent the evaluation of the variables previously defined at time t_k. The prediction of the augmented covariance matrix is defined as

$$
\text{Eq. 105} \qquad
\mathbf{P}_k^{a-} =
\begin{pmatrix}
\mathbf{P}_k^{-} & 0 & 0 & 0 \\
0 & P_{CiCi} & 0 & 0 \\
0 & 0 & \mathbf{P}_{EE} & 0 \\
0 & 0 & 0 & \mathbf{P}_{\delta\delta}
\end{pmatrix}
$$

with $\mathbf{P}_k^{-}$ given by Eq. 15, in which $\mathbf{x}_k^{-} = \overline{\boldsymbol{\Theta}}_{P2}^{i}(t_{k-})$ and $\mathbf{Q}$ is the covariance matrix of dynamic equation process noise $\boldsymbol{\eta}_{\Theta}^{i}$.

The augmented formulation allows properly managing the stochastic characterisation of the estimation. Indeed the first identification step results are treated as input to the second step and the uncertainty on the first step estimation is taken into account as measurement noise.

Eq. 109 and Eq. 110 are used in the prediction phase of the filter, whereas in the correction phase a virtual null measurement of the residual (res_i) is used.

The virtual measurement should be stochastically characterised in terms of measurement noise covariance matrix $\mathbf{R}$. This matrix is evaluated before flight using the available information. To this end, a Monte Carlo analysis of the mission is carried out, and for each simulation the

residual is computed as difference between the tabular pre-flight ADB and the pre-flight analytical aerodynamic model, that is, the analytical model error. Next the statistics of the Monte Carlo analysis can be evaluated and the matrix **R** can be computed.

The second approach is based on the Least Square estimation methodology [AR17], described in section 4.2.2. In contrast to UKF, LS only requires measurements equations, that is the analytical model, and does not need any initial guess or dynamic model describing the dynamics of the unknowns, which could eventually influence the convergence of the estimations. Since the aerodynamic model is linear with respect to the selected identifiable unknown parameters, in order to perform the estimation, the expression of the ith aerodynamic coefficient (Eq. 81 for the force coefficients and Eq. 82 for the moment coefficients) is rearranged in the form of Eq. 23, which is reported here

$$\text{Eq. 106} \qquad \mathbf{z}_i = \mathbf{A}_i \cdot \mathbf{\Theta}^i_{P2}$$

where $\mathbf{z}_i$ is given by the difference, evaluated in N_T time instants, between the global aerodynamic coefficient $C_{i\text{-}step1}$ and the summation of all the additive terms on the right hand side of Eq. 81 or Eq. 82 (depending on the coefficient) that are related to non-identifiable gains. These additive terms are evaluated using Mach number, aerodynamic angles and angular rate estimated in the first step, and the flight measurements of aerodynamic effectors. The matrix of the regressors $\mathbf{A}_i$ is composed of the additive terms on the right hand side of Eq. 81 or Eq. 82 (depending on the coefficient) related to the identifiable gains divided by the gains themselves, which are included in $\mathbf{\Theta}^i_{P2}$.

Finally the uncertainties on the estimated parameters are evaluated through a Monte Carlo analysis. To this end, many estimations of the same unknown parameters are carried out by using in input flight measurements and global aerodynamic coefficients randomly selected in their range of uncertainty. The statistics of the estimated parameters are then evaluated and used to define the estimation uncertainty on each of the evaluated aerodynamic parameters.

In conclusion, when the second step identification is carried out, the uncertainties on the results of the first identification step are treated as measurement noise and they are rigorously propagated through the second step, whatever the applied estimation methodology is. Therefore, the identification process provides the nominal value and the related estimation uncertainty of

the aerodynamic parameters, and guarantees an accurate and reliable characterisation of the identified aerodynamic model, by using all the available pre-flight information and in-flight gathered data.

6 MODEL IDENTIFICATION OF A ROTORCRAFT VEHICLE

Rotorcraft system identification is a challenging task, mainly due to the complexity of the model used to describe the vehicle dynamics. In fact, rotorcraft aeromechanical analyses are usually based on highly nonlinear coupled multi-body models [B2], which include both slow flight mechanics scales and faster aero-elastic ones. Furthermore the rotorcraft models are typically unstable, at least in certain flight conditions [B15]. For those reasons, suitable identification techniques have to be developed to get high fidelity simulation models of rotorcraft dynamics.

The multi-step estimation approach, proposed in this thesis, allows exploiting the advantage of both time and frequency domains methods and, together with the selection of a suitable vehicle model structure, permits to obtain an identified model applicable in the whole frequency range of interest (from low to high frequencies). The model structure and the identification strategy and techniques are presented in the next sub-sections.

6.1 Flight Mechanics Model

A rotorcraft is generally modelled for simulation purposes as nonlinear multi-body dynamic system, characterised by strong coupling between the dynamics of rotor blades and air flow passing through the rotor (inflow) with those of the fuselage, control system and engine [B2]. The structure of this model is very complex and could include a huge number of uncertain parameters, which leads to identifiability issue: the model has too many parameters (over parameterisation) and then too many degrees of freedom with respect to the available flight measurements [B1]. Therefore simplified model structure should be introduced for identification purpose. A literature analysis has enhanced that several model structures are proposed to this aim.

The simplest model is based on the classical rigid body 6 DoF equation of motion [B64]. It can be used in the nonlinear form (incorporating nonlinear aerodynamics) or can be linearised with respect to a trim flight condition [B65], limiting its applicability to a small operative range. Such so called low frequency rigid body 6 DoF models are generally adequate for flying qualities investigations and less demanding control system design [B66].

In order to take into account unmodelled high frequency dynamics, the Quasi-Steady 6 DoF models are introduced, based on the assumptions that transient rotor dynamics are modelled as equivalent time delays on control inputs, and rotor steady state response is modelled as equivalent quasi-steady fuselage derivatives [B2]. The use of equivalent time delays stems from the observation that flight measurements show a delay between control inputs and rotational accelerations, caused by the dynamic characteristics of the main rotor, which are neglected in the rigid body 6 DoF models. However, it has been shown that in some cases Quasi-Steady models couldn't be able to match flight data on-axis responses at higher frequencies [B67]. In general Quasi-Steady models are appropriate for applications in the lower and mid frequency range [B68].

High bandwidth models require a more complex modelling approach, named hybrid modelling, based on the augmentation of the 6 DoF rigid body model with rotor degrees of freedom, in order to meet high bandwidth requirements and to capture the rotor dynamics and the rotor fuselage interactions [B66]. Several hybrid models are proposed in the rotorcraft identification literature, with different complexity depending on the considered rotor dynamics:

- 10th order model: longitudinal and lateral flapping dynamics are modelled through first order equations. The obtained system is able to capture the majority of the rotor dynamics and rotor fuselage interactions [AR11], [AR13], [B1], [B69], [B70].

- 11th order model: the above model is augmented with the main rotor RPM dynamic, described by a first order equation [AR8], [B69], [B70].

- 16th order model: longitudinal and lateral flapping, coning and lead-lag dynamics are modelled as second order systems. This model can provide a more detailed insight into the helicopter dynamics. However system identification needs complete measurements of blade motions (both flap and lag angles) [B1], [B68].

- Inflow dynamics: the above model is augmented with a parametric Pitt and Peter inflow model, to describe the inflow dynamics [B68], [B71]. The number of model parameters to be estimated increases significantly. In this case a classical system identification problem can occur: the estimation can provide parameter values that don't represent the phenomena of

interest, to which they are related, rather they can account for some other unmodelled effects [B1].

- Hybrid fully coupled model: 13 DoF model, with coupled fuselage-regressive flap dynamics (8 DoF), coupled coning-inflow dynamics (2 DoF), lead-lag dynamics (2 DoF) and Engine torque response (1 DoF) [B2].

Hybrid models are suitable for higher frequency applications, that are high fidelity simulation, high precision fly by wire control law design and flight comfort evaluation.

The selection of model structure is performed considering the desired frequency range of application of the identified model, the dynamics to be reproduced by the model and the available flight measurements. For example, rotor dynamic modes are often important; however, in practice, the complete rotor dynamics measurements are difficult to obtain and with the fuselage based measurements only, rotor modes are difficult to be identified.

The model adopted in this thesis belongs to the hybrid model class, and it is composed of classical nonlinear rigid body 6 degrees of freedom equations of motion, to describe fuselage dynamics; main rotor first order nonlinear differential model, to simulate rotor blades flap angle and shaft angular position; static nonlinear model to evaluate the global force and moment acting on the fuselage during flight. Figure 6.1 presents the functional blocks of the model to be identified, these blocks are described in the following subsections.
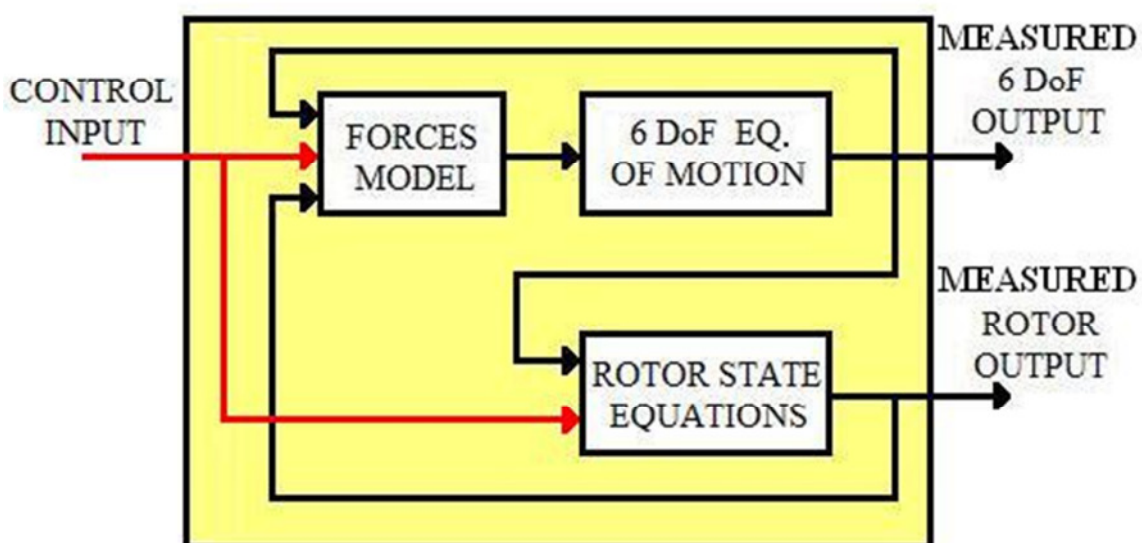
Figure 6.1 – Rotorcraft model functional blocks

6.1.1 Fuselage Model

As already said, the fuselage is modelled as a 6 DoF rigid body, whose equations are assembled by applying Newton's laws of motion, which relate the applied forces and moments to the resulting translational and rotational accelerations. The equations of motion for the fuselage are then Eq. 46 to Eq. 51, described in section 5.1.1. The model of external forces and moments, which represent the input to these equations, is presented in section 6.1.3.

6.1.2 Main Rotor Model

The main rotor model simulates coning, longitudinal and lateral flapping dynamics in multi-blade coordinates. The dynamics are modelled through coupled first order nonlinear system, which includes unknown parameters to be estimated from flight data.

Inputs to the rotor model are the rotorcraft control inputs and the fuselage velocity and angular rate, which are introduced to take into account the effect of the fuselage on the main rotor. The set of inputs, as well as the nonlinear terms included in the model, are selected on the basis of physical meaning and engineering judgment. Outputs of the model are coning angle, longitudinal and lateral flapping deflections and the angular position of the shaft.

The rotor model equations are then the following [AR8]:

Eq. 107
$$\begin{aligned}
\dot{a}_0 = {}& A_1 \cdot a_0 + B_{1,1} \cdot u + B_{1,2} \cdot w + B_{1,3} \cdot \vartheta_{1s} + B_{1,4} \cdot \vartheta_{1c} + B_{1,5} \cdot \vartheta_0 + B_{1,6} \cdot \vartheta_{TR} + \\
& + B_{1,7} \cdot \vartheta_{1s} \cdot \vartheta_{1c} + B_{1,8} \cdot u \cdot \vartheta_{1s} + B_{1,9} \cdot w \cdot \vartheta_0 + B_{1,10} \cdot u^2 \cdot \vartheta_0 + B_{1,11} \cdot v^2 \cdot \vartheta_0 + \\
& + B_{1,12} \cdot w^2 \cdot \vartheta_0 + B_{1,13} \cdot \cos(4\psi) + B_{1,14} \cdot \sin(4\psi) + B_{1,15}
\end{aligned}$$

Eq. 108
$$\begin{aligned}
\dot{a}_1 = {}& A_2 \cdot a_1 + B_{2,1} \cdot b_1 + B_{2,2} \cdot u + B_{2,3} \cdot v + B_{2,4} \cdot w + B_{2,5} \cdot p + B_{2,6} \cdot q + B_{2,7} \cdot r + \\
& + B_{2,8} \cdot \vartheta_{1s} + B_{2,9} \cdot \vartheta_{1c} + B_{2,10} \cdot \vartheta_0 + B_{2,11} \cdot \vartheta_{TR} + B_{2,12} \cdot \vartheta_{1s} \cdot \vartheta_{1c} + \\
& + B_{2,13} \cdot u \cdot \vartheta_{1s} + B_{2,14} \cdot v^2 \cdot \vartheta_{1c} + B_{2,15} \cdot u^2 \cdot \vartheta_0 + B_{2,16} \cdot w^2 \cdot \vartheta_0 + \\
& + B_{2,17} \cdot \cos(4\psi) + B_{2,18} \cdot \sin(4\psi)
\end{aligned}$$

Eq. 109
$$\begin{aligned}
\dot{b}_1 = {}& A_3 \cdot b_1 + B_{3,1} \cdot a_1 + B_{3,2} \cdot a_1 \cdot \vartheta_{TR} + B_{3,3} \cdot u + B_{3,4} \cdot v + B_{3,5} \cdot w + \\
& + B_{3,6} \cdot p + B_{3,7} \cdot q + B_{3,8} \cdot r + B_{3,9} \cdot \vartheta_{1s} + B_{3,10} \cdot \vartheta_{1c} + B_{3,11} \cdot \vartheta_0 + \\
& + B_{3,12} \cdot \vartheta_{TR} + B_{3,13} \cdot \vartheta_{1s} \cdot \vartheta_{1c} + B_{3,14} \cdot u \cdot \vartheta_{1s} + B_{3,15} \cdot v \cdot \vartheta_{1c} + \\
& + B_{3,16} \cdot u \cdot \vartheta_0 + B_{3,17} \cdot v \cdot \vartheta_0 + B_{3,18} \cdot w \cdot \vartheta_0 + B_{3,19} \cdot \sin(4\psi) + B_{3,20}
\end{aligned}$$

where

- (a_0, a_1, b_1) are coning, longitudinal and lateral flap deflection, respectively;

- $(\vartheta_{1s}, \vartheta_{1c}, \vartheta_0, \vartheta_{TR})$ are longitudinal cyclic, lateral cyclic, main rotor collective and tail rotor collective command, respectively;

- ψ is the angular position of the shaft

- A_i and $B_{i,j}$ are the unknown parameters to be estimated from flight data.

The coning is decoupled from the other flapping dynamics, whereas the longitudinal and lateral flapping are coupled. It is worthy to note that depending on the flight condition (hover or forward flight) some of the independent variables in the right hand side of the above equations could be neglected, thus reducing the number of unknowns to be estimated.

In order to estimate independently the unknown parameters in each equation, Eq. 107 to Eq. 109 are rearranged in the form

Eq. 110 $\qquad \dot{a}_0 = A_1 \cdot a_0 + \mathbf{B_1} \cdot \mathbf{U_1}$

Eq. 111 $\qquad \dot{a}_1 = A_2 \cdot a_1 + \mathbf{B_2} \cdot \mathbf{U_2}$

Eq. 112 $\qquad \dot{b}_1 = A_3 \cdot b_1 + \mathbf{B_3} \cdot \mathbf{U_3}$

where $\mathbf{U_1}$, $\mathbf{U_2}$ and $\mathbf{U_3}$ are input vectors, defined as:

Eq. 113
$$U_1 = [u, w, \vartheta_{1s}, \vartheta_{1c}, \vartheta_0, \vartheta_{TR}, \vartheta_{1s} \cdot \vartheta_{1c}, u \cdot \vartheta_{1s}, w \cdot \vartheta_0,$$
$$u^2 \cdot \vartheta_0, v^2 \cdot \vartheta_0, w^2 \cdot \vartheta_0, \cos(4\psi), \sin(4\psi), 1]$$

Eq. 114
$$U_2 = [b_1, u, v, w, p, q, r, \vartheta_{1s}, \vartheta_{1c}, \vartheta_0, \vartheta_{TR}, \vartheta_{1s} \cdot \vartheta_{1c},$$
$$u \cdot \vartheta_{1s}, v^2 \cdot \vartheta_{1c}, u^2 \cdot \vartheta_0, w^2 \cdot \vartheta_0, \cos(4\psi), \sin(4\psi)]$$

Eq. 115
$$U_3 = [a_1, a_1 \cdot \vartheta_{TR}, u, v, w, p, q, r, \vartheta_{1s}, \vartheta_{1c}, \vartheta_0, \vartheta_{TR},$$
$$\vartheta_{1s} \cdot \vartheta_{1c}, u \cdot \vartheta_{1s}, v \cdot \vartheta_{1c}, u \cdot \vartheta_0, v \cdot \vartheta_0, w \cdot \vartheta_0, \sin(4\psi), 1]$$

The rotor model also provides the angular position of the shaft through the following equation:

Eq. 116 $\qquad \dot{\psi} = \Omega_R$

where Ω_R is the main rotor angular speed.

6.1.3 Forces and Moments Model

The external forces and moments acting on the fuselage during flight are classified as gravitational, aerodynamic and inertial. Inertial forces and moments (essentially due to the main rotor) and aerodynamic forces and moments (to which fuselage, main rotor and tail rotor contribute) are subject to identification, whereas the gravitational force is assumed to be known with good accuracy. In fact, also the inertial contribution could be analytically computed [AR18], but actually uncertainties are present, especially on the transmission chain of forces and moments from the blades to the fuselage CoM, therefore, differently from fixed wing case, their model is identified from flight data.

The global force and moment are computed through a lumped parametric model, in which each force or moment component is expressed as parametric function of the vehicle state vector (fuselage plus main rotor), the control inputs and the controls derivatives. This formulation doesn't allow to distinguish the physical source of the aerodynamic term (if it is due to main rotor, fuselage or tail rotor), but it will identify a global vehicle model. For what concerns the inertial contribution, the model assumes that blades are rigid and main rotor inertial forces and moments are not dependent on lag dynamics.

The proposed model structure is based on physical considerations and sensitivities analysis. The force and moment components in fuselage body axes are expressed by:

Eq. 117 $\qquad F_X = \mathbf{\theta_{FX}} \cdot \mathbf{A_{FX}} - mg \sin \Theta$

Eq. 118 $\qquad F_Y = \mathbf{\theta_{FY}} \cdot \mathbf{A_{FY}} + mg \sin \Phi \cos \Theta$

Eq. 119 $\qquad F_Z = \mathbf{\theta_{FZ}} \cdot \mathbf{A_{FZ}} + mg \cos \Phi \cos \Theta$

Eq. 120 $\qquad M_X = \mathbf{\theta_{MX}} \cdot \mathbf{A_{MX}}$

Eq. 121 $\qquad M_Y = \mathbf{\theta_{MY}} \cdot \mathbf{A_{MY}}$

Eq. 122 $M_Z = \boldsymbol{\theta_{MZ}} \cdot \mathbf{A_{MZ}}$

The gravitational force components are shown explicitly. $\boldsymbol{\theta_{IJ}}$ (I = F, M, and J = X, Y, Z) are the vectors of unknown parameters, whereas the signals on the right hand side of the equations, denoted with $\mathbf{A_{IJ}}$, are called regressors and are defined as follows:

Eq. 123 $\mathbf{A_{FX}} = [u, v, w, p, q, r, \vartheta_{1s}, \vartheta_{1c}, \vartheta_0, \vartheta_{TR}, \dot{\vartheta}_{1c}, \dot{\vartheta}_0, a_0, a_1, b_1, \cos(4\psi), \sin(4\psi),$
$\vartheta_{1s} \cdot a_0, \dot{\vartheta}_{1s} \cdot \cos(a_1), a_1 \cdot b_1, 1]$

Eq. 124 $\mathbf{A_{FY}} = [u, v, w, p, q, r, \vartheta_{1s}, \vartheta_{1c}, \vartheta_0, \vartheta_{TR}, a_0, a_1, b_1, \cos(4\psi), \sin(4\psi), a_1 \cdot \cos(4\psi),$
$a_1 \cdot b_1, 1]$

Eq. 125 $\mathbf{A_{FZ}} = [u, v, w, p, q, r, \vartheta_{1s}, \vartheta_{1c}, \vartheta_0, \dot{\vartheta}_0, a_0, a_1, b_1, \cos(4\psi), \sin(4\psi), \vartheta_{TR} \cdot v^2, u^2 \cdot a_1,$
$v^2 \cdot b_1, w^2 \cdot a_0, a_1 \cdot b_1, 1]$

Eq. 126 $\mathbf{A_{MX}} = [u, v, w, p, q, r, \vartheta_{1s}, \vartheta_{1c}, \vartheta_0, \vartheta_{TR}, a_0, a_1, b_1, \cos(4\psi), \sin(4\psi), 1]$

Eq. 127 $\mathbf{A_{MY}} = [u, v, w, p, q, r, \vartheta_{1s}, \vartheta_{1c}, \vartheta_0, \vartheta_{TR}, a_0, a_1, b_1, \cos(4\psi), \sin(4\psi), p \cdot a_1, 1]$

Eq. 128 $\mathbf{A_{MZ}} = [u, v, w, p, q, r, \vartheta_{1s}, \vartheta_{1c}, \vartheta_0, \vartheta_{TR}, \dot{\vartheta}_0, a_0, a_1, b_1, \cos(4\psi), \sin(4\psi), u^2 \cdot \vartheta_{TR}, 1]$

Such as in the rotor model, depending on the flight condition (hover or forward flight) some of the above functional dependences can be neglected, in order to reduce the number of the unknowns to be estimated. The main rotor model receives in input the fuselage state vector while its outputs are used for the computation of the force and moment acting on the fuselage. In this way the fuselage main rotor coupling is correctly taken into account by the model.

In the literature, it has been shown that this model has good predictive capability for both aerodynamic [B1], [B24], and inertial forces [B72].

6.2 Identification Strategy and Techniques

The rotorcraft model identification is performed in the framework of a three-step approach, which allows specifying a suitable methodology compliant with each step objective and to exploit the advantage of both time-domain and frequency-domain methods. Indeed a hybrid

time-frequency estimation strategy is applied. Before starting the first identification step, a compatibility check is performed using kinematic relations, in order to check the flight measurements consistency and the correctness of the measurement errors characterisation.

The first identification step reconstructs the vehicle flight path by using the Unscented Kalman Filter. This is a preliminary step because it computes data (the time histories) needed by the following identification steps but it doesn't provide an estimation of unknown parameters included into the model. The second identification step aims at estimating all the unknown parameters of the rotor model. It is carried out in the frequency domain, because rotor dynamics are usually characterised by wide frequency range and frequency identification techniques allow defining the frequency range where the model should be identified. Finally, the estimation of all the unknown parameters of the forces and moments model is carried out in the third identification step. This step is performed in the time domain.
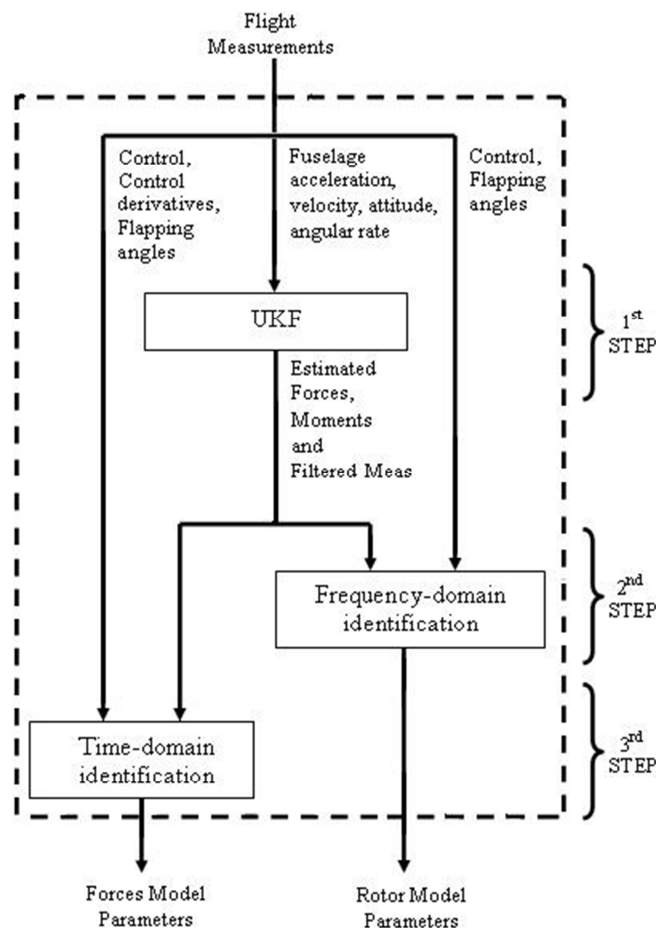

Figure 6.2 – Flowchart of the rotorcraft identification process

The Flow-chart of identification process is shown in Figure 6.2 and the methodologies applied in each identification step are detailed described in the following sections.

It is worth noting that, differently from the re-entry vehicle case, optimal flight tests can be designed and performed for gathering experimental data to be used for rotorcraft model identification.

6.2.1 First Identification Step

The first identification step is carried out in the time domain solving a nonlinear filtering problem by means of the Unscented Kalman Filter. The filtering is performed using a non-augmented algorithm for the UKF, according to the description provided in section 4.2.1, in order to reduce the filter state vector dimension [AR9]. It provides the estimation of the flight trajectories of fuselage state vector and global external forces (except for weight, which is assumed known) and moments acting on the vehicle's fuselage during the test. The associated estimation errors characterisation is also evaluated.

The prediction phase of the filter requires the definition of the filter model, which includes the six degrees of freedom rigid body equations of motion (Eq. 46 to Eq. 51), to predict the time evolution of the fuselage state vector. All the states of the fuselage are measured. Process and measurement noises for the fuselage model are assumed additive. The covariance matrix of process noise is a design parameter of the filter, whereas the covariance matrix of measurement noise is defined by the datasheet of the on board sensors.

The UKF considers the unknowns as augmented states of the model, therefore the dynamic behaviour of the external forces and moments has to be modelled, too, in order to complete the filter state equations. To this aim, periodic random models [B60] are introduced, considering that the main relevant force acting on the fuselage during the flight is produced by the rotor and is periodic. Order of the periodic model, values of characteristic parameters and process noise covariance matrix are determined before flight, performing Monte Carlo simulations of the mission and analysing the autocorrelation function of simulated force and moment [AR12]. For the examined rotorcraft mission, second order periodic random processes are selected to model force and moment components in body axes. The mathematical representation of the model in the state space for the ith unknown is:

Eq. 129 $\qquad \dot{x}_{i1} = x_{i2} + \eta_{ix1}$

Eq. 130 $\qquad \dot{x}_{i2} = -\alpha_{ip}x_{i1} - 2\beta_{ip}x_{i2} + \left(\alpha_{ip} - 2\beta_{ip}\right)\eta_{ix2}$

where x_{i1} is the unknown (force or moment component), x_{i2} is an auxiliary state, α_{ip} and β_{ip} are characteristic parameters of the model and η_{ix1} and η_{ix2} are process noises.

The parameters of the model are tuned in order to fit the mean autocorrelation computed numerically from the simulated flight data provided by the Monte Carlo analysis. An example of this result is shown in Figure 6.3 for the X-axis force component and the pitching moment component during a typical identification manoeuvre.

It is worth noting again that the above described forces and moments model selection is executed in pre-processing, before analysing the flight data; it isn't a result of the first identification step. In fact the outputs of this step are the time histories of external forces and moments and not their model. Eq. 129 and Eq. 130 are only introduced to allow the UKF correctly works.
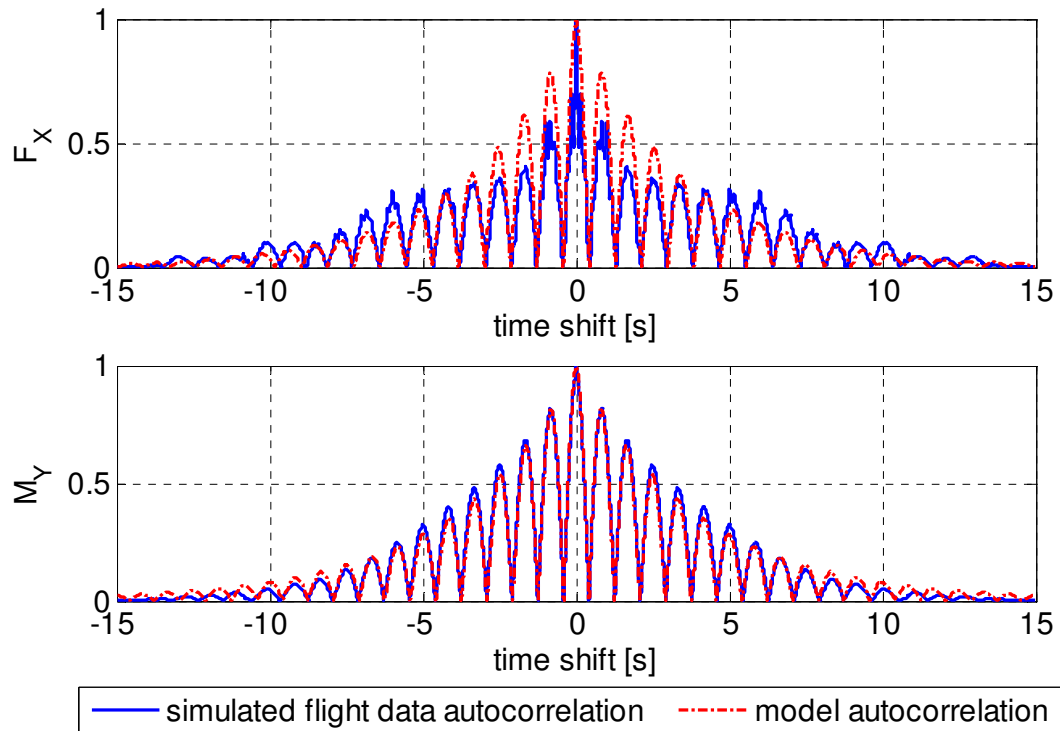
Figure 6.3 – Comparison between the modelled autocorrelation and the one computed from simulated flight data for F_X and M_Y components acting on the vehicle during a tail rotor 3-2-1-1 manoeuvre from hover

In the correction phase of the filter, the flight measurements of fuselage CoM acceleration and velocity, and fuselage angular rates and attitude are used to correct the predicted estimations.

The time histories estimated in the first step and the characterisation of the estimations errors are provided in input to the following steps.

6.2.2 Second Identification Step

Second identification step is performed in the frequency domain using the methodology proposed in [B39] and described in section 4.2.4. This technique estimates the unknown parameters by minimizing the sum of square differences between measured data and corresponding values provided by the model on a selected frequency range. The choice of the frequency range allows focusing on the estimation of the parameters associated to the desired dynamics.

The proposed approach applies this technique to Eq. 110, Eq. 111 and Eq. 112, in order to estimate all the parameters of the rotor dynamics model. Inputs to the second identification step are the estimation results of the first identification step, plus the flight measurements of control inputs, main rotor coning, longitudinal and lateral flapping angles.

Finally, Eq. 40 allows computing the estimation error and therefore characterizing the identified model uncertainty.

6.2.3 Third Identification Step

The estimation of the unknown parameters of the forces and moments model, described by Eq. 117 to Eq. 122, is performed in this identification step. The estimation is carried out independently for each force or moment component equation. Since the model is static, the LS estimation methodology is applied, according to the description provided in section 4.2.2. Alternatively, if the model is dynamic, the UKF could be applied, or other time domain methodology for the estimation of constant unknown parameters, such as the Maximum Likelihood Estimation (MLE) technique [AR13], [B1].

Inputs to this step are the time histories of forces, moments and filtered flight measurements estimated in the first identification step and measured flight data of vehicle control inputs, main

rotor coning and flapping angles. Data gathered during different flight tests can be concatenated and provided in input as a unique data set to be processed.

The uncertainties on the inputs, provided by the first identification step or from the sensors datasheet, are also taken into account in order to evaluate the uncertainty on the identified model. To this end, many estimations of the same unknown parameters are carried out in a Monte Carlo analysis, by using in input flight measurements and global aerodynamic coefficients randomly selected in their range of uncertainty. The statistics of the estimated parameters are then evaluated and used to define the estimation uncertainty on each of the evaluated parameters.

7 NUMERICAL ASSESSMENTS

Before applying the proposed methodology to actual flight data, it was validated in simulation, for both the examined vehicles. This chapter presents the numerical assessment results.

7.1 Re-entry Space Vehicle Identification

7.1.1 Simulation Model for Flight Data Generation

Simulated flight data, provided in input to the identification process, were generated using a complete model of the CIRA FTB1 vehicle, also featuring a detailed description of flight control system, vehicle aerodynamics, actuators, sensors, and environmental disturbances. The vehicle model is based on the classical rigid body nonlinear equations of motion, in agreement with the relations introduced in section 5.1.1. Vehicle state vector is composed of Centre of Mass position and velocity components, attitude angles, and angular rates. Algebraic expressions for the computation of aerodynamic angles, Mach number and dynamic pressure, are also included in the model. Vehicle aerodynamic behaviour is modelled using the tabular pre-flight database, obtained by means of wind tunnel tests and computational fluid dynamics analyses [B57]. It is worthwhile to note that the structure of model to be identified is different from the one used in simulation. It introduces a modelling error that is present also when actual flight data are examined. The detailed description of the CIRA FTB1 vehicle is reported in section 8.1.

The atmospheric model is based on the meteorological data of the European Centre for Medium-Range Weather Forecasts, that provides baseline profiles for wind velocity, air temperature and pressure during the mission. These profiles are corrected by means of Gauss-Markov processes [B59], introduced to simulate high frequency variations.

The sensors measure load factors, attitude angles, angular rate, aerodynamic angles, Mach number and aerodynamic effectors deflections. All data are sampled at 100 Hz and are affected by additive measurements Gaussian noise, characterised by the sensors datasheets as reported in Table 7.1.

The simulation model was implemented in MATLAB/SIMULINK environment. Its first level block diagram is shown in Figure 7.1.

Measurement	*Load factor*	*Angular rate*	*Roll and Pitch Euler angles*	*Yaw Euler angle*	*Aerodynamic angles*	*Mach number*
Noise standard deviation	0.025 m/s^2	0.015 deg/s	0.1 deg	1deg	1 deg	0.004

Table 7.1 – Standard deviations of measurement noises
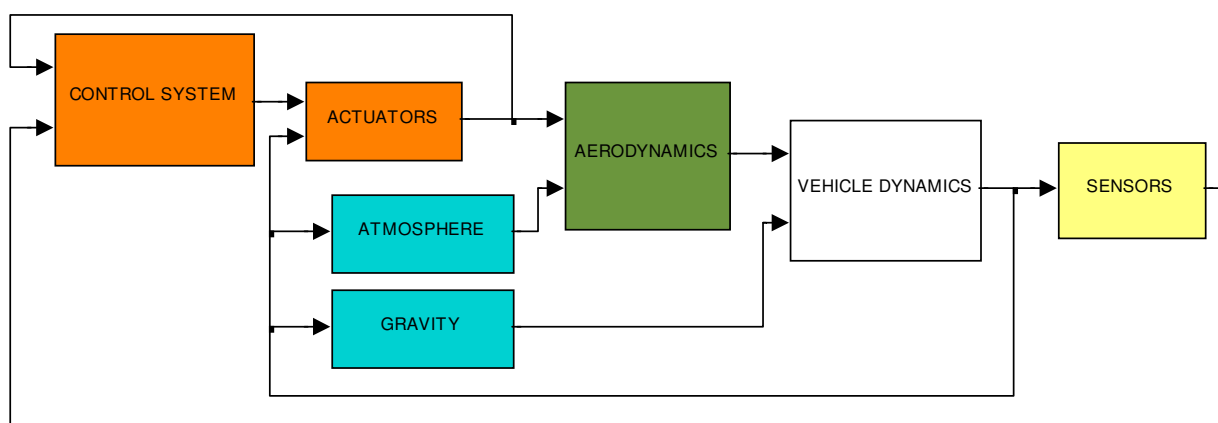
Figure 7.1 – First level block diagram of SIMULINK simulation model used for flight data generation

Before providing the flight measurements as input to the identification process, a compatibility check based on kinematic relations was carried out on the data [B1], in order to check their consistency.

7.1.2 Flight Tests Design

The CIRA Dropped Transonic Flight Test 2 (DTFT2) mission was simulated in order to collect flight data for the numerical validation of the proposed system identification methodology.

The DTFT2 mission operations are detailed described in section 8.2. In simulation, the controlled gliding flight phase is only reproduced. The simulated profiles of flight measurements, that is, load factors, angular rates, aerodynamic angles, Mach number and aerodynamic effectors deflections are shown in Figure 7.2 to Figure 7.5 for the nominal trajectory. Besides the nominal trajectory, other trajectories were randomly generated, varying the aerodynamic parameters, the measurement noises and the environmental disturbances within their uncertainty ranges. The obtained angle of attack time histories and Mach-altitude plots are presented in Figure 7.6 and Figure 7.7, respectively.
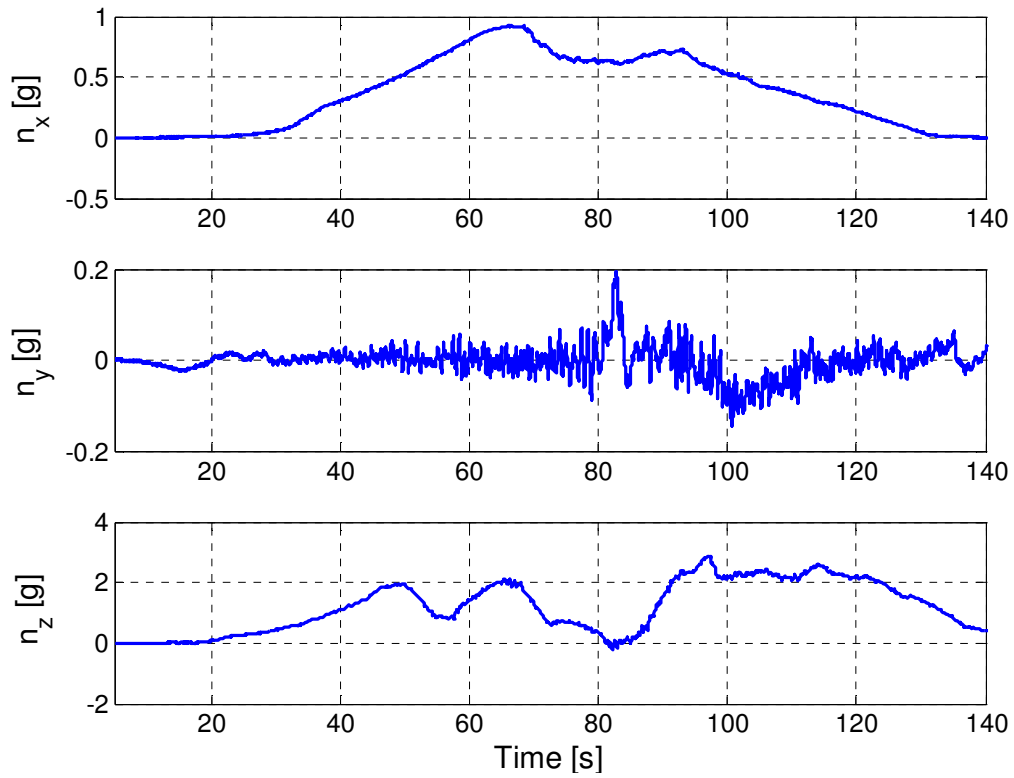
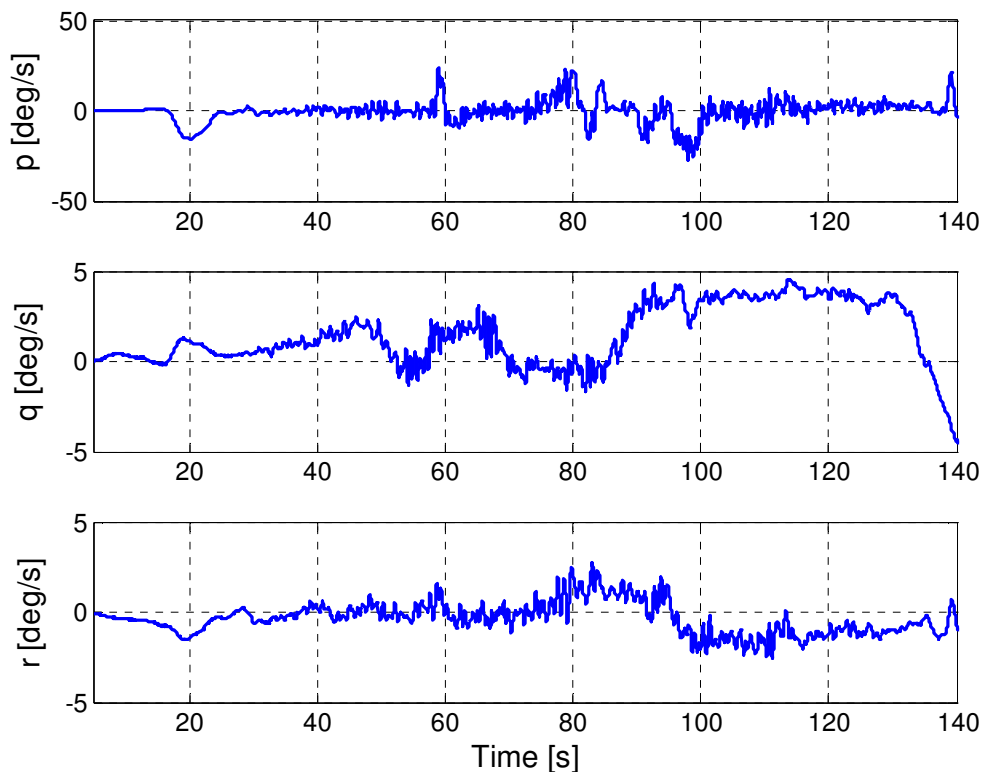**Figure 7.2 – Nominal trajectories of load factors for DTFT2 mission**

Figure 7.3 – Nominal trajectories of angular rate components for DTFT2 mission
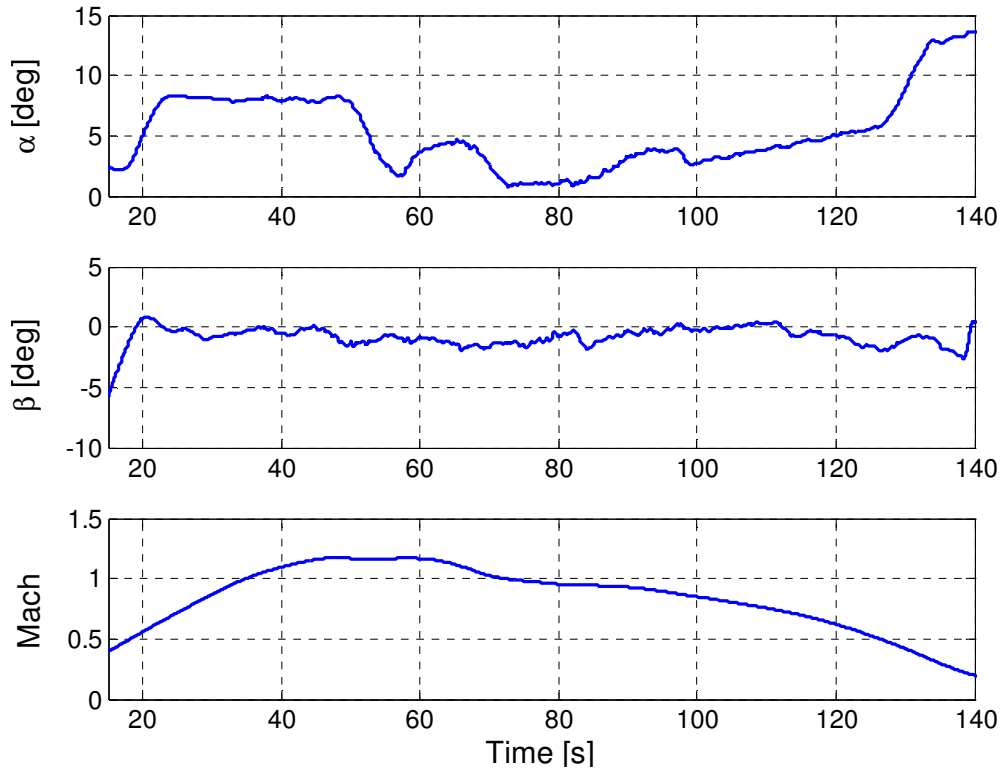
Figure 7.4 – Nominal trajectories of aerodynamic angles and Mach number for DTFT2 mission
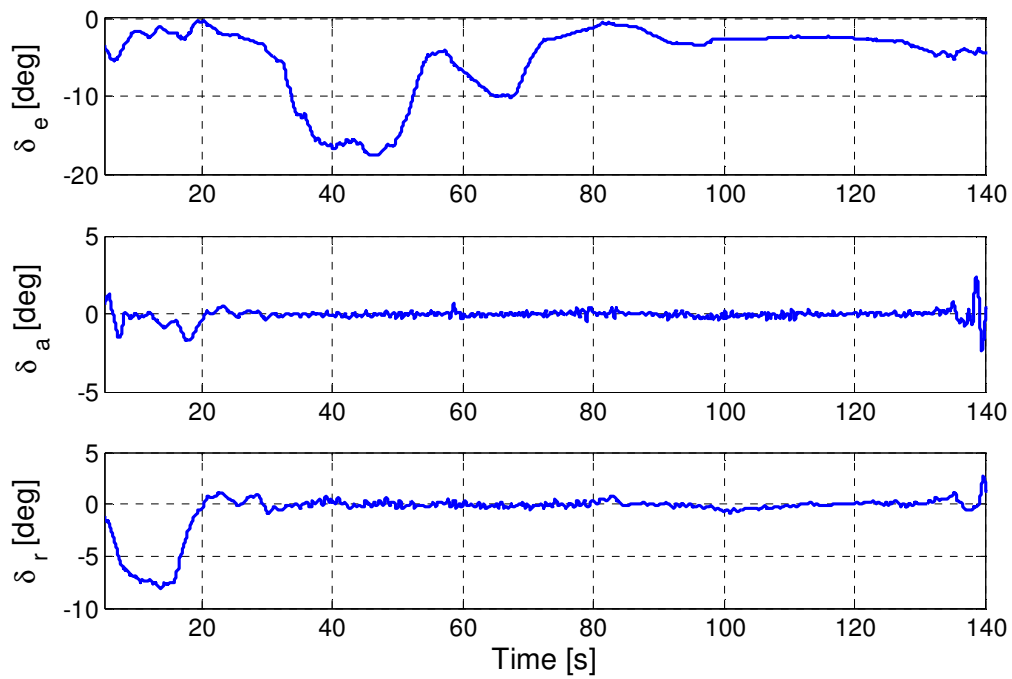

Figure 7.5 – Nominal trajectories of aerodynamic effectors deflections for DTFT2 mission
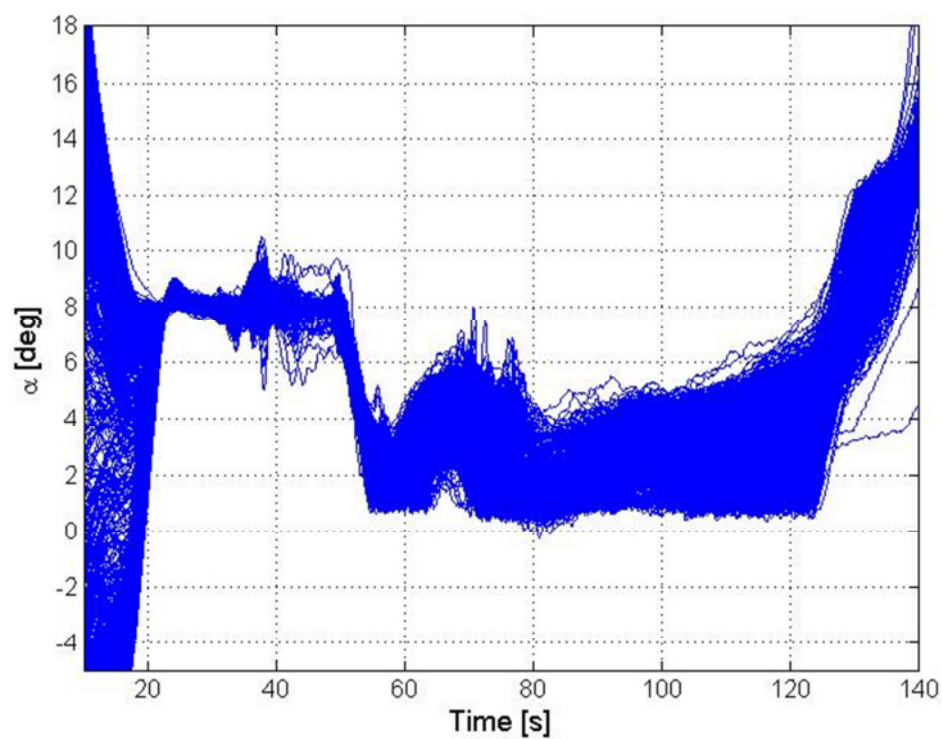
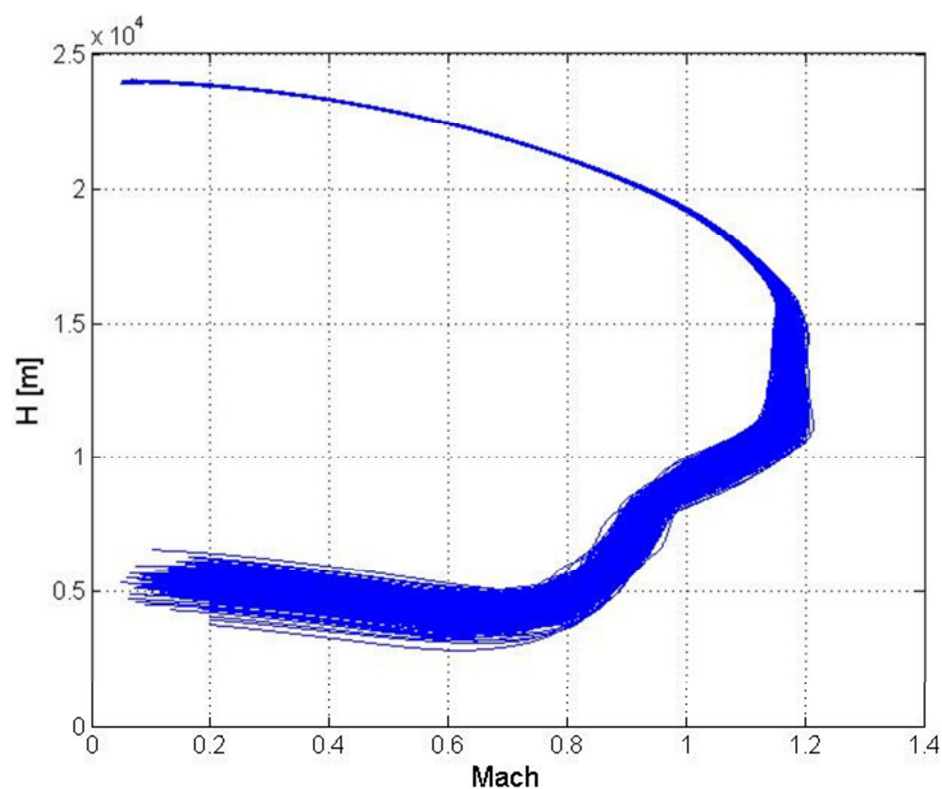**Figure 7.6 – Dispersed trajectories of angle of attack for DTFT2 mission**

Figure 7.7 – Dispersed profiles of Mach number versus altitude for DTFT2 mission

It is worthy to note that due to safety reason, specific manoeuvres aimed at system identification purpose were not executed during the flight test.

7.1.3 *Model Identification Results*

The analysis of the model identification results from simulated flight data allows evaluating the effectiveness of the proposed methodology, because the knowledge of the true values of time histories and model parameters can be exploited.

7.1.3.1   First Identification Step Results

The first identification step provides the estimation of flight trajectory for global aerodynamic coefficients, wind velocity, atmospheric pressure and temperature, filtered vehicle state vector and measurements. These estimations for the nominal trajectory are shown from Figure 7.8 to Figure 7.12 [AR12].

The estimated trajectories of the aerodynamic coefficients are presented in Figure 7.8, where they are compared with the corresponding true trajectories. Estimated and true trajectories are practically indistinguishable. In Figure 7.9 the estimation error trajectories are reported for each aerodynamic coefficient, together with the trajectories of the uncertainty on the estimation, provided by the UKF, too. The error is almost always consistent with the uncertainty, confirming that the UKF provides reliable value for the accuracy of the estimation. Finally the identified uncertainty is significantly lower than the pre-flight one, as shown in Figure 7.10, where pre and post identification uncertainties are compared.

The estimated trajectories of horizontal components of the wind speed are presented in Figure 7.11. They are compared with the true trajectories and the with the meteorological data, which are affected by error. The estimations match the true values and extend the frequency content of the wind speed trajectories with respect to the meteorological information. Also the estimations of air pressure and temperature fit the true values, which does not differ significantly with respect to the meteorological data. They are not presented here for the sake of brevity.

Finally, Figure 7.12 presents the aerodynamic angles, which are the most noisy measured data. The UKF estimations are compared with the simulated flight measurements (affected by noise) and the corresponding true values. Only a short part of the trajectories is shown, in order to

reduce the plot scale and to enhance the effects of the filter. Indeed, the UKF is able to filter out the noise and to reconstruct the true behaviour of the examined variables. Similar results are obtained along the whole trajectory and for all the flight measurements.

The simulated flight data of 100 trajectories, obtained through the Monte Carlo simulations described in section 7.1.2, were also examined, in order to further assess the UKF estimation capability. The main statistics of the UKF error on the aerodynamic coefficients estimation are listed in Table 7.2. These results confirm the reliability of first identification step output.

Aerodynamic coefficient		C_L	C_D	C_Y	C_l	C_m	C_n
RMS	**Mean**	0.00013	7.93e-5	8.24e-5	8.61e-8	8.09e-5	6.51e-6
	Standard deviation	8.63e-5	6.60e-5	6.50e-5	8.81e-9	6.13e-6	5.06e-7

Table 7.2 – Error statistics on UKF estimation for 100 flight trajectories
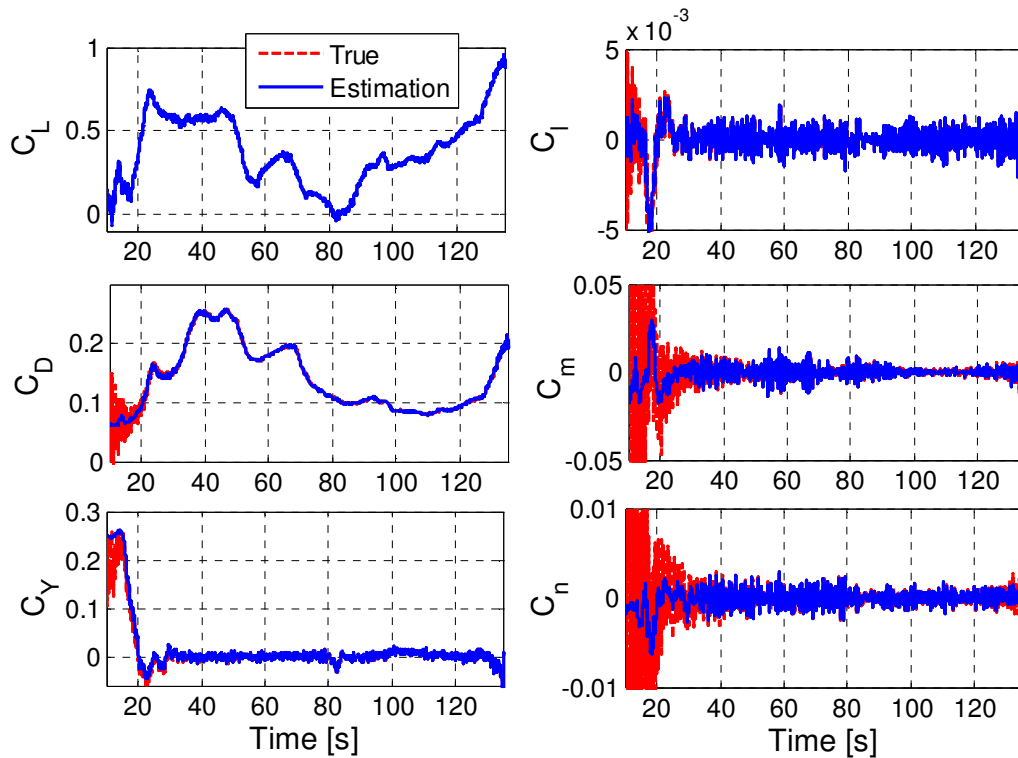
Figure 7.8 – Comparison between estimated and true trajectories of the aerodynamic coefficients
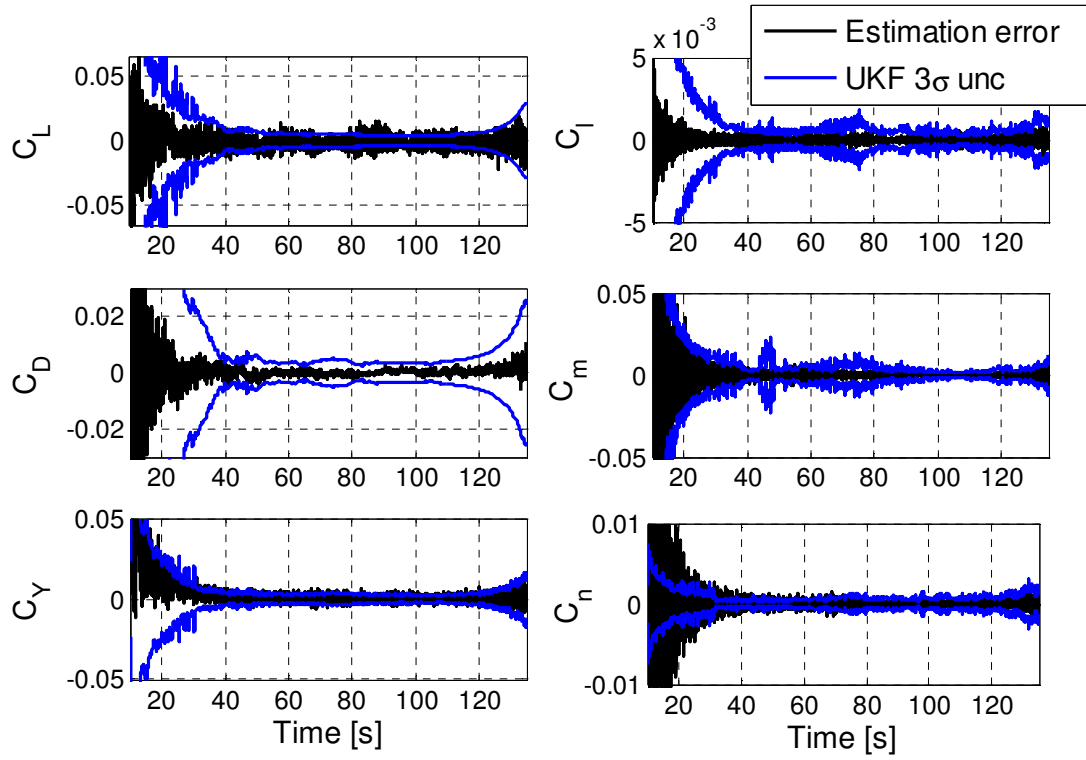
Figure 7.9 – Comparison between estimation error and uncertainties on the estimation provided by the UKF
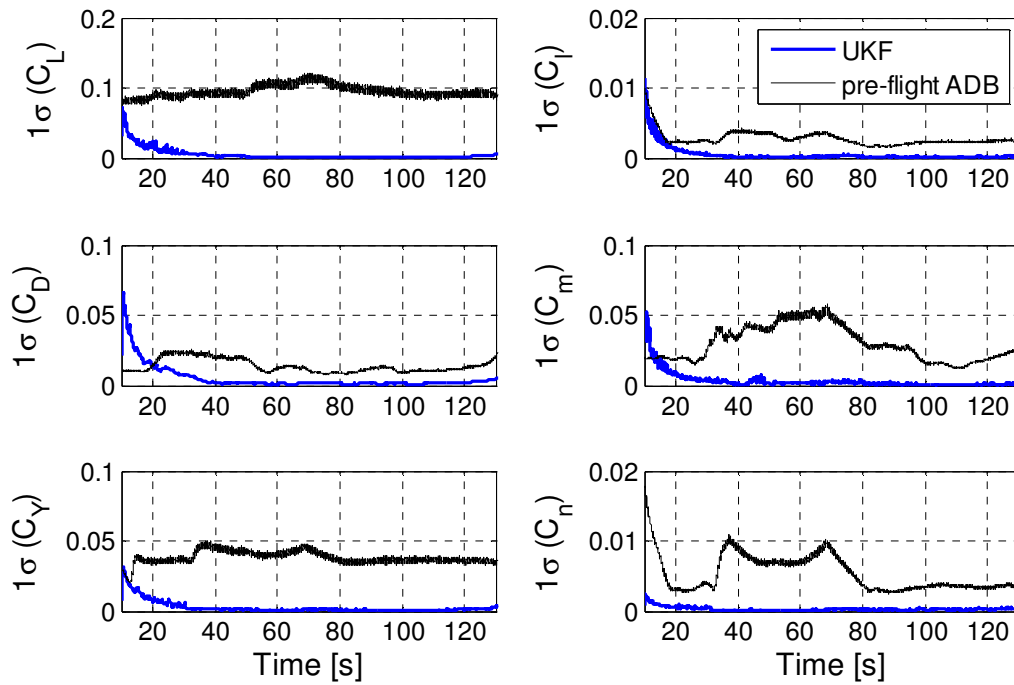

Figure 7.10 – Comparison between pre-flight and estimated aerodynamic uncertainties
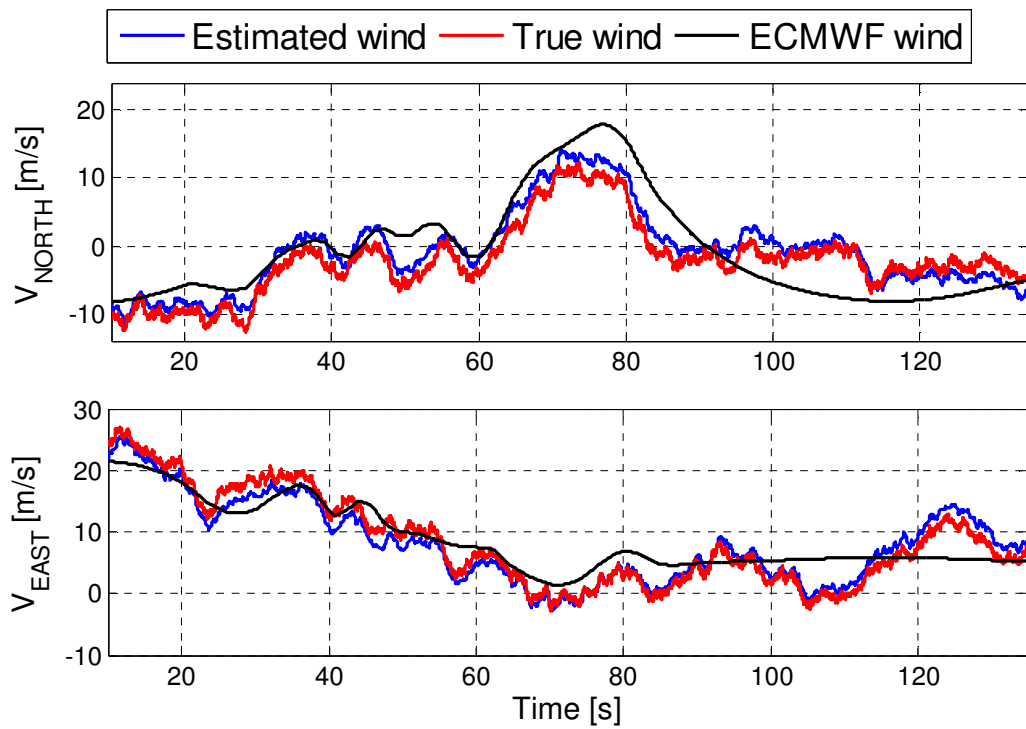
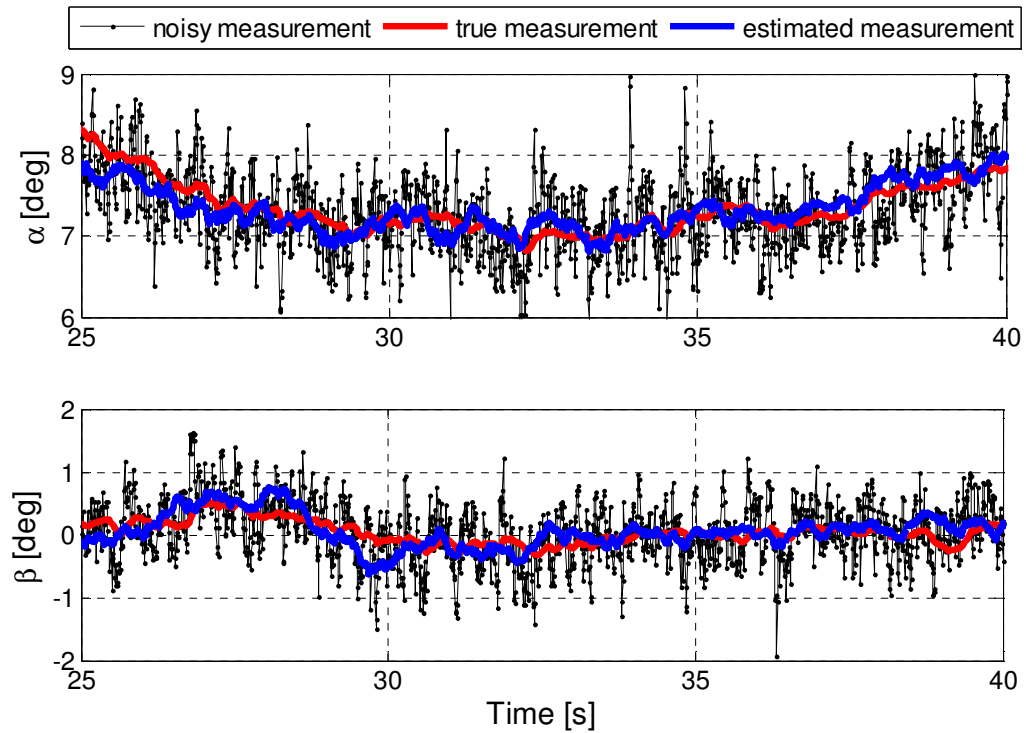**Figure 7.11 – Comparison among estimated, true and ECMWF trajectories of wind speed**

Figure 7.12 – Comparison among noisy, true and estimated flight measurements of aerodynamic angles

7.1.3.2 Second Identification Step Results

The subset of the aerodynamic model parameters to be estimated in the second step were selected through an identifiability analysis based on Cramer-Rao bounds. 21 parameters were identified from the simulated flight data by using the UKF, following the first approach described in section 5.2.2 [AR12].

The estimated values are listed in Table 7.3 and Table 7.4 (for subsonic and supersonic flight regimes, respectively), together with the corresponding true values and the estimation uncertainties. It is worthy to note that the structure of the aerodynamic model used for simulated flight data generation, that is the pre-flight aerodynamic database, is different from the structure of the identified aerodynamic model, which is the analytical model presented in section 5.1.2. The true values of the aerodynamic parameters reported in the tables are computed before performing the identification from flight data, by minimizing the error between pre-flight database and analytical model on the whole flight envelope. However this error, denoted as modelling error, is not zero everywhere also if the true values of the parameters are used, because it depends on the structure of the analytical model.

The initial guesses for the identification from flight data are set equal to 1.3 times the true values. The UKF converges to a constant value, as shown in Figure 7.13 for two of the unknowns, namely the gains related to the derivatives $C_{n\beta}$ and $C_{l\delta a}$, in subsonic and supersonic regime, respectively. The estimated values of the gains associated to all the main longitudinal and some lateral-directional aerodynamic derivatives are very good, whereas the estimation of the gains related to the subsonic zero-order terms of lift and pitch moment coefficients is good. The estimates of standard deviations, a measure of estimation uncertainty, are in general very low and coherent with the estimation error, but for some parameters related to lift coefficient derivatives (in particular, only the standard deviation of $C_{L\delta e}$ is unacceptable, maybe due to identifiability problem). The computed standard deviations are in general lower than their pre-identification values, showing an improvement varying between 34% and 90%. Better results, in terms of uncertainty reduction and increased number of estimated parameters, could be obtained if specific identification manoeuvres are performed during the mission to improve the identifiability of the aerodynamic model.
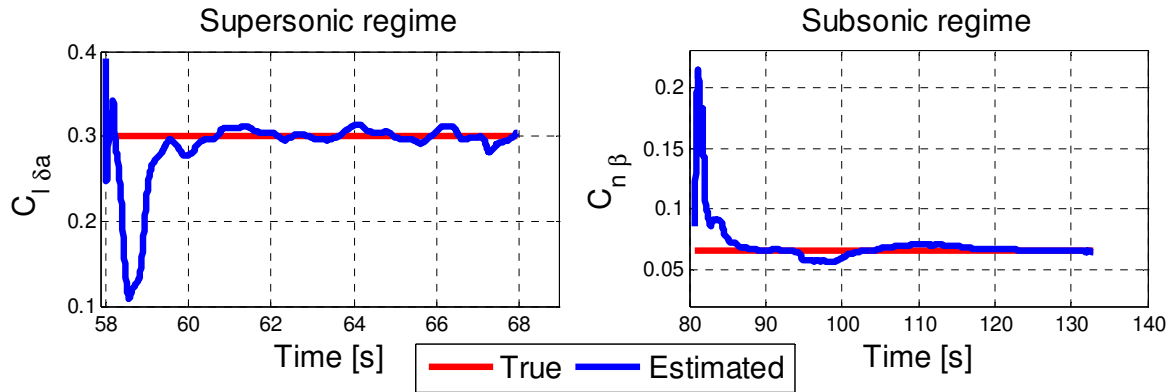
Figure 7.13 – UKF estimations of constant aerodynamic parameters

Gain related to	True value	Estimation	Standard deviation
$C_{L\,0}$	0.038	0.057	9.7e-3
$C_{L\,\alpha}$	4.29	4.244	0.132
$C_{L\,\delta e}$	1.55	1.67	9.99
$C_{D\,0}$	0.062	0.062	2.8e-3
$C_{D\,\alpha}^{2}$	4.078	3.828	0.090
$C_{m\,0}$	-0.0421	-0.052	1.6e-3
$C_{m\,\alpha}$	0.144	0.137	7.2e-3
$C_{m\,\delta e}$	-1.391	-1.382	0.024
$C_{Y\,\beta}$	-2.05	-2.119	0.015
$C_{l\,\beta}$	-0.049	-0.044	6.3e-4
$C_{l\,p}$	-0.405	-0.370	4.2e-3
$C_{n\,\beta}$	0.0656	0.0651	7.5e-4

Table 7.3 – Subsonic aerodynamic parameters estimated in the second identification step

Gain related to	True value	Estimation	Standard deviation
$C_{L\,0}$	-0.29	-0.267	0.208
$C_{L\,\alpha}$	7.98	8.095	0.196
$C_{L\,\delta e}$	0.803	0.788	0.375
$C_{D\,0}$	-1.30	-1.31	3.5e-3
$C_{D\,\alpha}^{2}$	4.75	4.86	0.040
$C_{m\,\alpha}$	-0.23	-0.23	1.7e-3
$C_{l\,\delta a}$	0.30	0.30	6.9e-3
$C_{l\,\delta r}$	0.66	0.58	0.016
$C_{n\,\delta a}$	0.13	0.12	1.8e-3

Table 7.4 - Supersonic aerodynamic parameters estimated in the second identification step

It is worth to note that the estimation results could significantly vary, depending on initial trial of the unknowns and filter tuning parameters, therefore they should be selected carefully. The Least Square estimation is not affected by this problem, therefore both the estimation techniques are applied to actual flight data.

7.1.4 Model Validation

In simulation, the assessment of the results could be performed comparing the estimated values and trajectories with the true ones, which are known. This approach has already been presented in the previous section. A further validation of the identified model was performed following the procedure described at point 3.V of section 4.3.

The identified analytical aerodynamic model was integrated into the simulation model shown in Figure 7.1, replacing the pre-flight aerodynamic database. The control system was removed and open loop simulations were carried out, using as input the aerodynamic effectors deflections. The outputs of the simulations were compared with the simulated flight data, in order to assess the capability of the identified model to reproduce the phenomena experimented by the vehicle in flight. This type of validation is very critical because small identification errors can lead to the divergence of the simulation, due to the absence of a flight control system which allows tracking the reference trajectory.

Three types of simulations were performed:

1. The identified model was used to compute all the aerodynamic force and moment coefficients.

2. The identified model was used to compute only the aerodynamic force coefficients (lift, drag and side force); the aerodynamic moment coefficients were provided as input to the model using the time histories estimated by the UKF in the first identification step.

3. The identified model was used to compute the lateral-directional aerodynamic force and moment coefficients (side force, roll and yaw moments); the longitudinal aerodynamic coefficients were provided as input to the model using the time histories estimated by the UKF in the first identification step.

In the first case the model outputs diverged from the flight measurements, whereas very good matching of the flight measurements were obtained in the other two cases. Model outputs and corresponding flight measurements for case 2 are presented from Figure 7.14 to Figure 7.17, similar results are obtained for case 3 (not reported for the sake of brevity). Table 7.5 shows the Theil's coefficients for cases 2 and 3. These coefficients are used to assess quantitatively the fitting of the flight measurements. For all the considered variables, the coefficients are significantly lower than 0.25, which represents the threshold corresponding to good matching of the data.

The obtained results enhance that the identified pitching moment coefficient was mainly responsible for the simulation divergence in case 1, although the estimation errors on the related parameters were small, as shown in Table 7.3 and Table 7.4. It means that the modelling error on this aerodynamic coefficient is not negligible along the DTFT2 trajectory and/or the sensitivity of the model outputs with respect to this error is very high. It was taken into account when actual flight data were examined to identify the aerodynamic model.
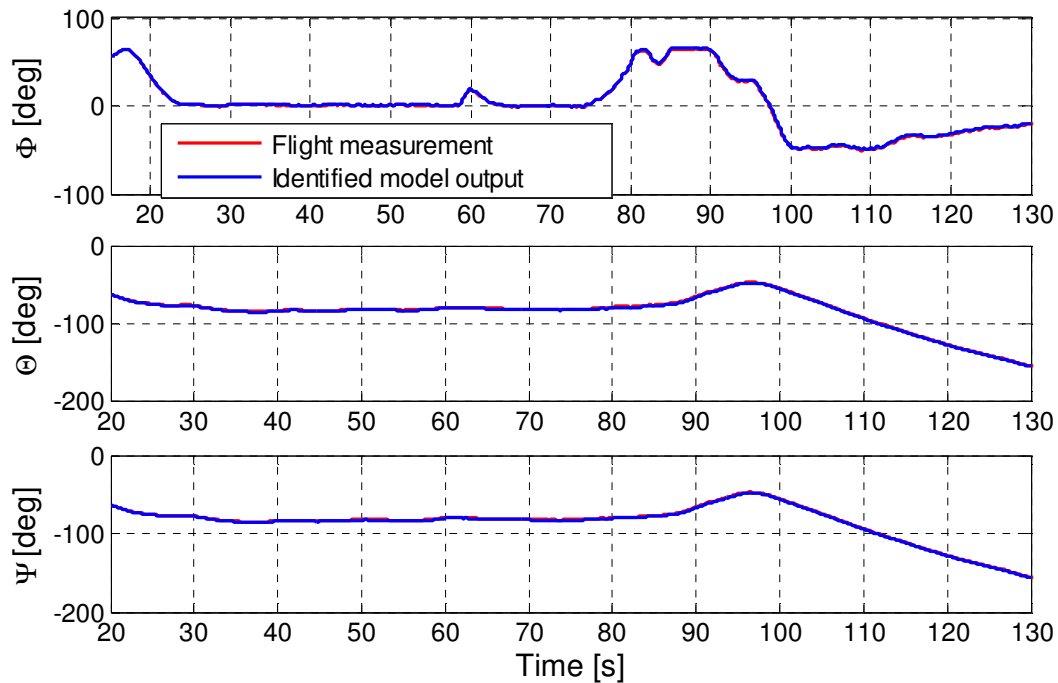
Figure 7.14 – Comparison between identified model outputs and simulated flight measurements of Euler angles along the DTFT2 trajectory
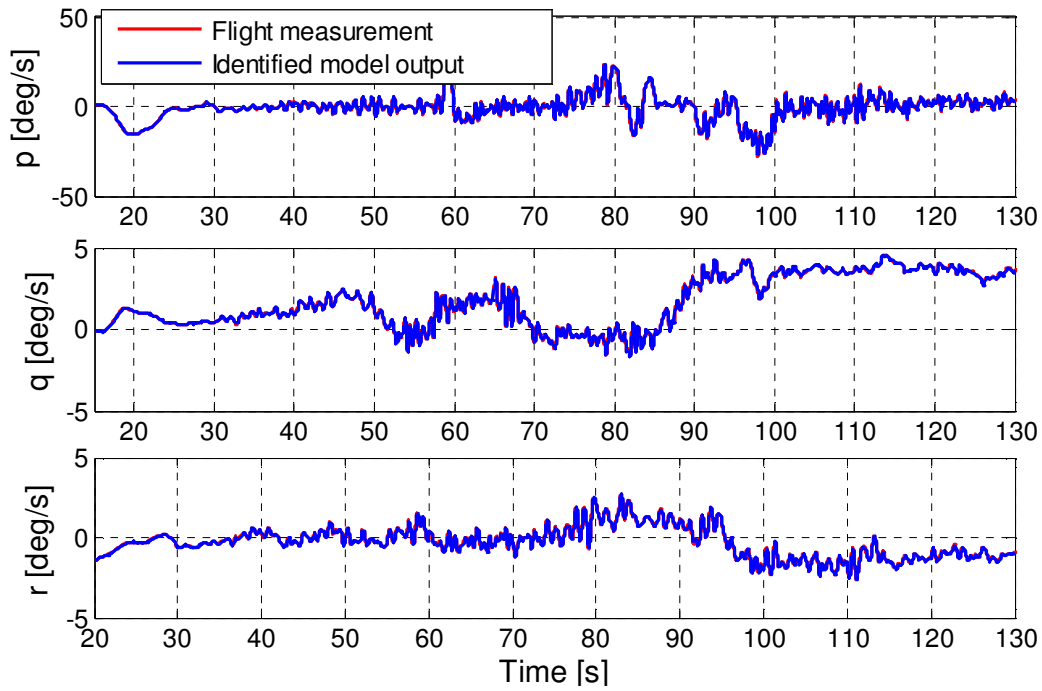
Figure 7.15 - Comparison between identified model outputs and simulated flight measurements of angular rate components (in body axes) along the DTFT2 trajectory
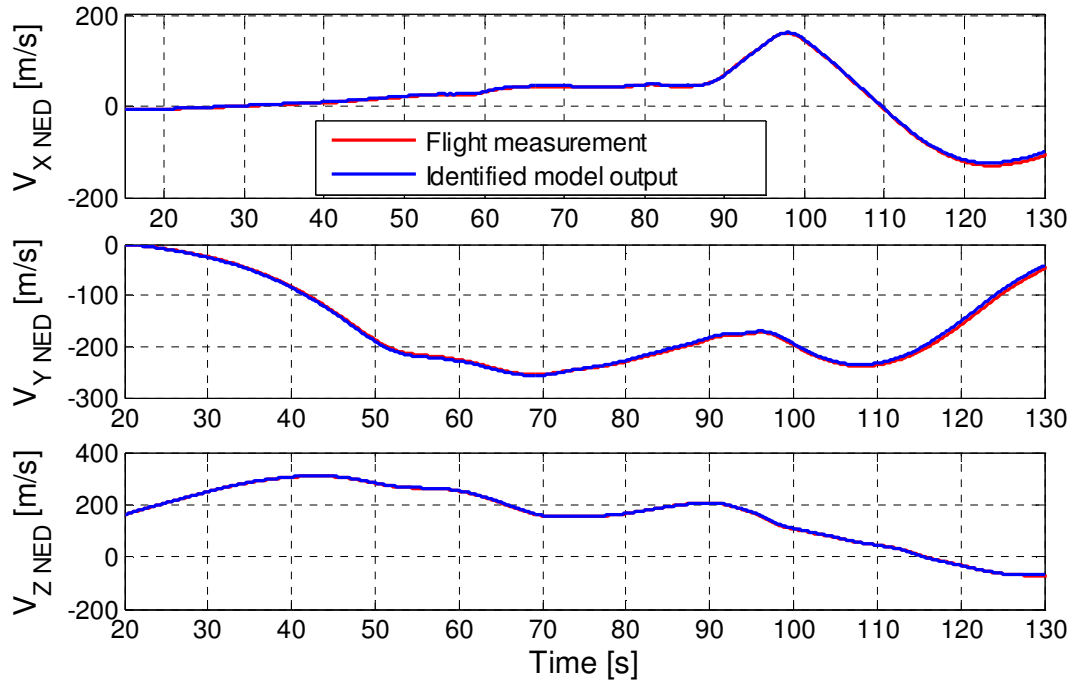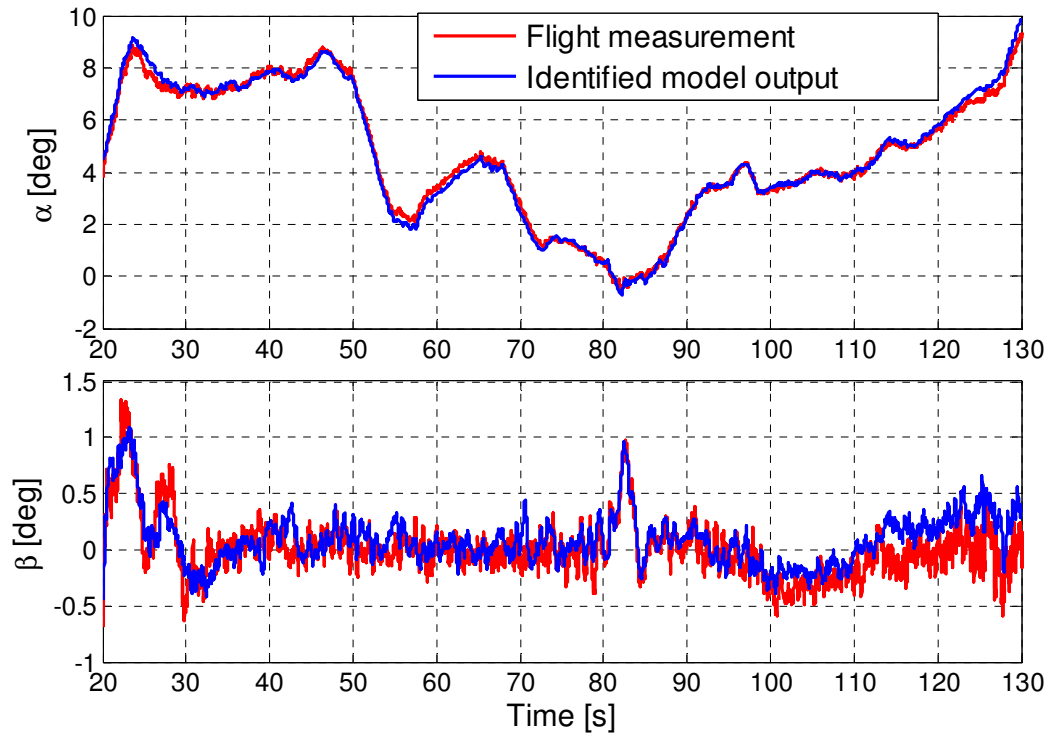

Figure 7.16 - Comparison between identified model outputs and simulated flight measurements of CoM velocity components (in NED reference frame) along the DTFT2 trajectory

Figure 7.17 - Comparison between identified model outputs and simulated flight measurements of aerodynamic angles along the DTFT2 trajectory

Measurement	Theil's Coefficients	
	Validation case 2	**Validation case 3**
roll angle	0.013	0.013
pitch angle	0.004	0.004
yaw angle	0.004	0.004
roll rate	0.060	0.059
pitch rate	0.017	0.017
yaw rate	0.039	0.039
north velocity	0,018	0.026
east velocity	0.001	0.005
down velocity	0.003	0.006
angle of attack	0,022	0.079
angle of sideslip	0,111	0.137

Table 7.5 – Theil's coefficients

7.2   Rotorcraft Model Identification

7.2.1 Simulation Model for Flight Data Generation

The simulation model of the UH60 Black Hawk [B73] was implemented in the FLIGHTLAB Software Environment and used for simulated flight data generation. The rotorcraft model is nonlinear and includes detailed description of main rotor, tail rotor and fuselage. The main rotor is four-bladed with flap and lag articulation provided at the blade root by electrometric bearings. The rotor blade elastic characteristics are introduced via nonlinear flexible beam elements and the rotor aerodynamic model includes a 2D indicial formulation to account for the blade sectional air loads unsteadiness. The rotor induced flow dynamics is modelled using the Peters-He finite state wake model with 15 state variables [B74]. Pertinent rotor parameters are listed in Table 7.6, together with the inertial properties of the fuselage. The tail rotor is modelled as a four bladed Bailey rotor with radius of 5.5 feet and angular speed of 124.62 rad/s. The simulation model only describes the vehicle dynamics, wind and turbulence are not modelled. It is worthy to note that the model used for data generation is significantly more complex with respect to the one adopted for identification purpose and described in section 6.1, in particular for what concern the rotor dynamics and external force.

Figure 7.18 – UH60 Black Hawk

Parameter	Value
Number of Blades	4
Radius	27.0 ft (8.23 m)
Chord	1.73 ft (0.53 m)
Rotor Disk Area	2290.2 ft^2 (212.77 m^2)
Rotor Blade Area	186.8 ft^2 (17.35 m^2)
Solidity Ratio	0.0816
Main Rotor Speed	27 rad/s
Nominal Tip Speed	729 ft/s (222.2 m/s)
Blade Airfoils	NACA0012
Feathering hinge offset	1.2 ft (0.36 m)
Flap hinge offset	1.2 ft (0.36 m)
Lag hinge offset	1.3 ft (0.39 m)
Fuselage weight	16434 lbf (7554 Kg)
I_{xx}	10037 slug·ft^2 (13608 Kg m)
I_{yy}	44565 slug·ft^2 (60422 Kg m)
I_{zz}	44183 slug·ft^2 (59904 Kg m)
I_{xy}	0 slug·ft^2
I_{xz}	-1497 slug·ft^2 (-2030 Kg m)
I_{yz}	0 slug·ft^2

Table 7.6 – Rotorcraft data

The simulation model was used to generate the flight measurements of:

- fuselage CoM acceleration and velocity, in body reference frame;

- fuselage angular acceleration, angular rates and attitude;

- actual control inputs (collective pitch, longitudinal and lateral cyclic pitch, tail rotor collective pitch);

- main rotor rotational frequency and flapping angles (expressed in multi-blade coordinates).

A white zero mean Gaussian noise was added to the fuselage measurements provided by the model, in order to simulate the sensors measurement errors. The standard deviations of Gaussian measurements noises are shown in Table 7.7, derived from a typical COTS inertial systems. Measurement noise is supposed negligible for the input controls and the rotor measurements.

Furthermore the true measurements of external forces and moments acting on the fuselage during the flight tests were recorded. Although these measurements were not provided as input to the

identification process, they were required in order to perform a validation of the first step identification results.

The data were originally sampled at 1538 Hz, that is 360 sampling instants each main rotor rotation. A preliminary analysis enhanced that the frequency band of interest for flight mechanics is well beyond 1500 Hz, then, in order to reduce the computational burden of the identification process, the original signals were resampled at 153.8 Hz (36 sampling instant each main rotor rotation), which correctly represents the signals dynamics.

Before starting the identification process, data consistency for all the performed flight tests was verified through a compatibility check on the flight measurements based on kinematics relations.

Measurement	*CoM acceleration*	*CoM velocity*	*Angular acceleration*	*Angular rates*	*Attitude*
Noise standard deviation	0.0492 ft/s^2	0.32808 ft/s	0.00025 rad/s^2	0.0035 rad/s	0.00035 rad

**Table 7.7 – Standard deviations of inertial measurement noises**

7.2.2 Flight Tests Design

Optimal flight test design can be performed for rotorcraft model identification, since stringent safety constraints on flight trajectory dictated for re-entry vehicle are not applicable in this case.

The classical excitation inputs can be used for rotorcraft identification, obviously they should be applied to the specific rotorcraft primary commands. A peculiar characteristic of rotorcraft is that they generally exhibit dynamically unstable response . As a consequence, the flight tests have to be completed with feedback by the pilot or with the automatic flight control system active (closed loop testing) to keep the response within a reasonable range of amplitude. For example, while test is going on using on-axis control input, pilot can regulate off-axis controls to keep aircraft near the flight condition test point. However this strategy must not mask or suppress important aspects of the relevant dynamic, introducing collinearity into the flight data, otherwise flight data information will be poor.

Several flight tests were performed in simulation for the identification of the UH60 rotorcraft model. For each of them, flight data were gathered over a time range of 15s. Two flight test conditions were considered, that is, hover at 90 ft altitude above ground level and forward flight condition at 60 knots. In each flight condition, several identification manoeuvres were carried

out, perturbing the starting trimmed condition. The first one was a 3-2-1-1 perturbation applied to one of the four rotorcraft controls, that is, longitudinal cyclic pitch, lateral cyclic pitch, main and tail rotor collective pitch; these manoeuvres were repeated for each control and used for model identification purpose. The second manoeuvre type was a doublet perturbation applied to one of the four rotorcraft controls; also these manoeuvres were repeated for each control and used for the validation of partial results after each step of the identification strategy, as described in the following. Finally, other two tests were executed and used for the final validation of the global identified model: collective sweep perturbation starting from hover; doublet perturbations applied in sequence to all the four rotorcraft control, starting from the forward flight condition. In total 18 manoeuvres were executed. For all the manoeuvre types, the amplitude of the perturbation was equal to 10% of the maximum control deflection, whereas the duration of the manoeuvre was 7s for the 3-2-1-1 command input, 2s for the single doublet, 6s for the sweep and 8s for the sequence of doublets. Due to the possible instability of the vehicle, identification test manoeuvres were performed while flight control system was active (closed loop test), degrading the optimality of the flight test. Indeed the commanded input was modified by the flight control system, as shown in Figure 7.19 for a specific identification manoeuvre. However the measurement of the actual control applied by the flight control system was recorded and system identification was performed relating these measurements (open loop inputs) with the vehicle's dynamics.
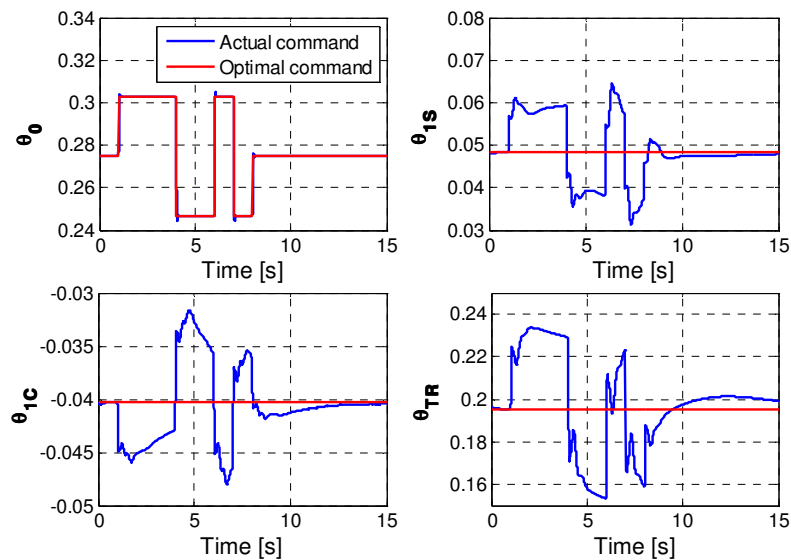
Figure 7.19 - Commanded identification test manoeuvres and actual commands for a 3-2-1-1 perturbation on the collective starting from trimmed forward flight at 60 knots

7.2.3 Model Identification Results

The model identification results for the rotorcraft test case are presented and discussed in this section [AR8]. The three-step methodology described in section 6.2 was applied.

7.2.3.1 First Identification Step Results

The main aim of this step is the estimation of the trajectories of external forces and moments acting on the fuselage of the vehicle. A by-product of this step is the estimation of filtered state vector of the vehicle dynamics.

First identification step was performed independently on each flight test. Only the 3-2-1-1 manoeuvres were used for identification purpose. Considering that the test should be repeated for each of the 4 commands (longitudinal cyclic, lateral cyclic, main rotor collective and tail rotor collective) and for each of the 2 examined flight conditions (hover and forward flight), in total 8 flight tests were analysed and 8 time histories were estimated for each force or moment components. For the sake of brevity, only the results of 2 tests are presented, that is, 3-2-1-1 longitudinal cyclic manoeuvre starting from trimmed hover and 3-2-1-1 lateral cyclic manoeuvre starting from trimmed forward flight. However analogous results were obtained for all the analysed flight tests.

Force and moment components provided by the UKF for the longitudinal perturbation of hover are presented from Figure 7.20 to Figure 7.25. In each figure the upper plot compares the estimated trajectory with the true one (known in simulation) and the lower plot shows the estimation error, which is compared with the 3σ uncertainty on the estimation, also provided by the UFK. True and estimated time histories are in practice undistinguishable, confirming that the estimation results are excellent. Estimation error is zero mean noise, confirming the estimation doesn't include any erroneous trend. Moreover the estimation error uncertainty is always consistent with the actual estimation error. It means that the stochastic characterisation of the estimation error provided by the filter is very reliable, too.
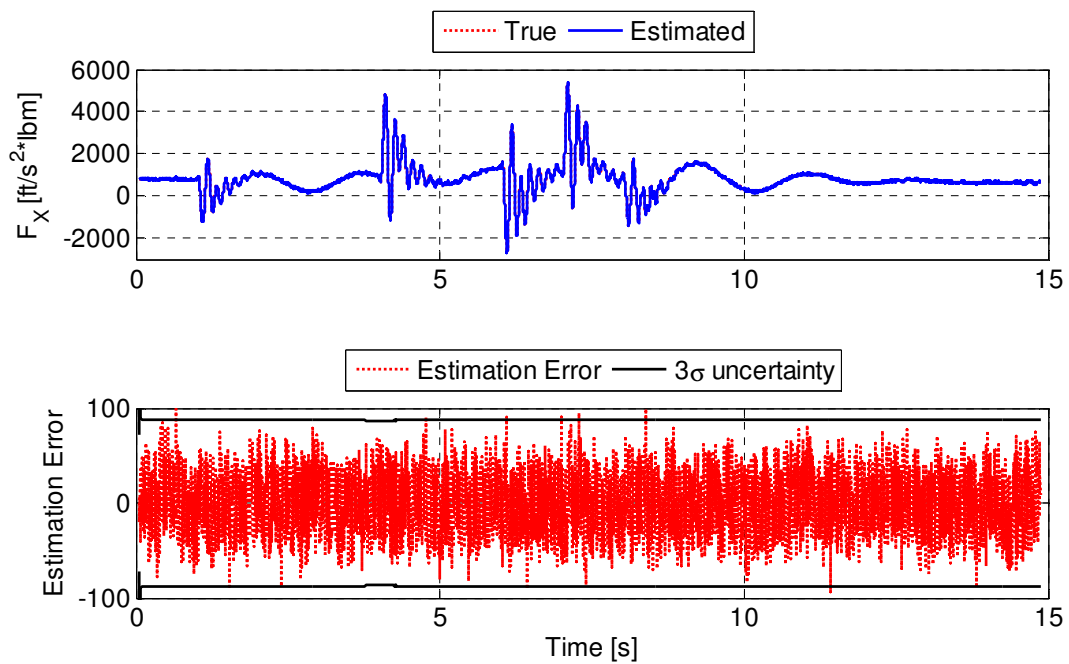
Figure 7.20 - Comparison between true and estimated F_X for longitudinal cyclic perturbation of hover condition
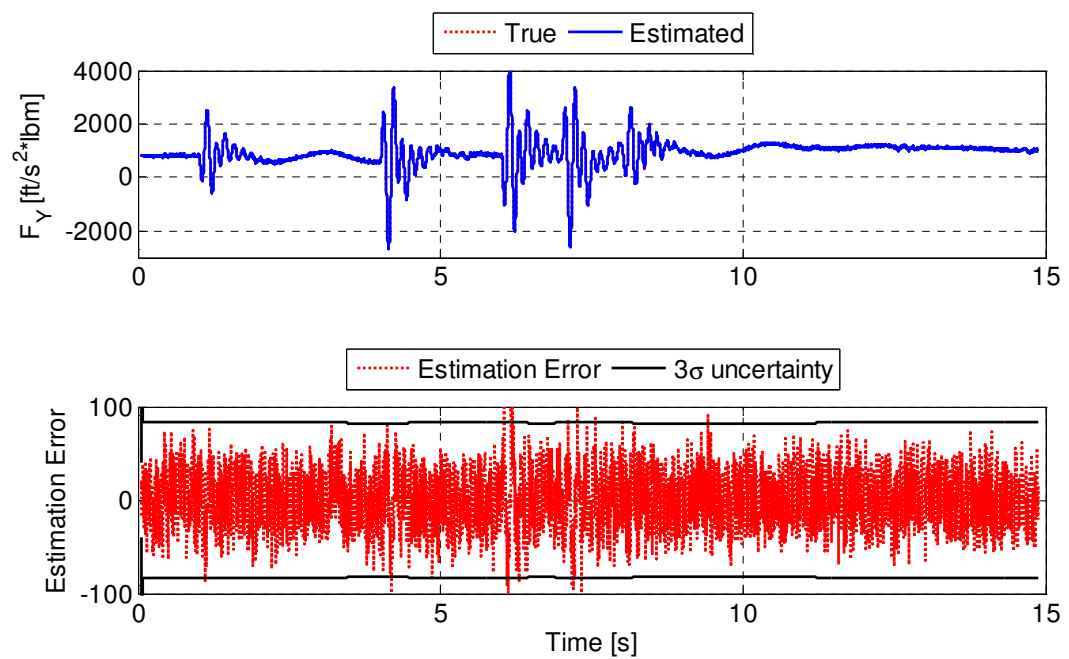
Figure 7.21 - Comparison between true and estimated F_Y for longitudinal cyclic perturbation of hover condition
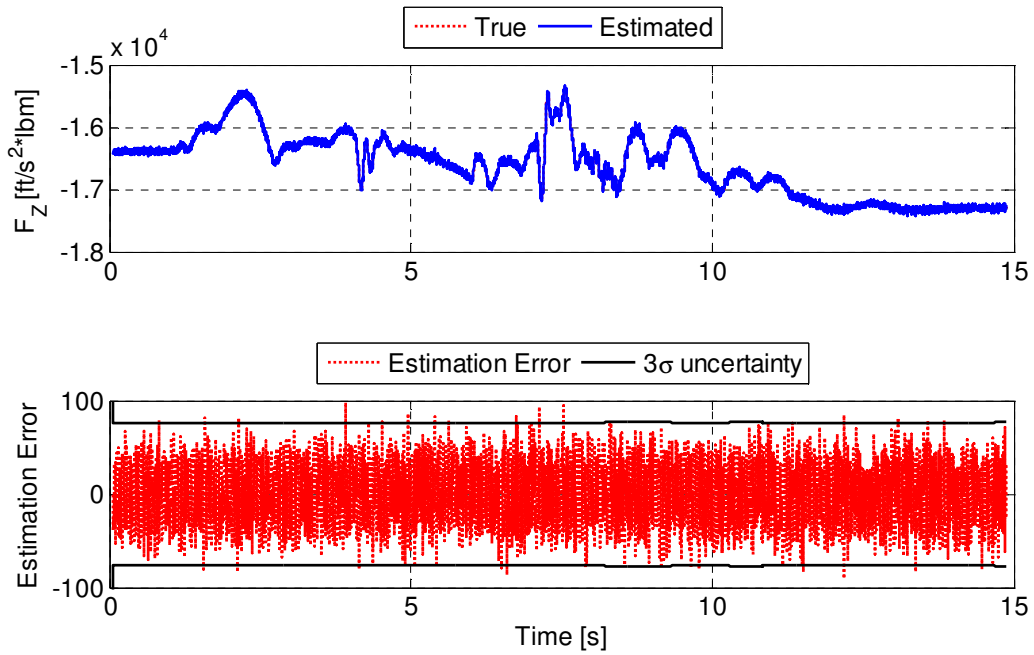
Figure 7.22 - Comparison between true and estimated F_Z for longitudinal cyclic perturbation of hover condition
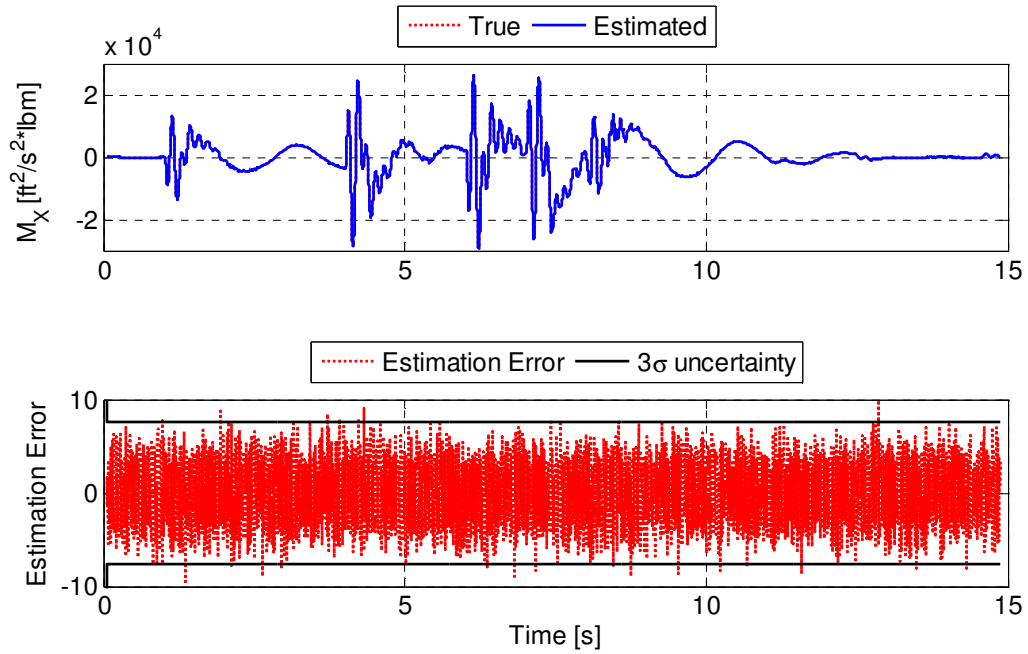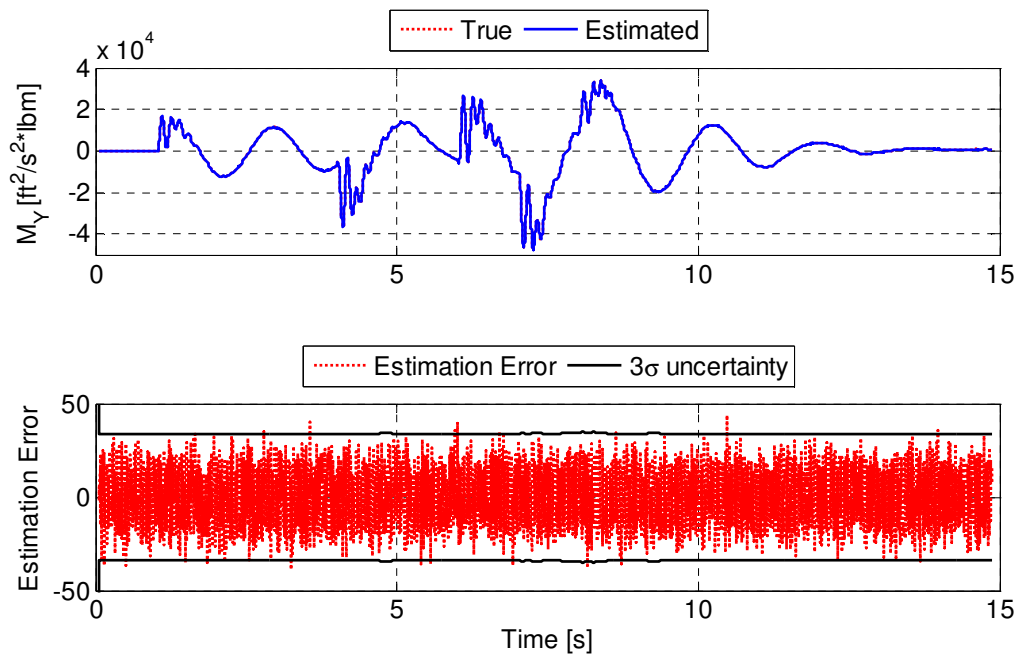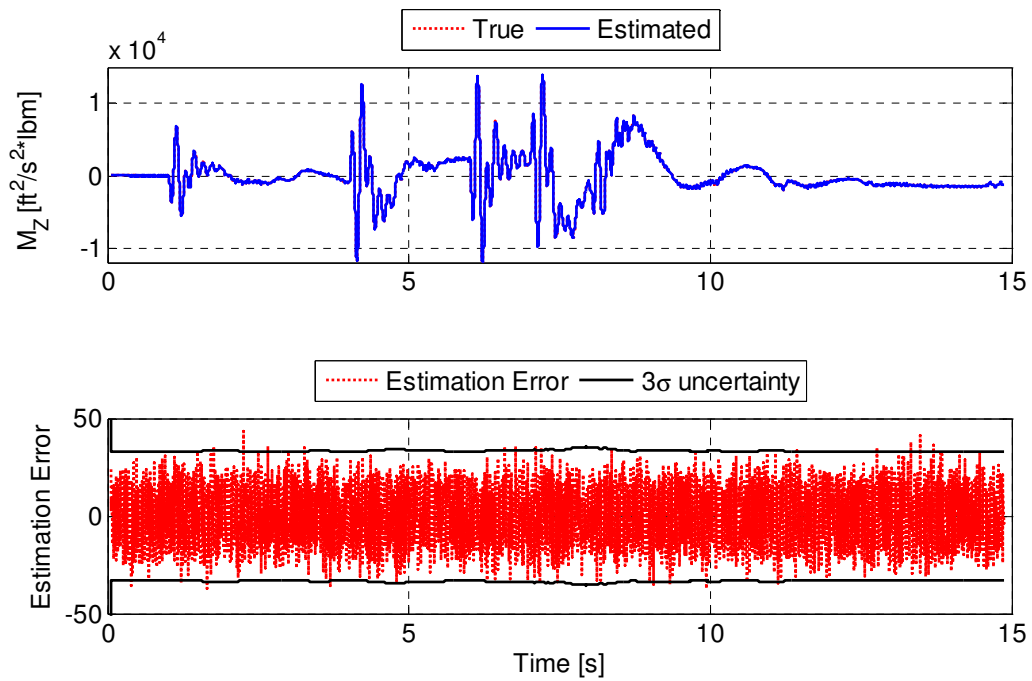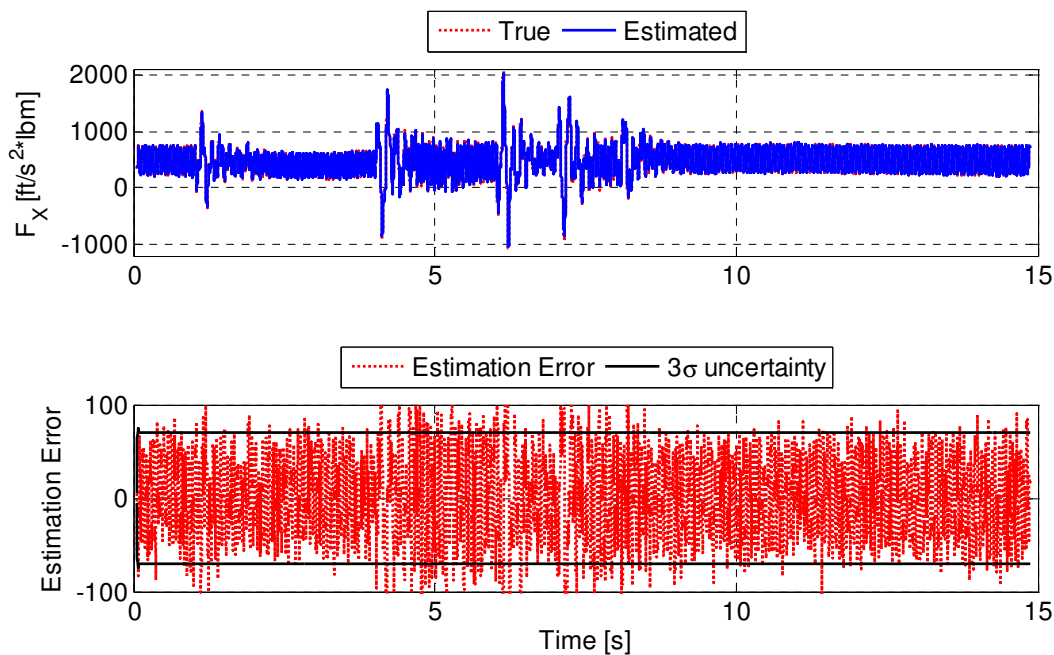

Figure 7.23 - Comparison between true and estimated M_X for longitudinal cyclic perturbation of hover condition

Figure 7.24 - Comparison between true and estimated M_Y for longitudinal cyclic perturbation of hover condition

Figure 7.25 - Comparison between true and estimated M_Z for longitudinal cyclic perturbation of hover condition

Concerning lateral perturbation of forward flight condition, results are presented from Figure 7.26 to Figure 7.31. The above considerations related to the hover identification results still hold. Moreover, in the forward flight condition force and moment components oscillate at 4 times the main rotor frequency, because the main rotor is four bladed. The oscillations are correctly caught by the UKF, as enhanced in Figure 7.32, where a zoom of Figure 7.26 is presented. These oscillations are not relevant in hover condition.

Another product of the UKF is the estimation of fuselage state vector, that is, position, velocity, attitude and angular rate of the fuselage. Figure 7.33 to Figure 7.35 show the results for angular rate components estimation from flight data of the 3-2-1-1 lateral cyclic manoeuvre perturbing forward flight condition. The figures enhance that the UKF estimations are in practice overlapped to the true time histories. Moreover the estimation uncertainty is lower than measurement uncertainty (lower plot of the figures) and the estimation error is consistent with the UKF estimated uncertainty. Similar results are obtained for all the flight measurements and all the examined flight tests.

Figure 7.26 - Comparison between true and estimated F_X for lateral cyclic perturbation of forward flight condition
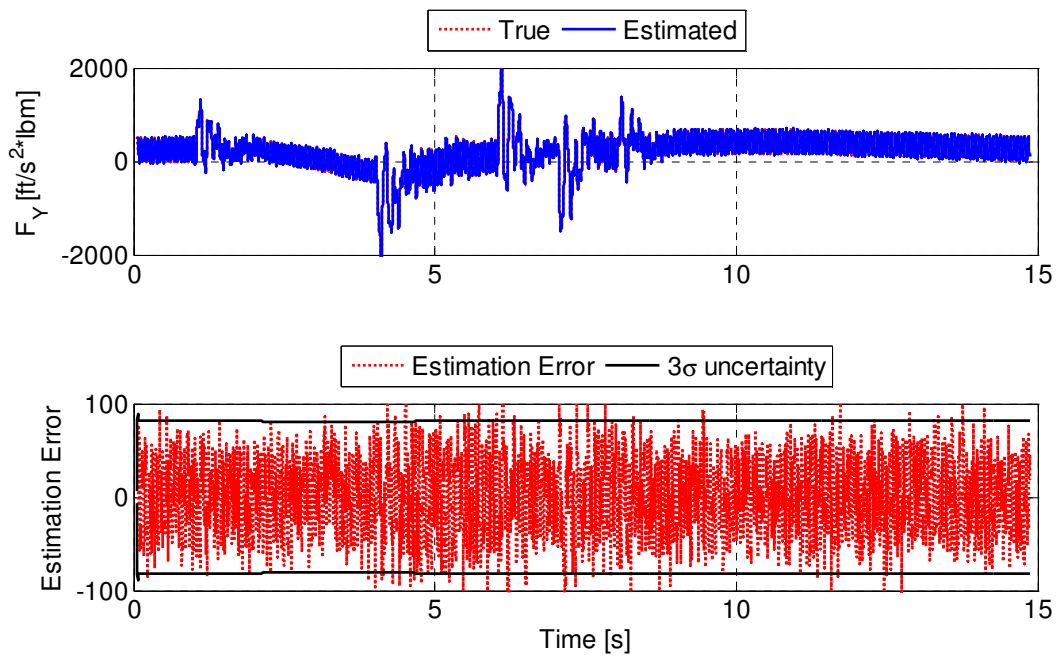
Figure 7.27 - Comparison between true and estimated F_Y for lateral cyclic perturbation of forward flight condition
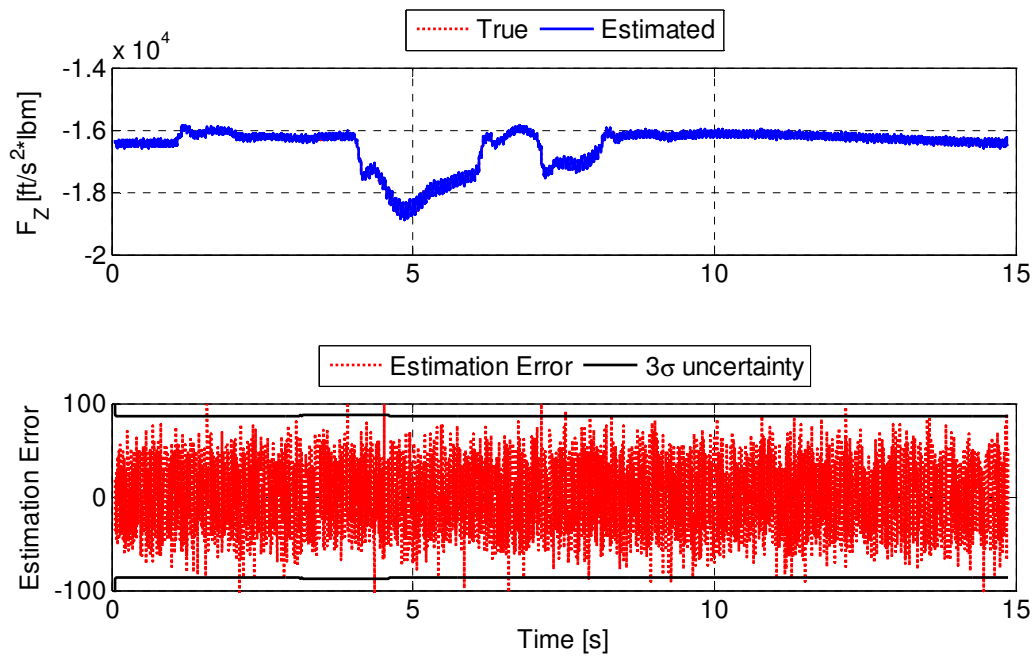

Figure 7.28 - Comparison between true and estimated F_Z for lateral cyclic perturbation of forward flight condition
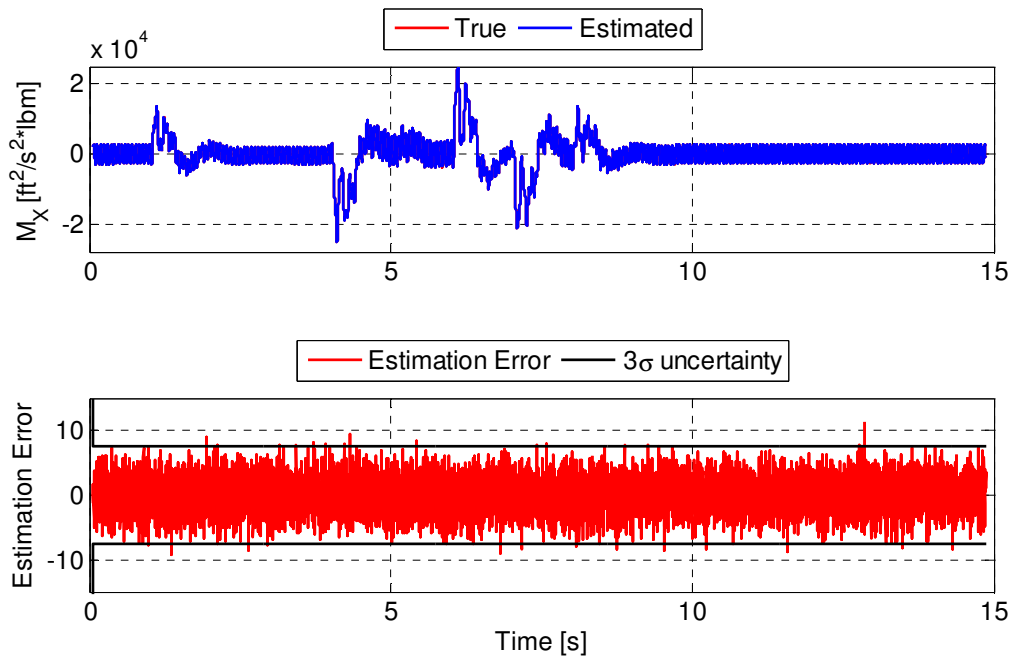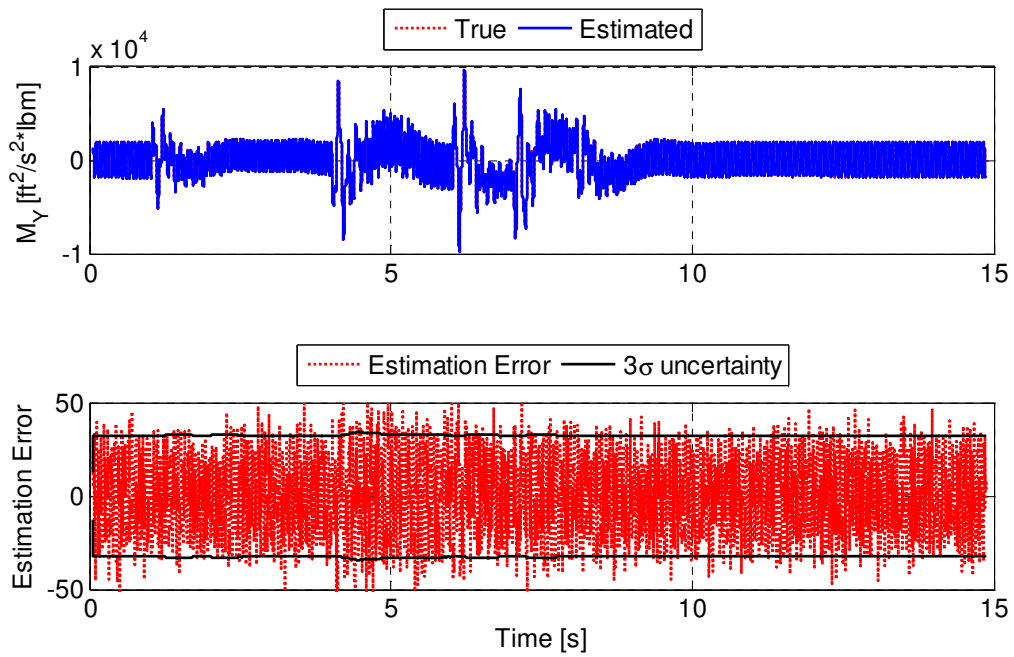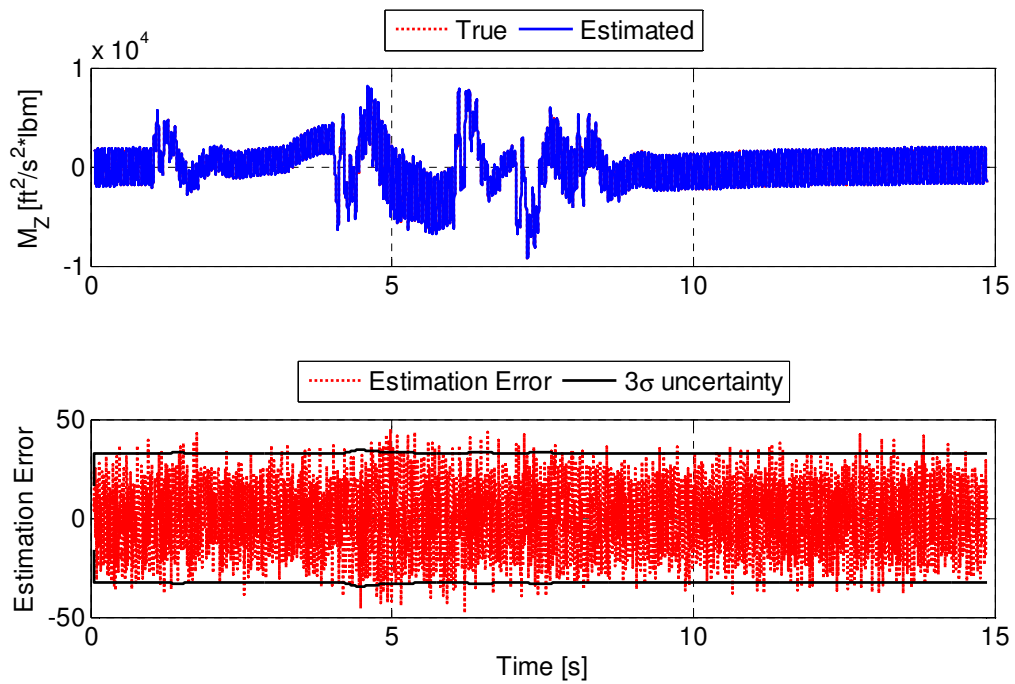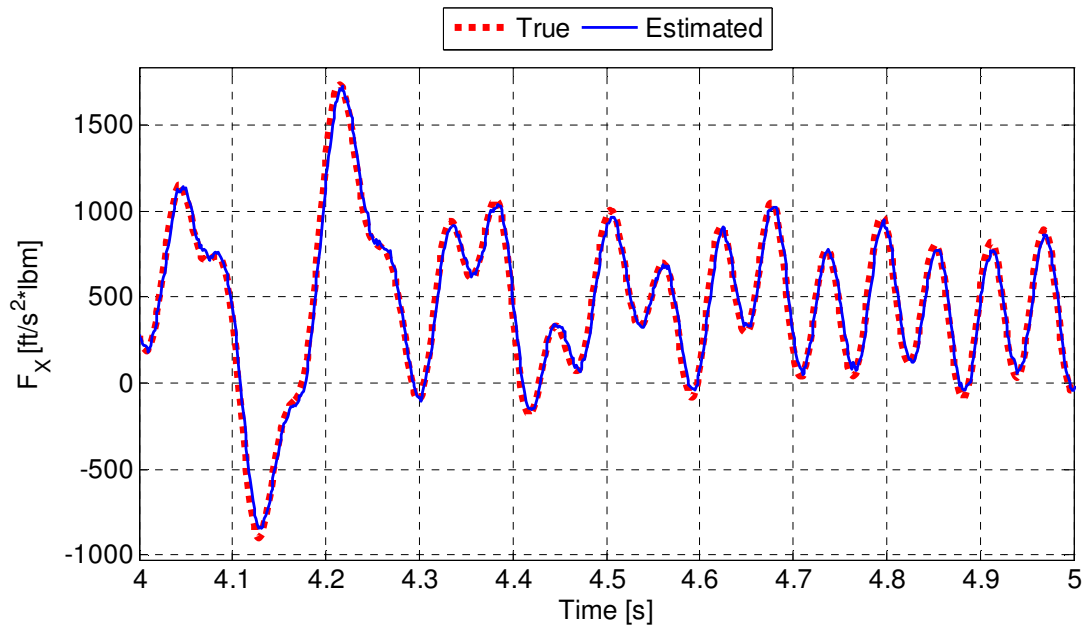
Figure 7.29 - Comparison between true and estimated M$_X$ for lateral cyclic perturbation of forward flight condition

Figure 7.30 - Comparison between true and estimated M$_Y$ for lateral cyclic perturbation of forward flight condition

Figure 7.31 - Comparison between true and estimated M$_Z$ for lateral cyclic perturbation of forward flight condition

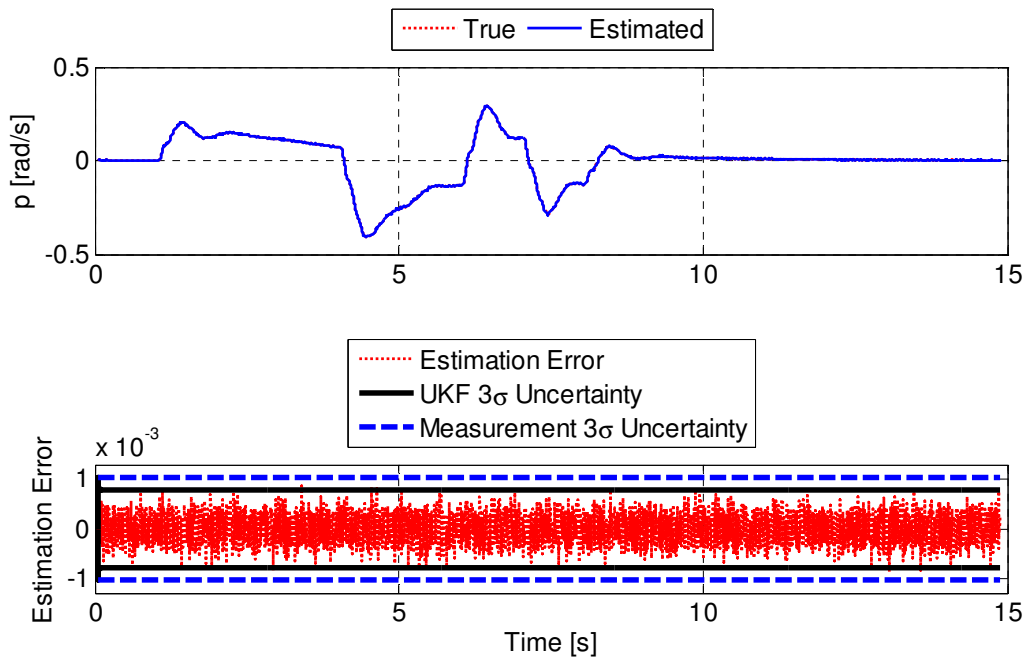**Figure 7.32 - Zoom of Figure 7.26: the UKF catches the high frequency oscillations**

Figure 7.33 - Comparison between true and estimated X-axis component of angular rate for lateral cyclic perturbation of forward flight condition
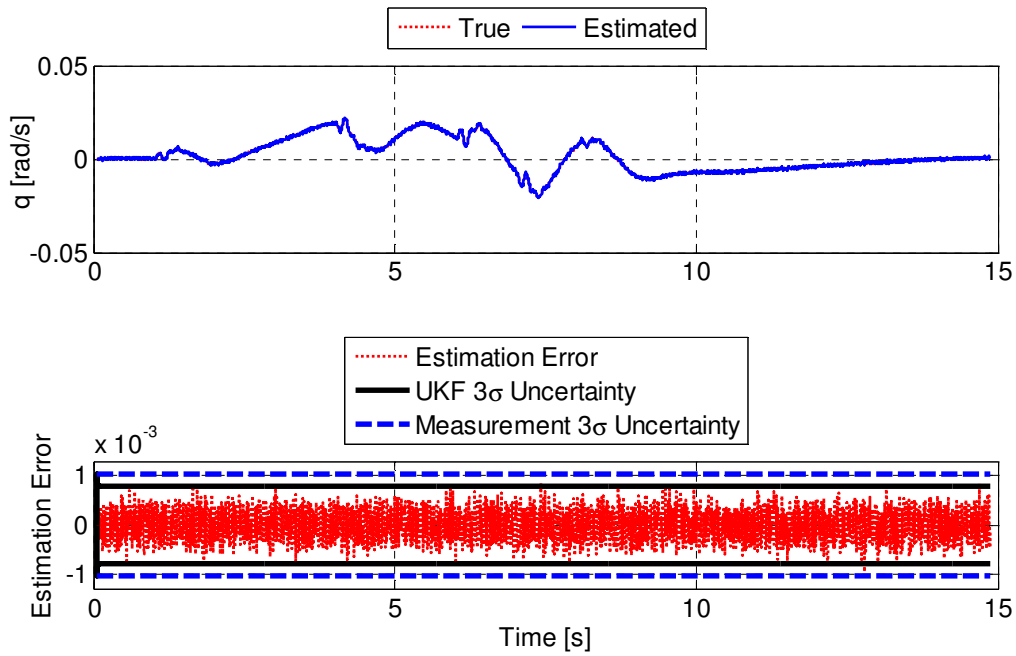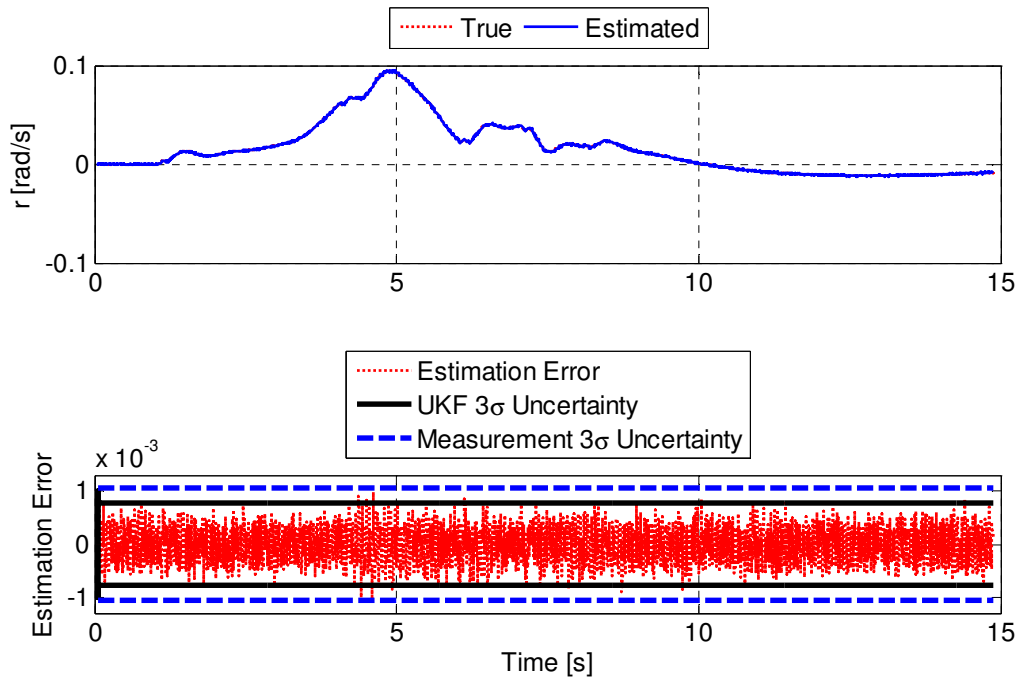

Figure 7.34 - Comparison between true and estimated Y-axis component of angular rate for lateral cyclic perturbation of forward flight condition

Figure 7.35 - Comparison between true and estimated Z-axis component of angular rate for lateral cyclic perturbation of forward flight condition

7.2.3.2 Second Identification Step Results

The model of each rotor dynamic, that is, coning, longitudinal flapping and lateral flapping as described by Eq. 110 to Eq. 112, was identified independently. The data gathered during all the 3-2-1-1 simulated flight tests were provided as input to the estimation process. The estimation was executed in the frequency range [0, 20] Hz. Since the structure of the identified model was completely different from the one of the model used for simulated flight data generation, the true values of the estimated parameters were not available. Therefore, obtained results were checked comparing the true time histories of the rotor states with the ones provided by the identified model through a dynamic simulation, as presented in the following figures. The comparison is performed both on the 3-2-1-1 manoeuvres used for identification and on the doublet manoeuvres, which were not used for the identification (acid test). Only the last test results are shown, because they are more significant.

The acid tests for coning dynamic model in hover and forward flight conditions are presented in Figure 7.36 and Figure 7.37, respectively. The coning is essentially excited when main rotor collective perturbation is applied, whereas in forward flight less relevant dynamics appear when longitudinal cyclic perturbation is introduced, probably due to the action of the flight control

system. Generally, the model is able to reproduce the measured coning dynamics along all the examined manoeuvres and for both the flight conditions, except for the spikes which follow a step command. This problem may be due to the structure of the model used which could be further optimized.

The acid tests for longitudinal flapping dynamic model in hover and forward flight conditions are shown in Figure 7.38 and Figure 7.39, respectively. The model works very well in all the performed tests.

The acid tests for lateral flapping dynamic model in hover and forward flight conditions are presented in Figure 7.40 and Figure 7.41, respectively. Again the model works very well in all the performed validation tests. It is worthy to note that in forward flight the flap angles oscillate at a frequency equal to 4 times the main rotor frequency. The model is able to catch this dynamic as enhanced in Figure 7.42 where a zoom of Figure 7.41 is shown. Similar results are obtained for the coning and longitudinal flapping models, too.
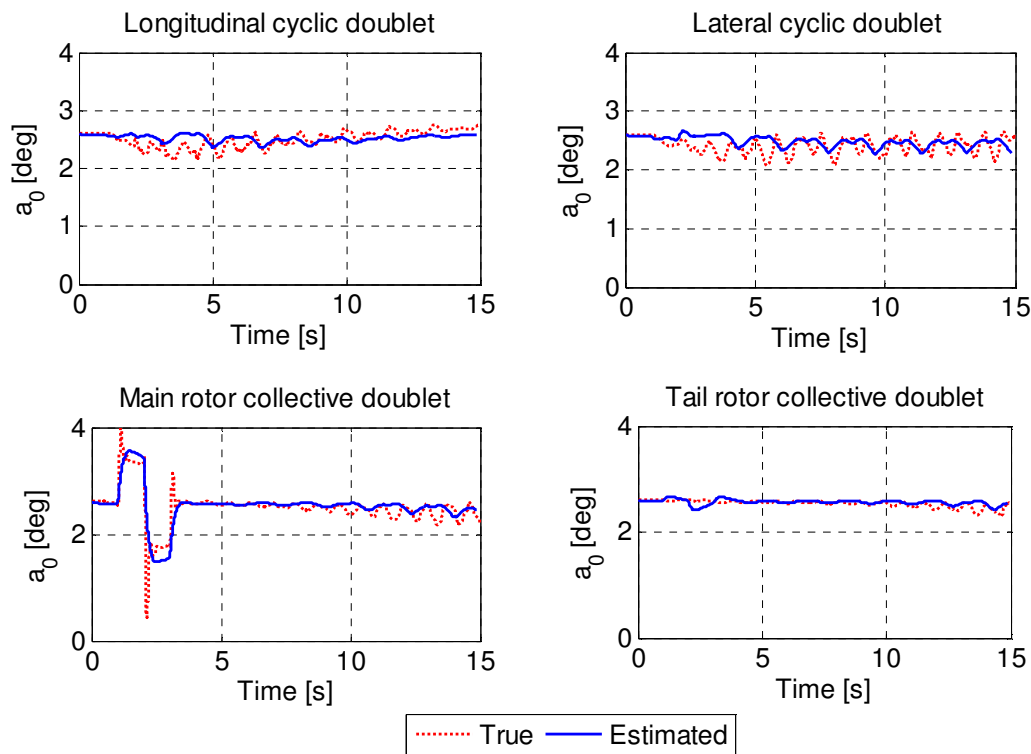
Figure 7.36 - Comparison between true coning angle and the ones provided by the identified model in hover condition along four manoeuvres which were not used for the identification
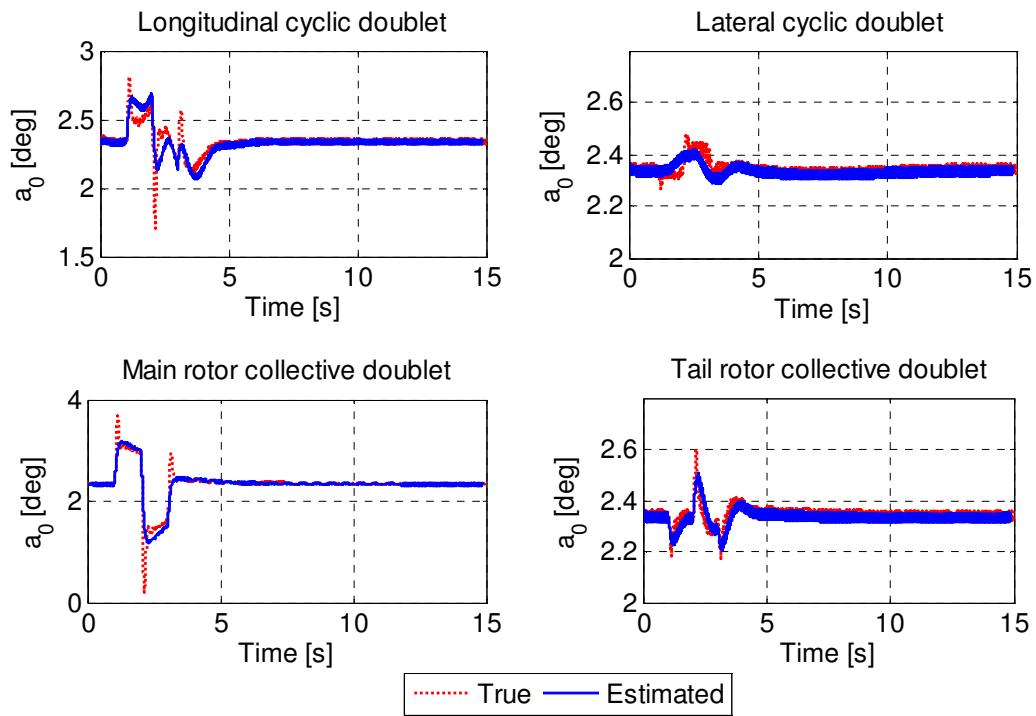
Figure 7.37 - Comparison between true coning angle and the ones provided by the identified model in forward flight along four manoeuvres which were not used for the identification
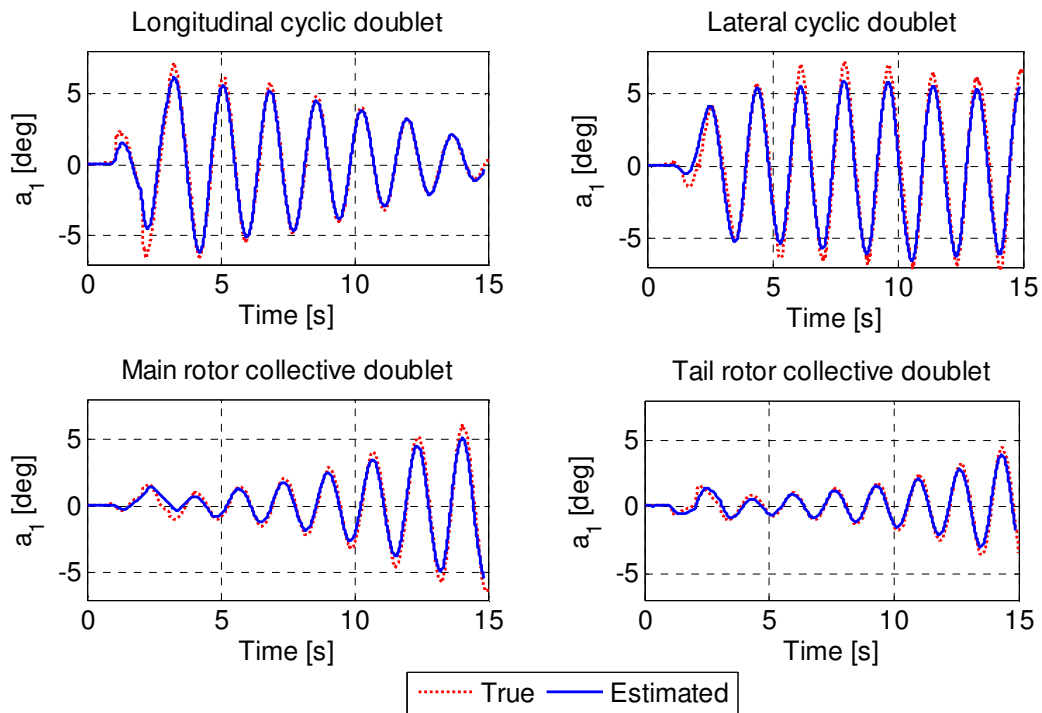
Figure 7.38 - Comparison between true longitudinal flap angle and the ones provided by the identified model in hover condition along four manoeuvres which were not used for the identification
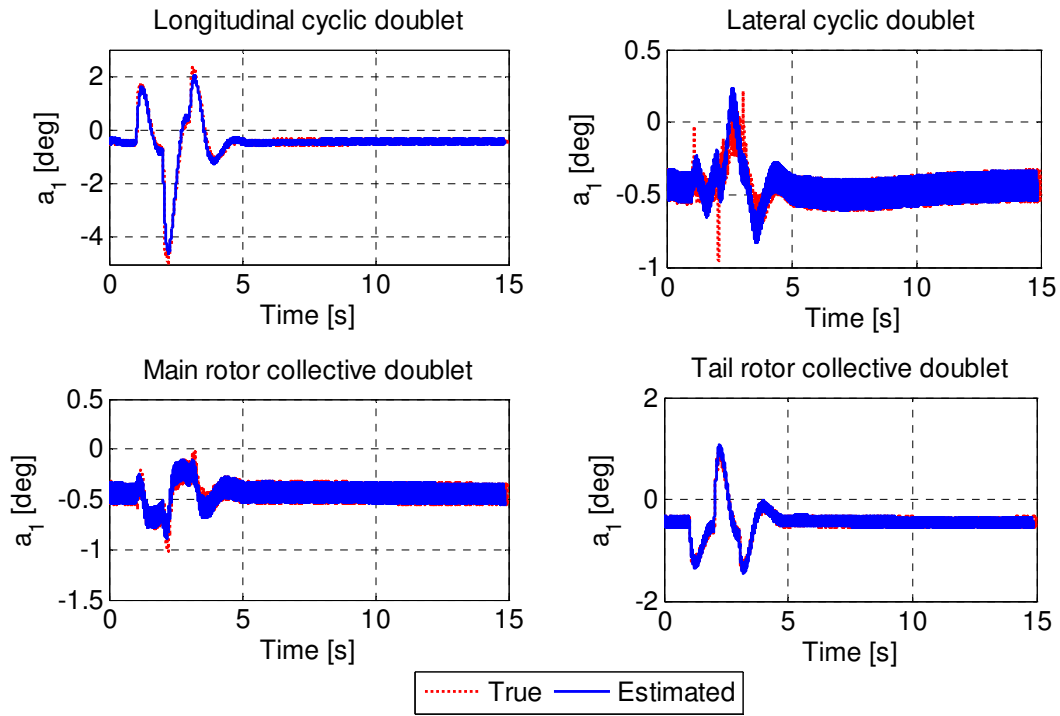
Figure 7.39 - Comparison between true longitudinal flap angle and the ones provided by the identified model in forward flight along four manoeuvres which were not used for the identification
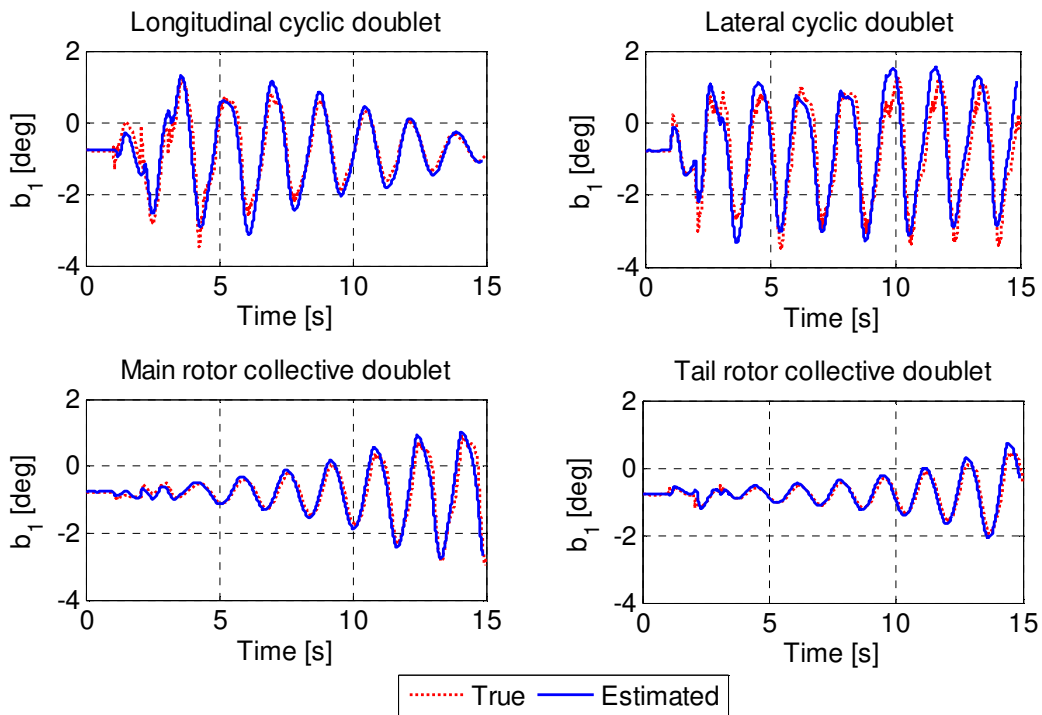
Figure 7.40 - Comparison between true lateral flap angle and the ones provided by the identified model in hover condition along four manoeuvres which were not used for the identification
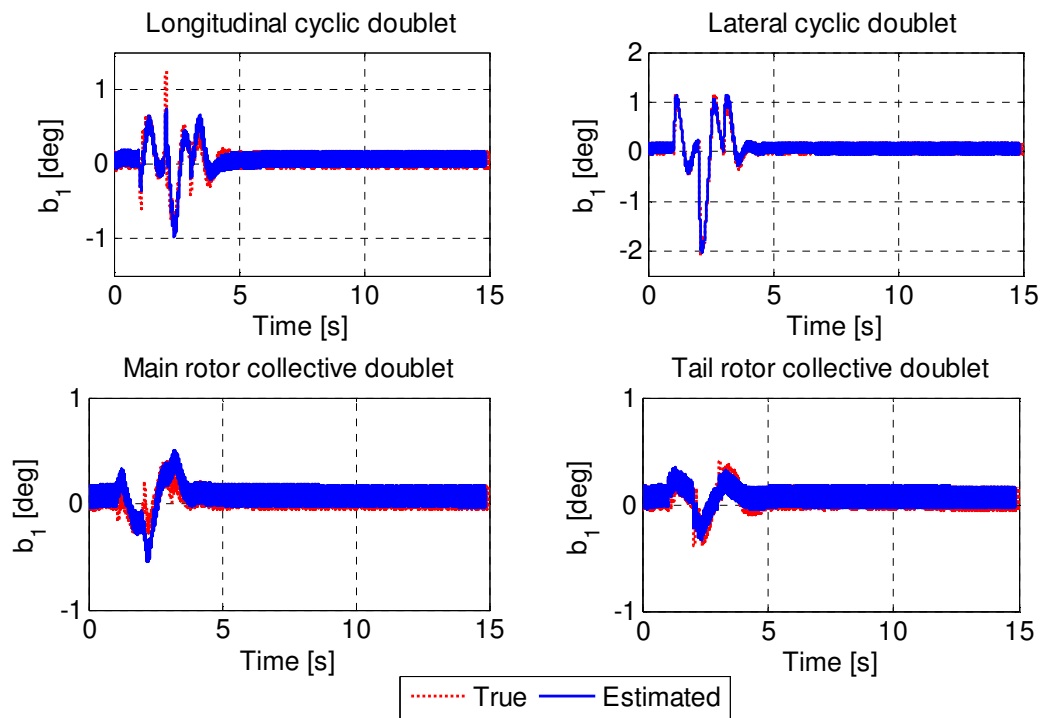
Figure 7.41 - Comparison between true lateral flap angle and the ones provided by the identified model in forward flight along four manoeuvres which were not used for the identification
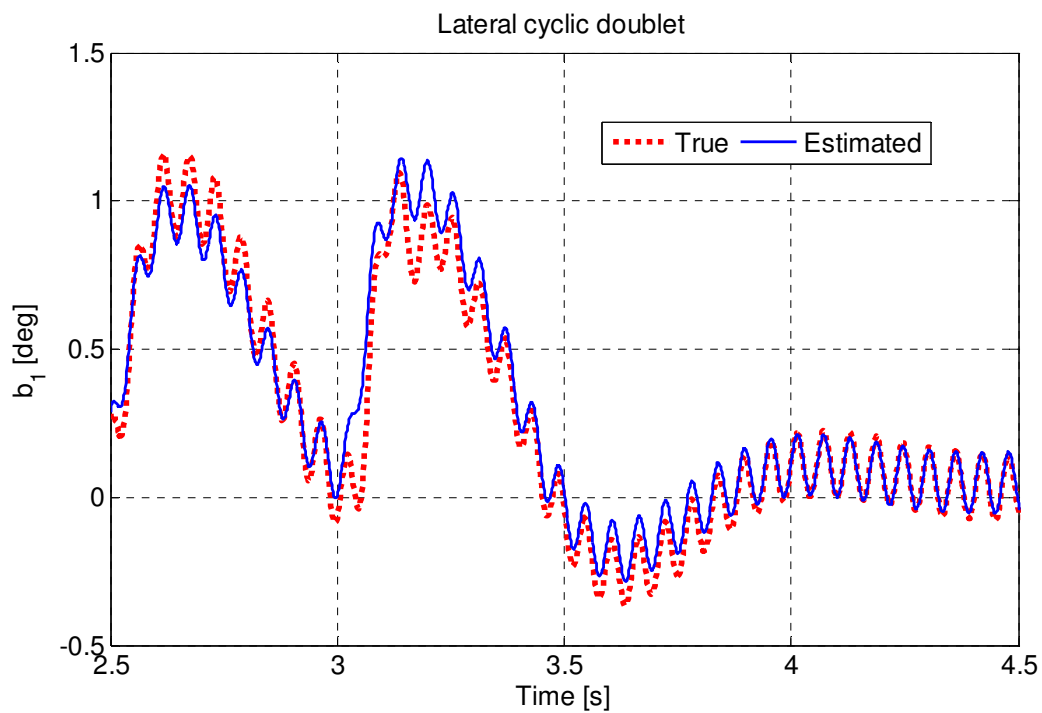

Figure 7.42 - Zoom of Figure 7.41: the lateral flapping model catches the high frequency oscillations

7.2.3.3 Third Identification Step Results

In order to estimate the unknown parameters of the force model, the data of all the 3-2-1-1 manoeuvres were concatenated and provided as input to the identification process as one single test. Also in this case, since the structure of the identified model was completely different from the one used for flight data generation, the true values of the estimated parameters were not available. Therefore the quality of the estimation was evaluated through the comparison of the true force and moment components time histories with the ones provided by the model. This comparison was executed both on the data of the 3-2-1-1 manoeuvres used for the identification and on the data of the doublet manoeuvres, which were not used for identification (acid test). Since the last test results are more significant, they are only shown for the sake of brevity.

Identification results for the hover conditions are presented from Figure 7.43 to Figure 7.48. Identification results for the forward flight are presented from Figure 7.49 to Figure 7.54. In both flight conditions, the estimation of F_Z and M_Y components are excellent. For the other components the identified model is able in mean to reproduce the true time histories but it doesn't catch some high amplitude oscillations at frequency of about 4 Hz, which are mainly present during the execution of the longitudinal cyclic manoeuvre. The current structure of the identified model does not allow a satisfactory capturing of the phenomenon. For what concern the F_X and F_Y components, a preliminary analysis shown that these oscillations are correlated to the main rotor single blade lead-lag angle, which oscillates at a frequency slightly greater than the main rotor one (about 4 Hz). The introduction of this variable into the model structure could solve the problem, but it requires the identification of the lead-lag dynamic model, increasing the complexity of the overall identification process. However, these oscillations are filtered out by the fuselage dynamics, therefore their effect on the vehicle dynamics is negligible.

On the other side, the model is able to match the oscillations in forward flight at about 16 Hz (4 times the main rotor frequency). They are due to the periodic behaviour of the four bladed main rotor, which is taken into account considering the 4/rev force and moment components associated with the rotor angular position. The described oscillation phenomena are enhanced in Figure 7.55, which is a zoom of Figure 7.49. The figure shows the high amplitude oscillations, which are not fitted by the model in the first 0.5 seconds of the plot, and the high frequency oscillation, fitted by the model in the following 1 second.
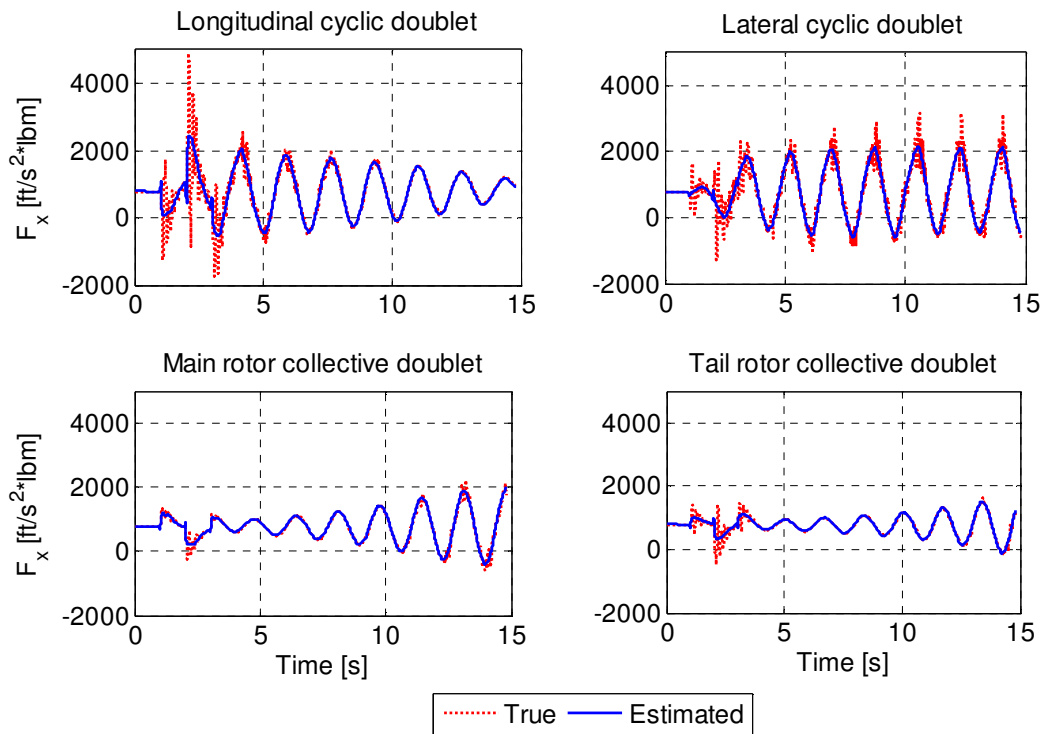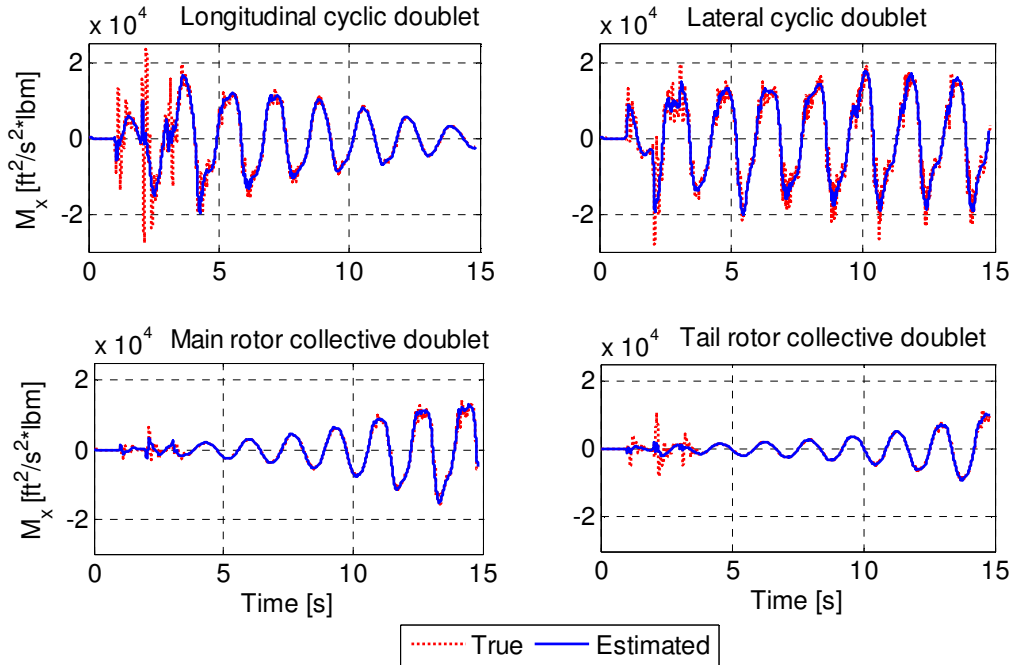
Figure 7.43 - F$_X$ component in hover: comparison between the true time histories and the ones provided by the model along four manoeuvres which were not used for the model identification (acid test)
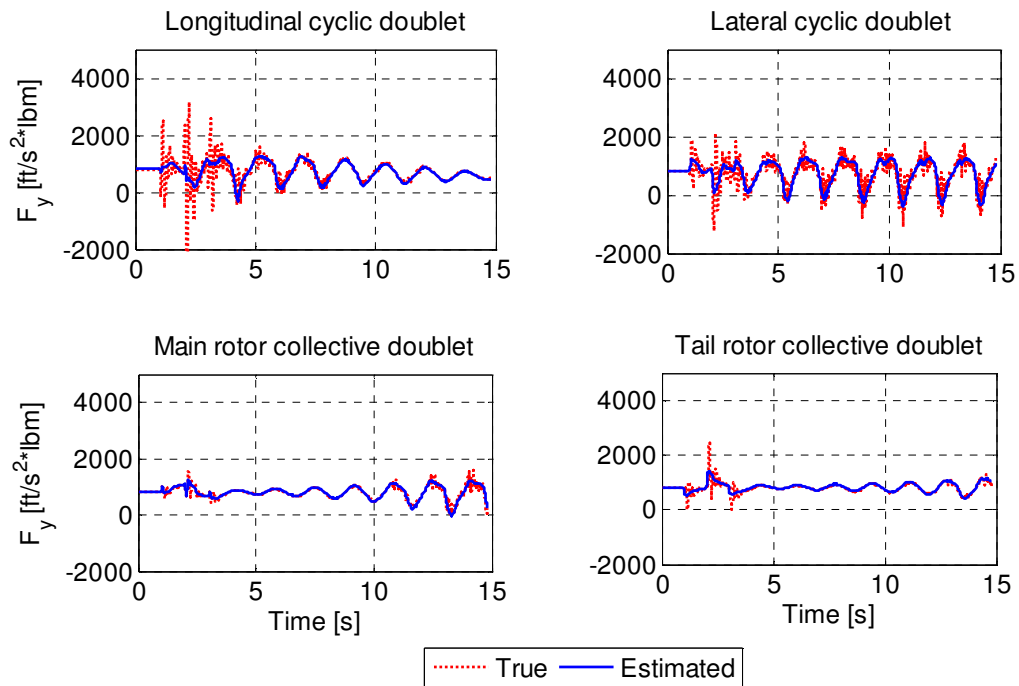
Figure 7.44 - F$_Y$ component in hover: comparison between the true time histories and the ones provided by the model along four manoeuvres which were not used for the model identification (acid test)
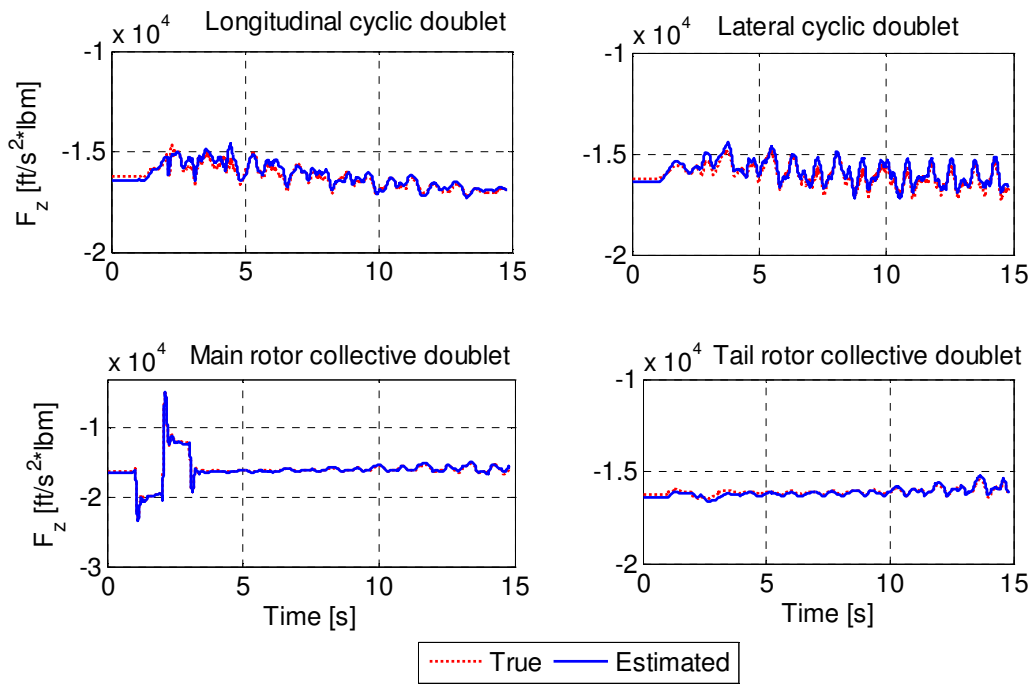
Figure 7.45 - F$_Z$ component in hover: comparison between the true time histories and the ones provided by the model along four manoeuvres which were not used for the model identification (acid test)

Figure 7.46 - M$_X$ component in hover: comparison between the true time histories and the ones provided by the model along four manoeuvres which were not used for the model identification (acid test)

Figure 7.47 - M_Y component in hover: comparison between the true time histories and the ones provided by the model along four manoeuvres which were not used for the model identification (acid test)

Figure 7.48 - M_Z component in hover: comparison between the true time histories and the ones provided by the model along four manoeuvres which were not used for the model identification (acid test)
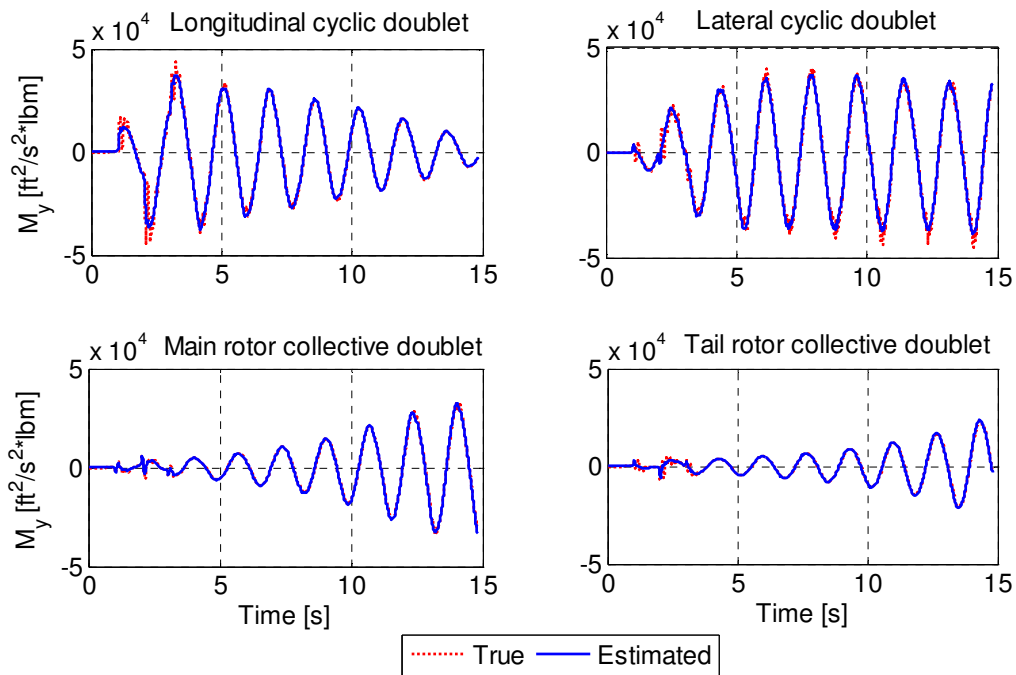
Figure 7.49 - F$_X$ component in forward flight: comparison between the true time histories and the ones provided by the model along four manoeuvres which were not used for the model identification (acid test)
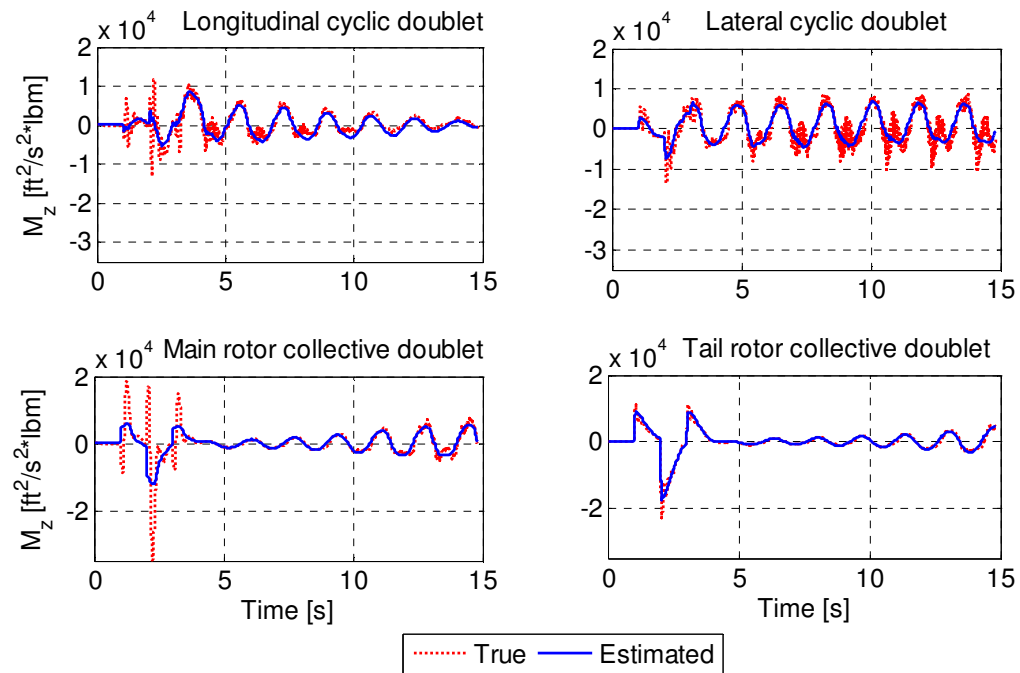

Figure 7.50 - F$_Y$ component in forward flight: comparison between the true time histories and the ones provided by the model along four manoeuvres which were not used for the model identification (acid test)
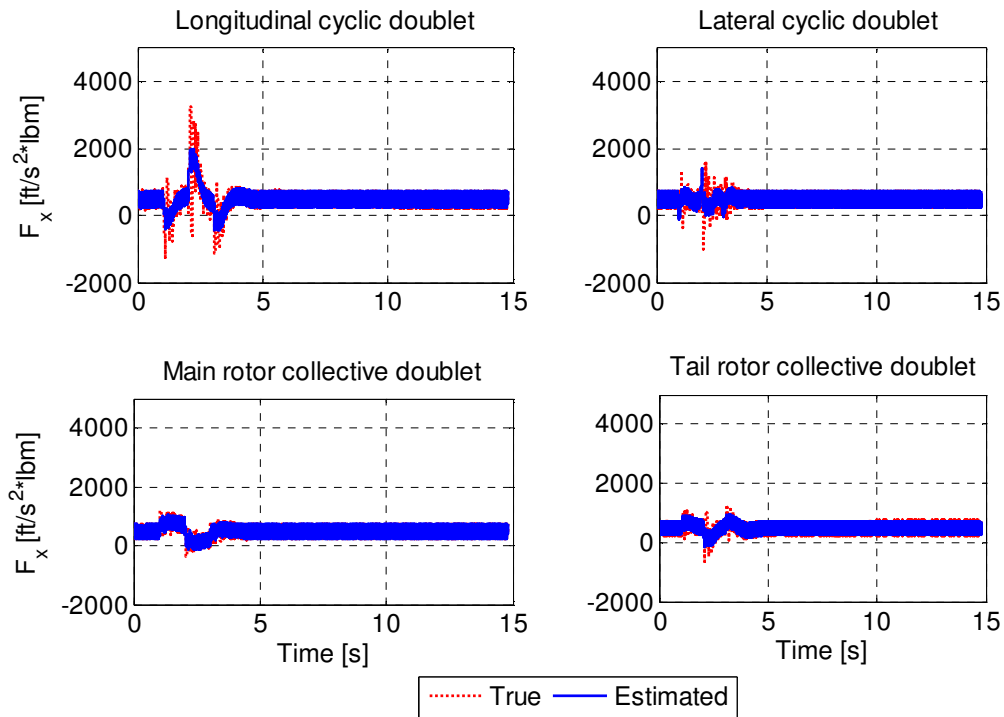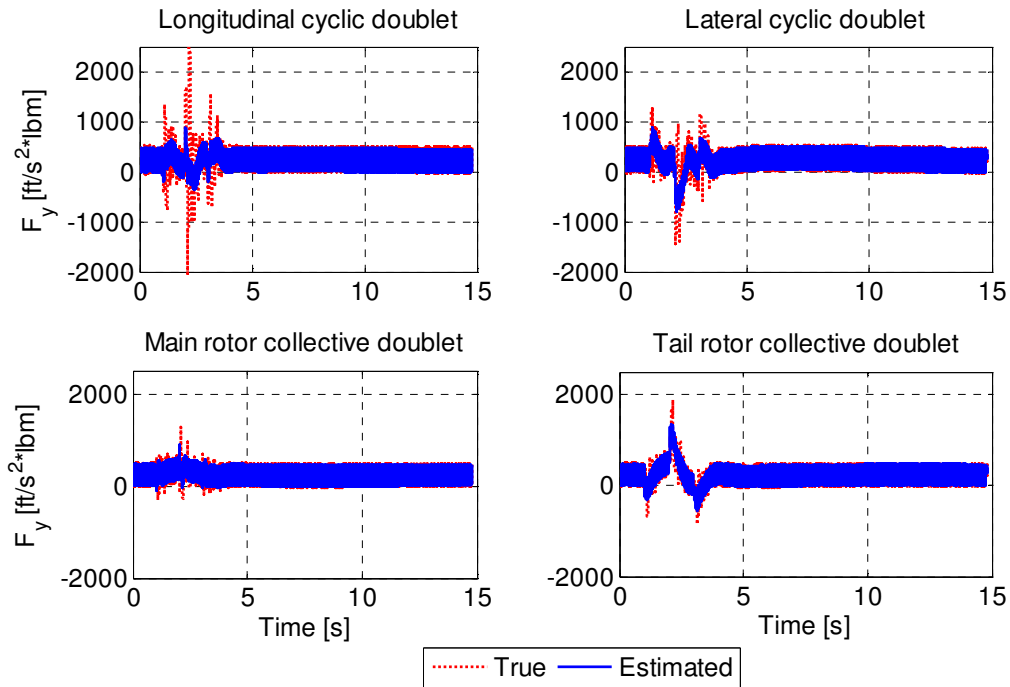
Figure 7.51 - F$_Z$ component in forward flight: comparison between the true time histories and the ones provided by the model along four manoeuvres which were not used for the model identification (acid test)
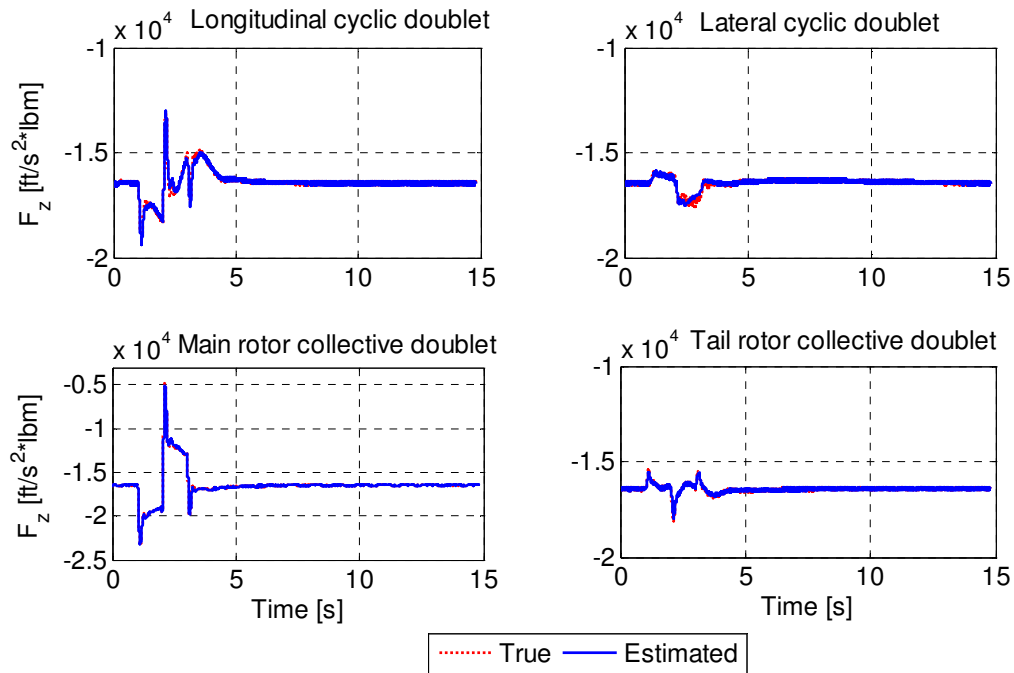

Figure 7.52 - M$_X$ component in forward flight: comparison between the true time histories and the ones provided by the model along four manoeuvres which were not used for the model identification (acid test)

Figure 7.53 - M_Y component in forward flight: comparison between the true time histories and the ones provided by the model along four manoeuvres which were not used for the model identification (acid test)
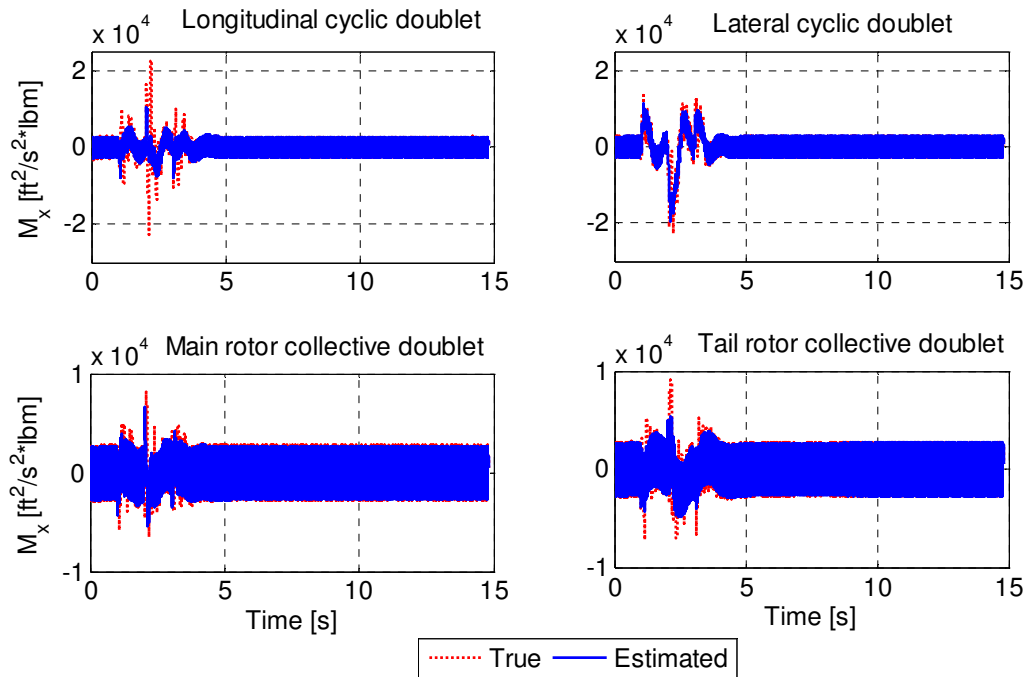

Figure 7.54 - M_Z component in forward flight: comparison between the true time histories and the ones provided by the model along four manoeuvres which were not used for the model identification (acid test)
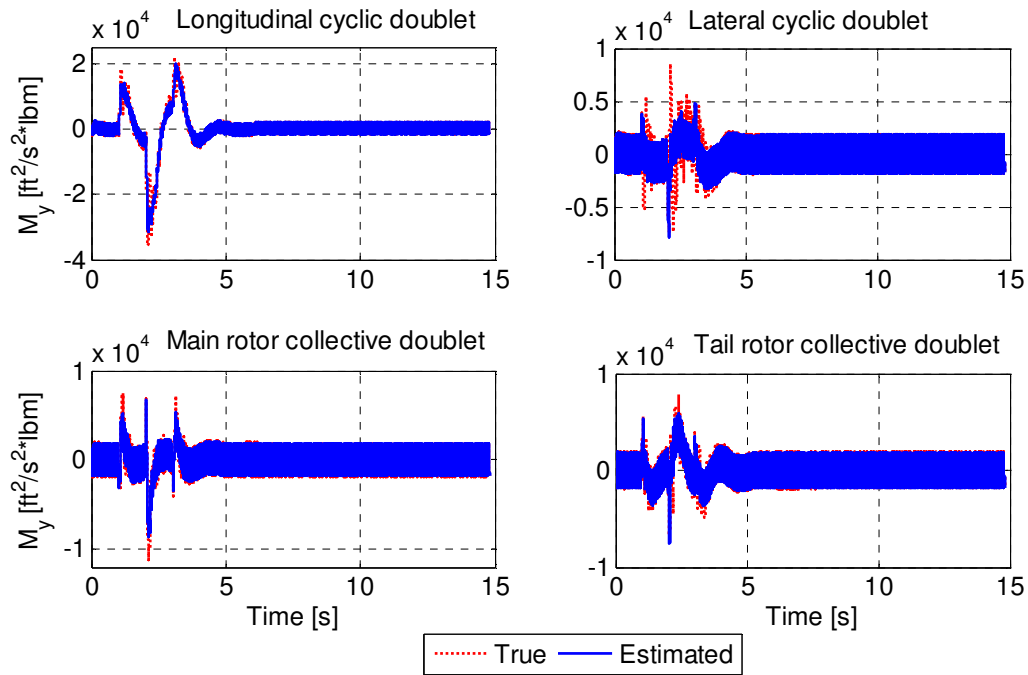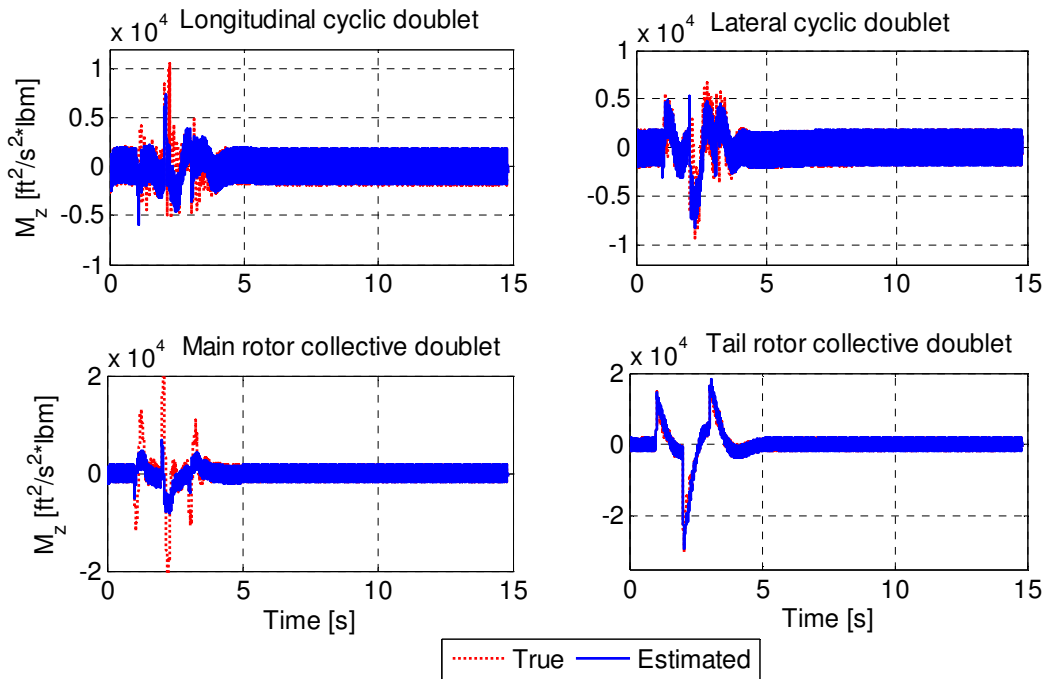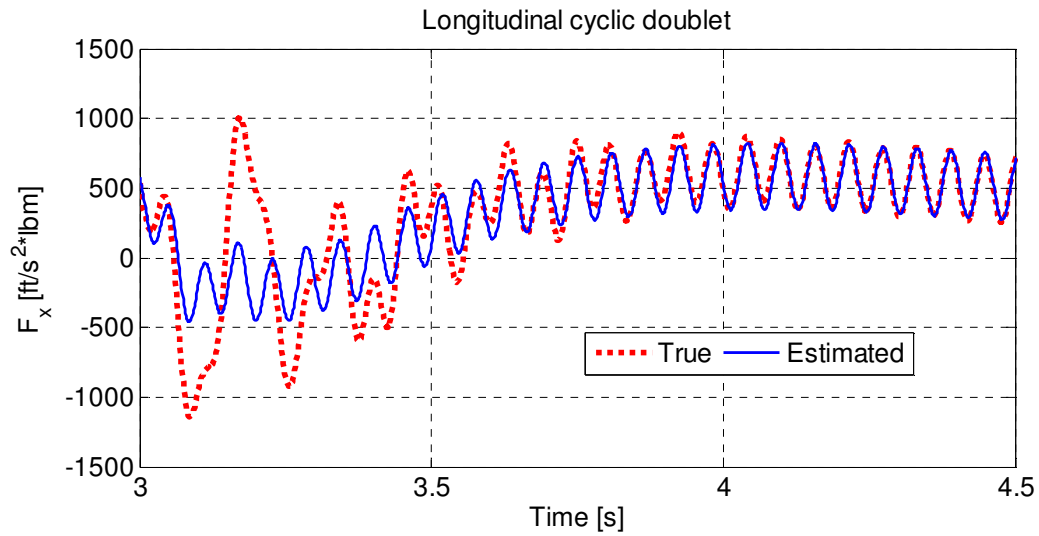
Figure 7.55 - Zoom of the first plot in Figure 7.49: the F_X model fits the high frequency oscillations but not the high amplitude low frequency ones

7.2.4 Model Validation

The complete simulation model of the rotorcraft was obtained by assembling the whole set of estimation results. It was implemented in MATLAB/SIMULINK environment, as shown in Figure 7.56
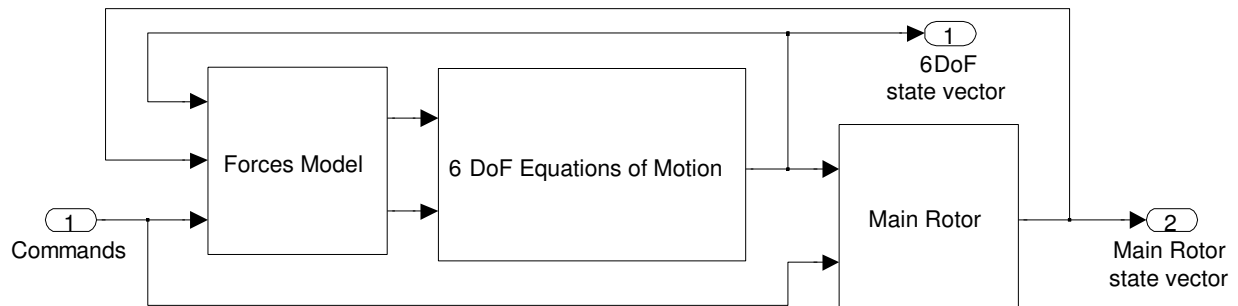
Figure 7.56 – First level block diagram of the identified rotorcraft model implemented in SIMULINK environment

The identified model was validated performing an open loop simulation and comparing the model outputs with the measurements. Consequently, the capability of the model to reproduce the measured flight data was evaluated. The validation was carried out through acid tests, therefore two manoeuvres that were not used for identification, neither for partial validation of single step results, were selected. The chosen tests consist of a frequency sweep in the range [0.05-2] Hz of the main rotor collective command, perturbing the trimmed hover condition (test

1), and a sequence of doublets applied to the four commands starting from trimmed forward flight at 60knots (test 2). When generating the simulated flight data in FLIGHTLAB, the flight control system was active and modifies the ideal test manoeuvres. The time histories of the actual vehicle commands, that are recorded and provided as input to the identified model, are presented in Figure 7.57 and Figure 7.61. Each simulation lasted 8 seconds and the simulation outputs were compared with the corresponding flight measurements provided by FLIGHTLAB. As already said, this type of validation is very critical because small identification errors could translate in dramatic differences in the simulation outputs till to the divergence, due to the absence of a flight control system which allows tracking the reference trajectory, that is, the measured one.

The acid test validation results are shown from Figure 7.58 to Figure 7.60 for test 1 and from Figure 7.62 to Figure 7.64 for test 2. The fitting of the flight data is good for the perturbed hover test and it is excellent for the forward flight condition, both for fuselage dynamics and rotor dynamics. The high amplitude force and moment oscillations described in the previous section, which the force model isn't able to reproduce, have negligible effect on the vehicle dynamics. Concerning main rotor coning, although the model generally works well, it is still not able to catch the spikes which follow the step command (see Figure 7.64).
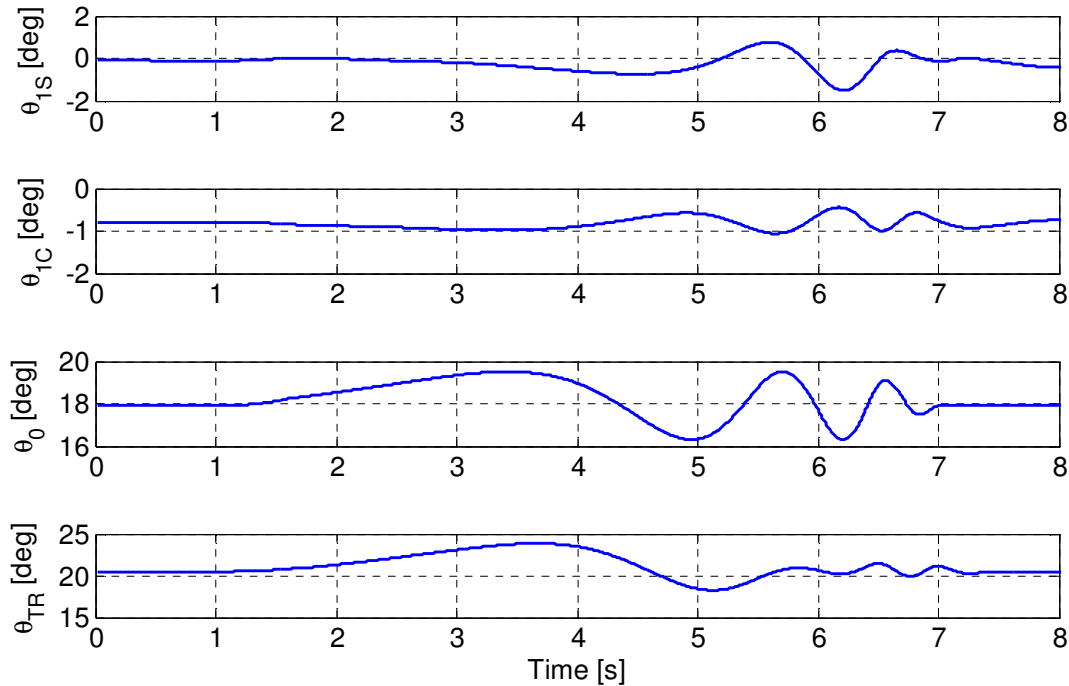
Figure 7.57 - Commands time histories (test 1)

Figure 7.58 - Comparison between the true time histories of the velocity and the corresponding time histories provided by the identified model (test 1)

Figure 7.59 - Comparison between the true time histories of the angular rate and the corresponding time histories provided by the identified model (test 1)

Figure 7.60 - Comparison between the true time histories of the rotor dynamics and the corresponding time histories provided by the identified model (test 1)

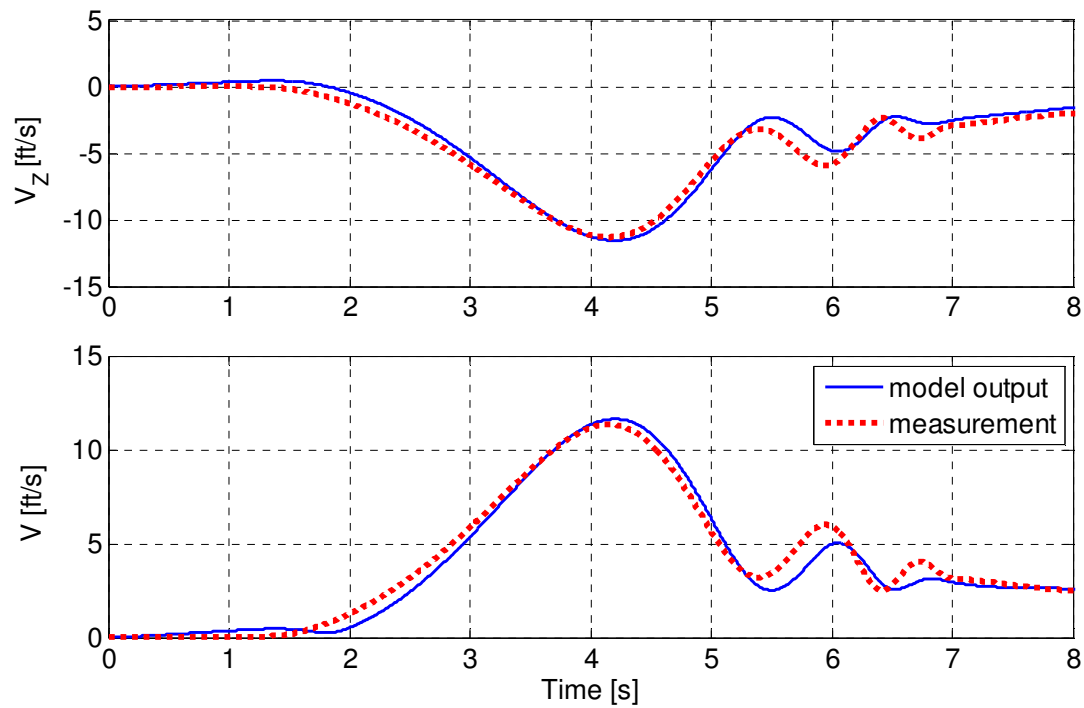**Figure 7.61 - Commands time histories (test 2)**

Figure 7.62 - Comparison between the true time histories of the velocity and the corresponding time histories provided by the identified model (test 2)
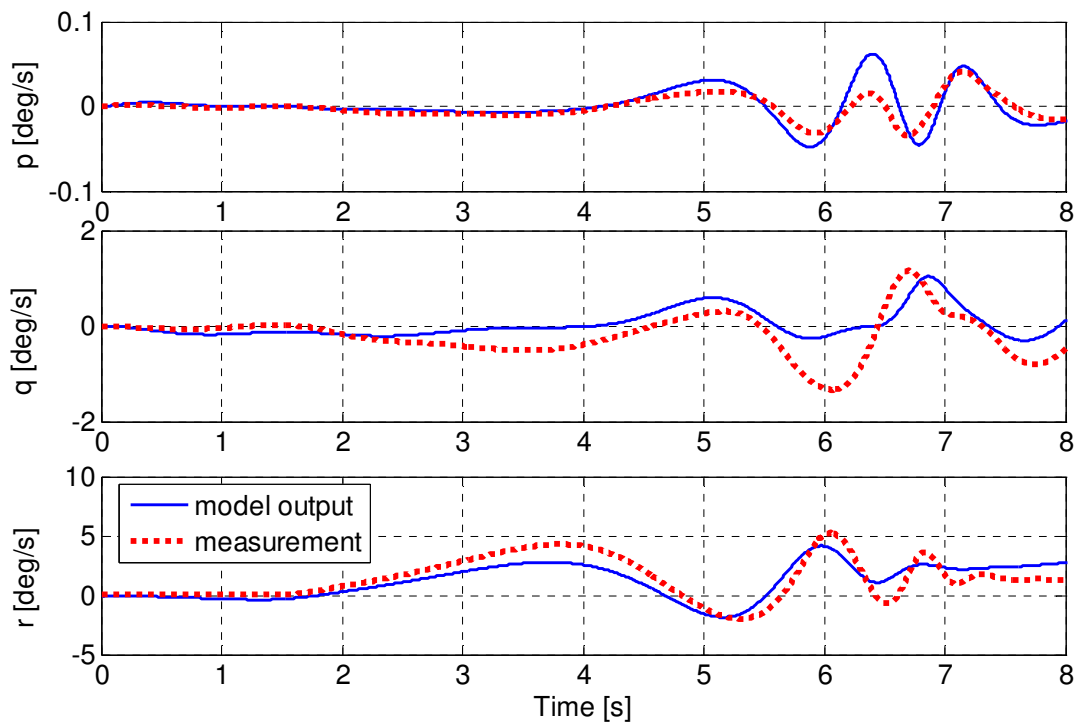

Figure 7.63 - Comparison between the true time histories of the angular rate and the corresponding time histories provided by the identified model (test 2)
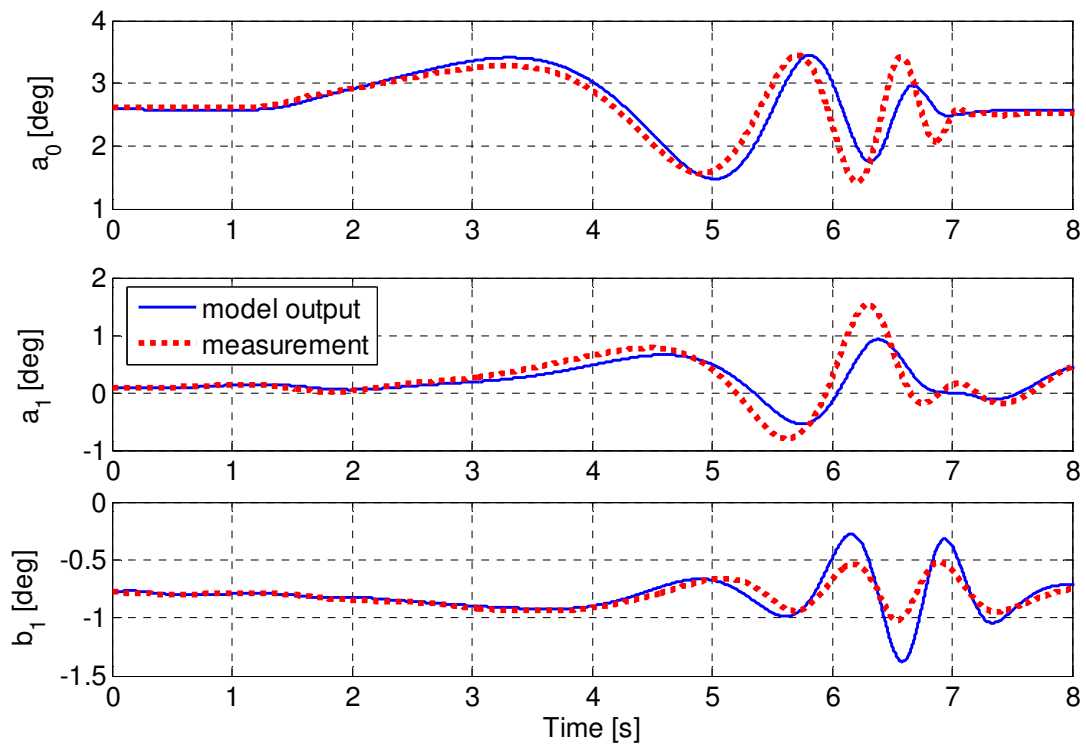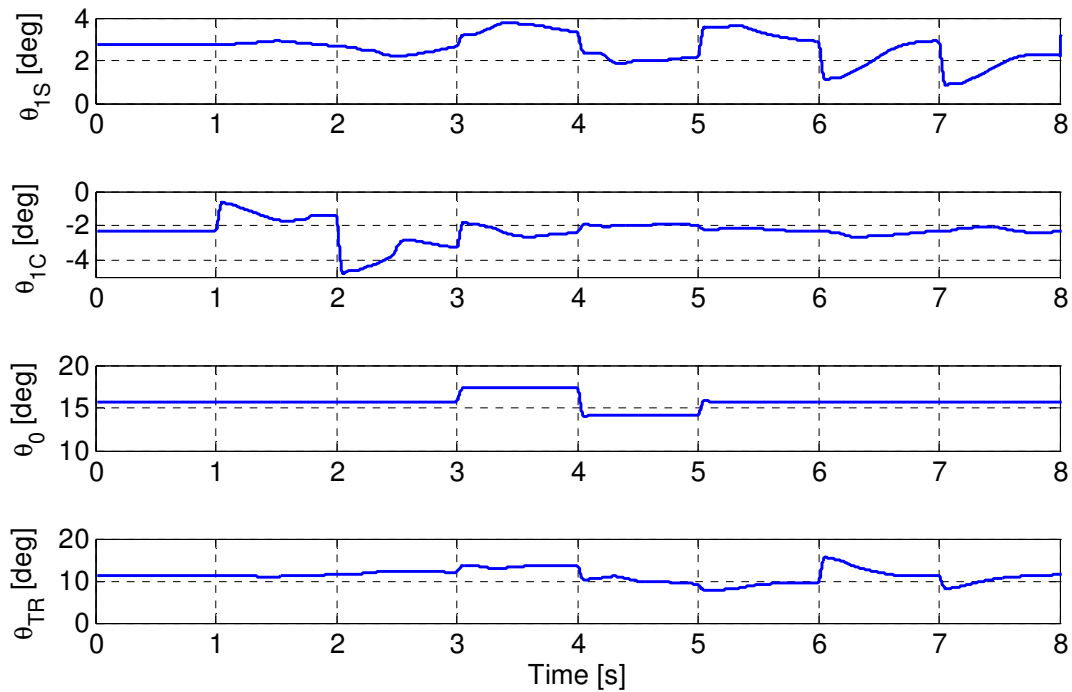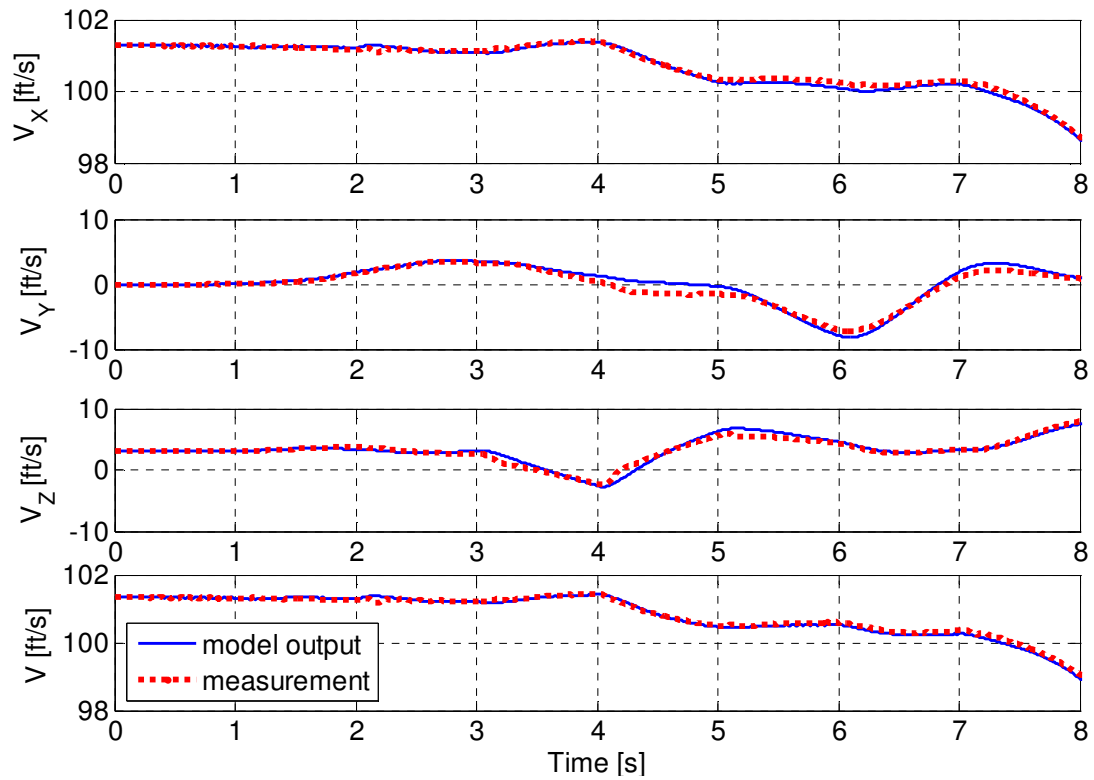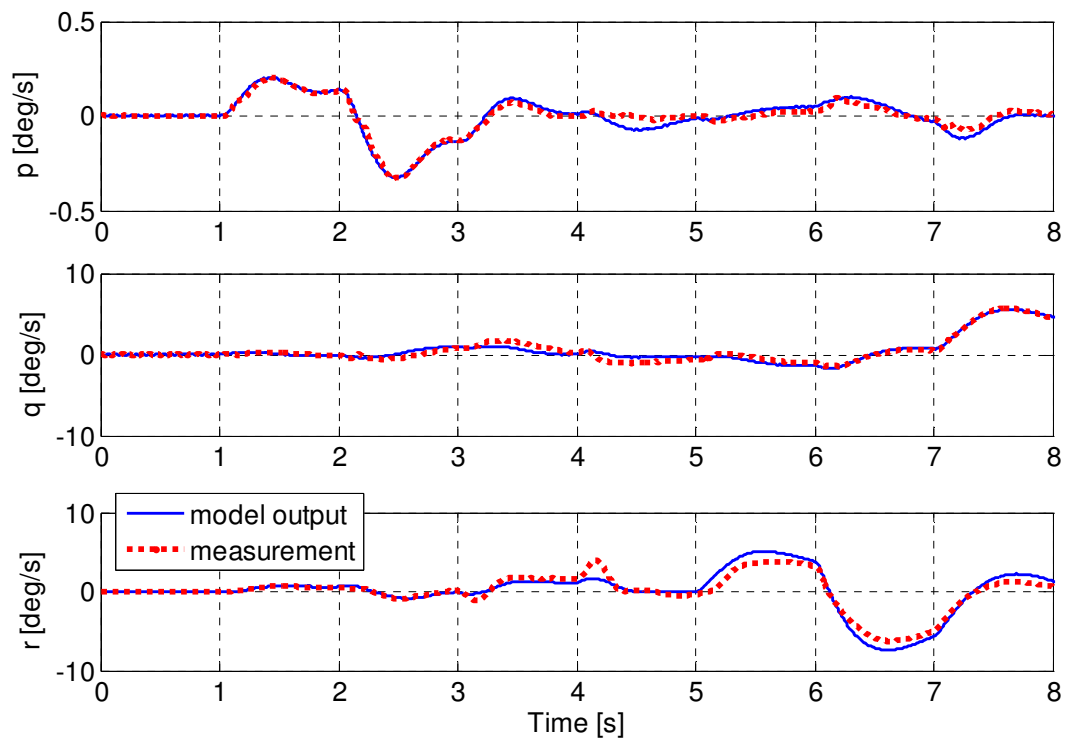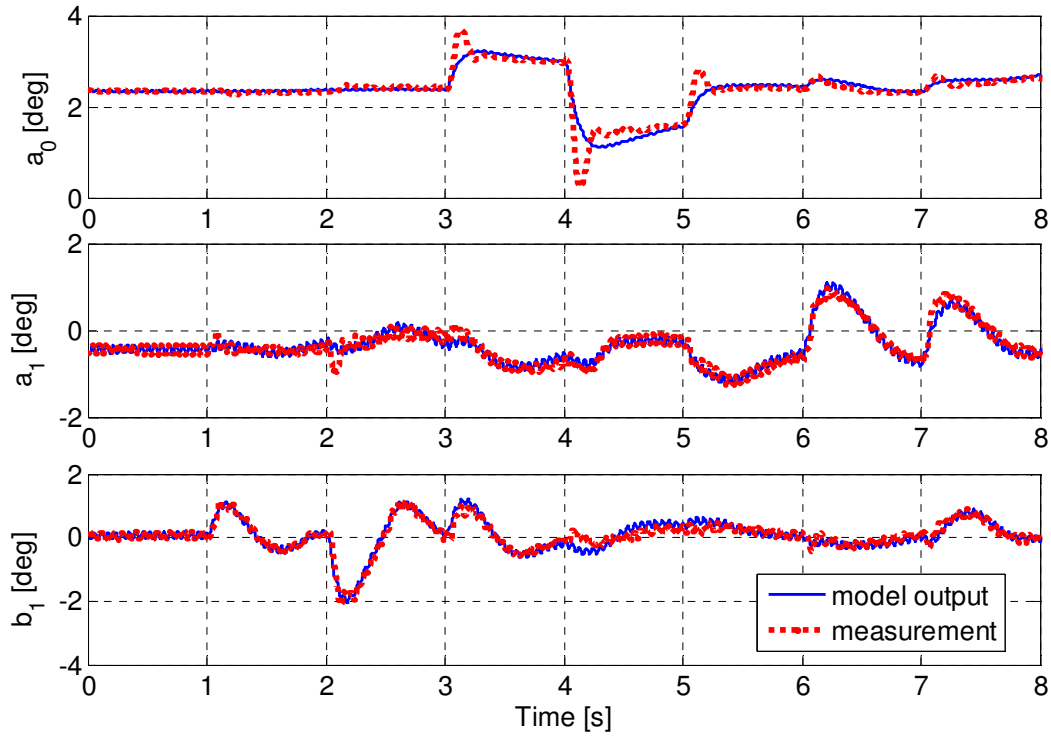
Figure 7.64 - Comparison between the true time histories of the rotor dynamics and the corresponding time histories provided by the identified model (test 2)

In conclusion the identified model is able to fast time simulate the performance of the vehicle, with some minor error which could be further reduced improving the model structure.

8 EXPERIMENTAL ASSESSMENTS

The proposed identification methodology was applied to actual flight data of the CIRA FTB1 vehicle, in order to identify the nominal aerodynamic model and reduce the related pre-flight uncertainties. Before describing the identification results, the FTB1 vehicle and the performed flight tests are introduced.

8.1 CIRA FTB1 Vehicle

In the framework of the Unmanned Space Vehicle (USV) program, the Italian Aerospace Research Centre developed two identical autonomous Flying Test Beds (called FTB1 but nicknamed Castore and Polluce), in order to perform flight missions for investigation of subsonic, transonic and low supersonic regimes. The FTB1 vehicles are unmanned and un-powered. They are winged slender configurations, with two sets of aerodynamic effectors: the elevons, that provide both pitch control when deflected symmetrically and roll control when deflected asymmetrically, and the rudders, that deflect only symmetrically to allow yaw control. Lateral-directional stability is enhanced by means of two ventral fins. A Hydraulic Actuator System controls the aerodynamic effectors. The on-board computers host the software that implements the guidance, navigation and control algorithms and manages subsystems and experimental payloads. One of the FTB1 vehicles is shown in Figure 8.1, while Figure 8.2 presents its three-view [AR1].

Figure 8.1 - FTB1 vehicle
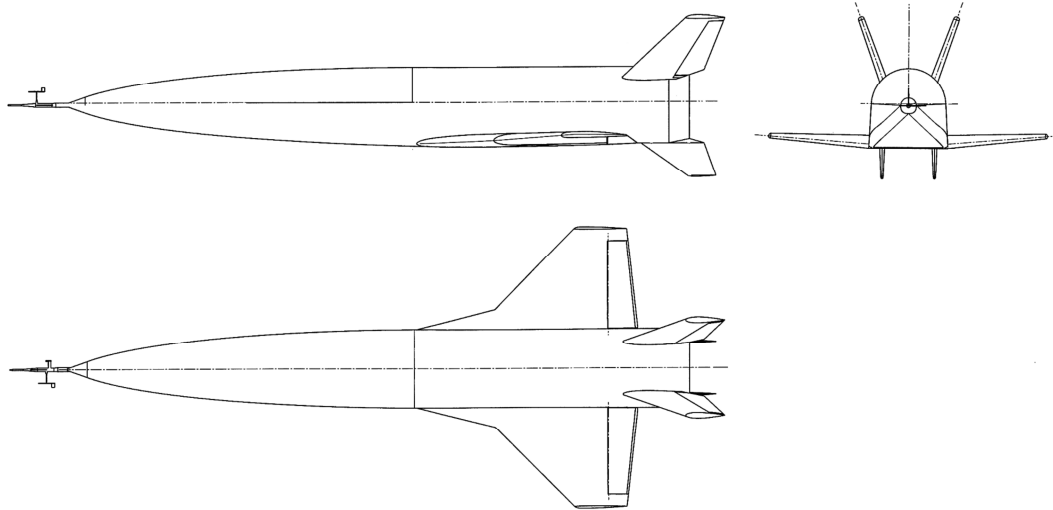
Figure 8.2 - FTB1 three-view

The navigation sensors suite of the FTB1 vehicles is composed of

- Commercial-Off-the-Shelf Inertial Measurement Unit (IMU), which uses three accelerometers, three fibres optic gyroscopes and a GPS unit to provide the inertial navigation measurements, that is, vehicle attitude and angular rate, CoM acceleration, velocity and position.

- Three-axial Magnetometer (MAG), which measures the magnetic field in order to compute the magnetic heading.

- Air Data System (ADS), composed of Air Data Computer (ADC) and air data boom, located on the nose of the vehicle; the ADS provides measurements of aerodynamic angles, static, impact and total pressure, static and total temperature, altitude, rate of climb, IAS, TAS, Mach number.

- Hydraulic System, which is the FTB1 actuation system and also performs the measurements of the angular deflections of the aerodynamic surfaces.

All the measurements gathered by the navigation suite during the FTB1 flight tests were low-pass filtered prior to recording, in order to reduce the noise. Moreover after the flight they were pre-processed to check calibration and synchronisation and to remove biases, in order to get the best estimation of navigation data [AR19].

8.2 DTFT Missions

The FTB1 vehicles performed two test missions in winter 2007 [AR20], [AR21] and in spring 2010 [AR19], [AR22], named Dropped Transonic Flight Test 1 and 2 (DTFT1 and DTFT2). Both mission profiles consisted of three main phases

- the ascent phase during which the carrier brought the vehicle at the release altitude (about 20 km for the first mission and 24 km for the second one) by means of a stratospheric balloon;

- the flight phase where the vehicle left the carrier and started a free flight accelerating to achieve the maximum Mach number;

- the deceleration phase where the vehicle opened a parachute system and ended its mission by water splash down.

Key mission phases of DTFT missions are shown from Figure 8.3 to Figure 8.5, whereas the time histories of Mach number and angle of attack for the two missions are presented in Figure 8.6. For both missions, the examined time frame starts 17 seconds after the vehicle drop, when the air data measurement noise was suitably low.
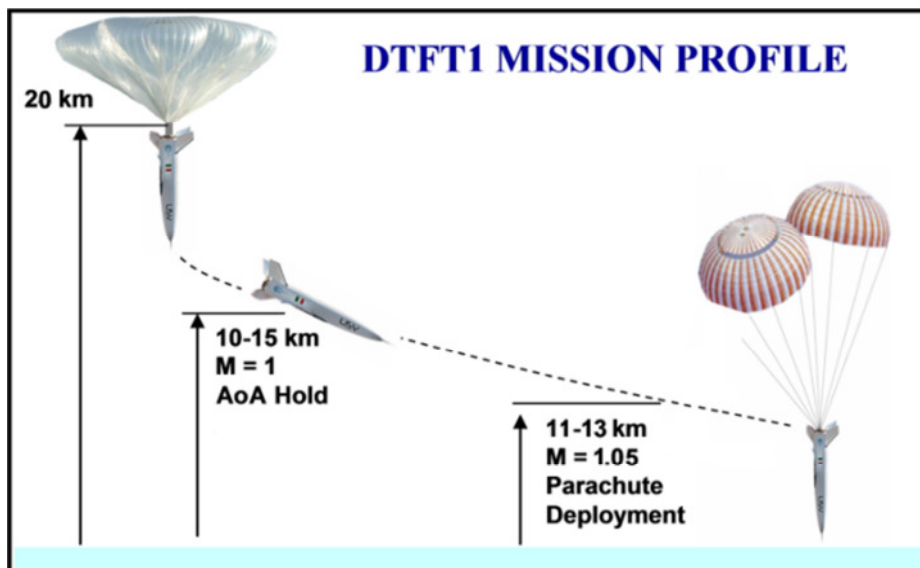
Figure 8.3 - Pictorial representation of the DTFT1 Missions Profile
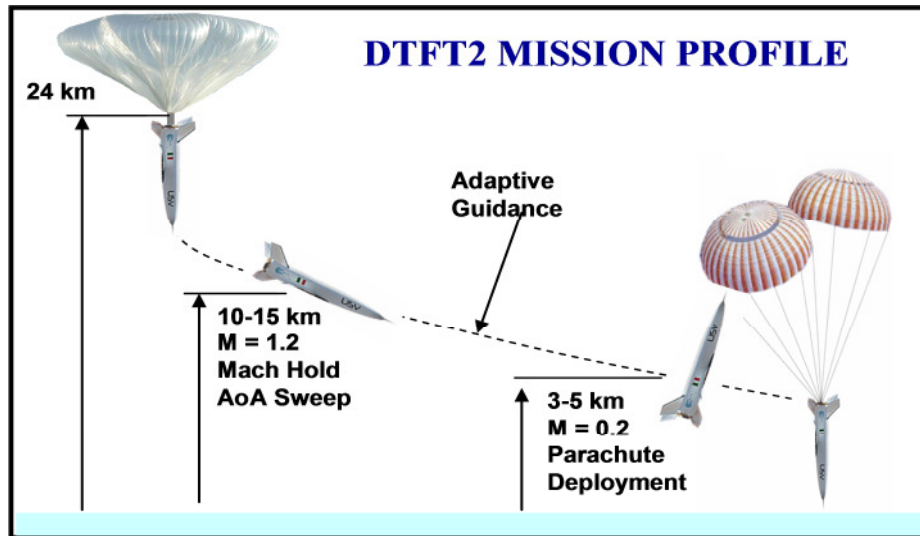
Figure 8.4 - Pictorial representation of the DTFT2 Missions Profile
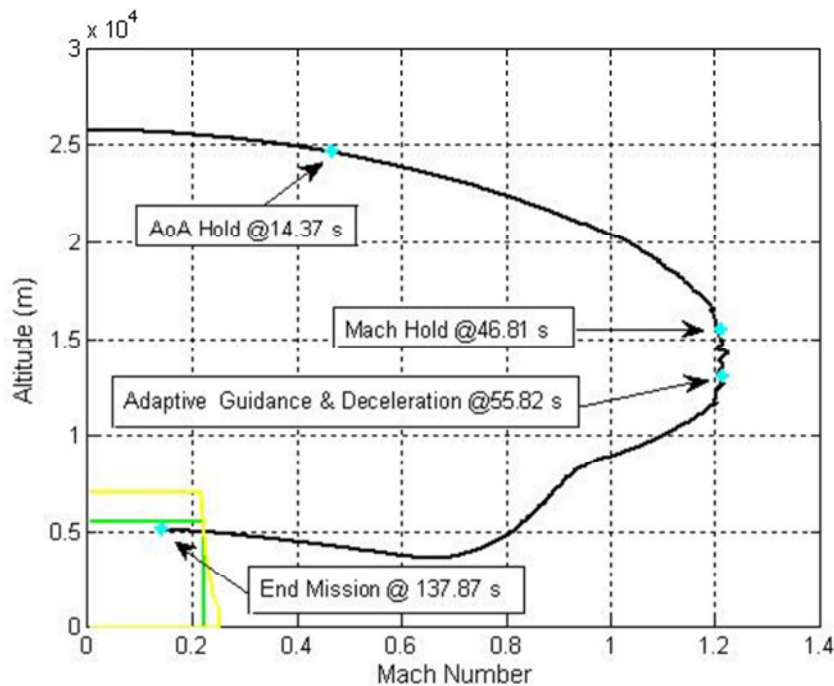
Figure 8.5 - DTFT2 Altitude vs. Mach profile (relevant phases are highlighted in the textboxes)

For DTFT1 Mach number varied from 0.57 to about 1.08, whereas the angle of attack was held nearly constant at about 7 degrees until 39 s. Transonic regime started about 31 s after the drop, where the displacement of the aerodynamic centre created a large perturbation in the pitch moment. At t = 39 s, due to a problem concerning the parachute deployment system, the flight control system switched into a safety mode. Consequently the aerodynamic control surfaces were brought to the neutral position, leading to the variations of α visible in the figure at t > 39 s that

resulted from the excitation of the short period dynamics of the vehicle. For the whole flight, the vehicle trajectory was basically longitudinal with the sideslip angle accurately tracking the 0 degree reference value. The flight was very short, lasting only about 44 seconds.
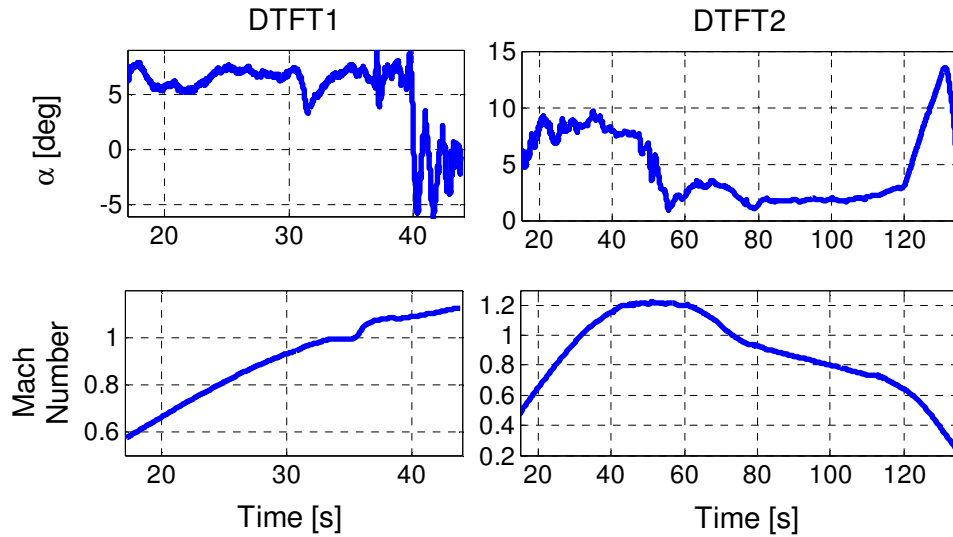
Figure 8.6 - Angle of attack and Mach number time histories for DTFT1 and DTFT2

Based on first mission experience, second mission was more complex. After release, the vehicle performed a pitch-up manoeuvre to reach and hold the specified value of the angle of attack while accelerating up to Mach 1.2 at about 15 km altitude; then a pull down manoeuvre was performed to keep the Mach number constant while a sweep in angle of attack was executed. The manoeuvre allowed the verification of the aerodynamic behaviour of the vehicle at constant Mach and variable angle of attack in full transonic regime as it would happen in a wind tunnel facility. At the end of this manoeuvre the vehicle began a pull up manoeuvre to decelerate to very low speeds (below Mach 0.2) and reached an altitude lower than 5 km where a subsonic parachute was opened, allowing a safe splash down of the vehicle. Transonic regime started about 30 s after the drop, while after 77 s the regime was again subsonic. The vehicle performed another sweep in angle of attack in subsonic regime at the end of the mission. The sideslip angle was almost always close to 0 degree reference value.

8.3   Model Identification Results and Discussion

For both the DTFT missions, the flight measurements of load factors, centre of mass velocity and position, angular velocity, Euler angles, aerodynamic angles, Mach number, total and static

pressure, total temperature and aerodynamic effectors deflections were provided as input to the identification process. During DTFT1, these data were recorded at different sampling rates (10Hz and 100Hz). They were re-sampled and synchronized at 100Hz prior to perform further analyses [AR23]. In the DTFT2 mission all the data were gathered at 100Hz. A compatibility check on the available measurements was also performed, by using kinematic relations [B1], in order to check the measurements consistency and the correctness of the measurement error characterisation.

Post-flight meteorological data, namely, static pressure, static temperature and mean wind velocity, provided by the European Centre for Medium-Range Weather Forecasts were also collected for identification purpose.

8.3.1 DTFT1 Data Analysis

Model identification was carried out using the flight data collected in the time interval [17, 44] seconds after the drop. Aerodynamic force and moment coefficients, wind velocity, static temperature and pressure, and vehicle state were estimated in the first identification step.

In Figure 8.7 the identified aerodynamic coefficients are compared with the ones provided by the pre-flight ADB along the DTFT1 trajectory. Although the coefficients returned by the pre-flight ADB were not far from the estimated values, an update of the pre-flight database appeared necessary. In particular, C_L was over predicted as well as C_D in the first 10 seconds of the considered time frame. The estimated values of C_m were very close to zero up to 39s flight time, whereas the same coefficient computed using the pre-flight ADB assumed negative values. Significant discrepancies between predicted and estimated values were also apparent in the plot of C_n versus time. Finally, the UKF notably reduced the uncertainties with respect to pre-flight ADB, as shown in Figure 8.8.

Figure 8.9 presents the comparison between the horizontal components of wind velocity estimated by UKF and computed through ECMWF. The UKF, extending the frequency content of wind velocity with respect to ECMWF, improved the evaluation of the wind field experienced by the vehicle during the flight which, in turn, had a positive effect on the filtering of the aerodynamic angles.
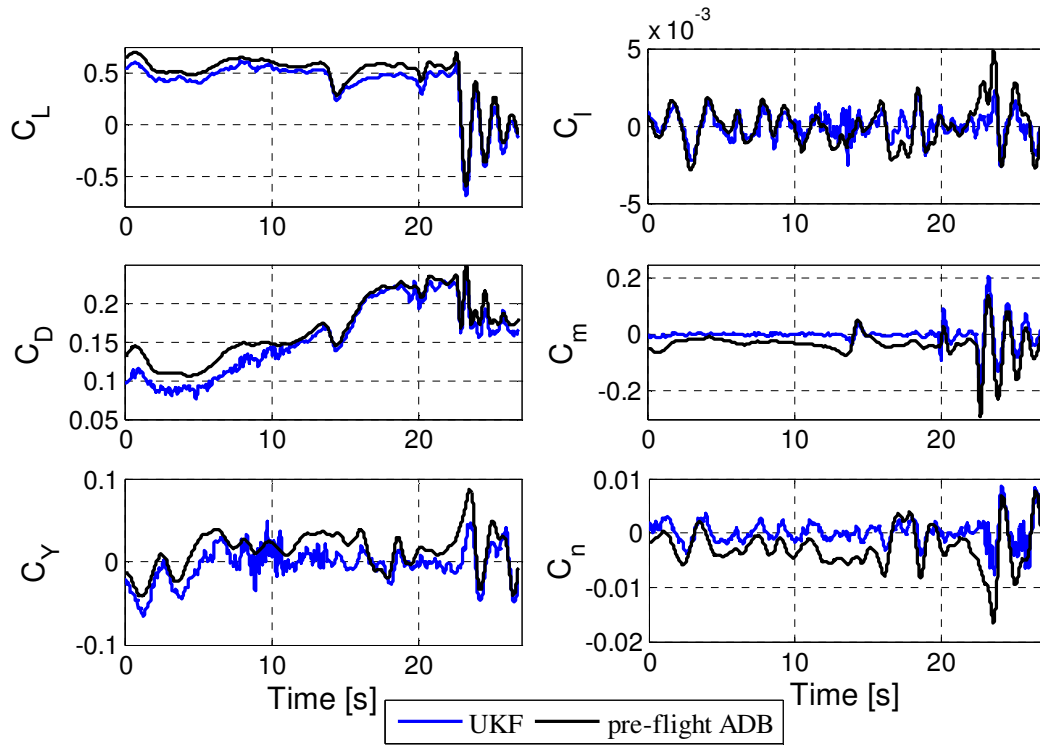
Figure 8.7 – Aerodynamic coefficients time histories estimated by UKF and provided by the pre-flight ADB
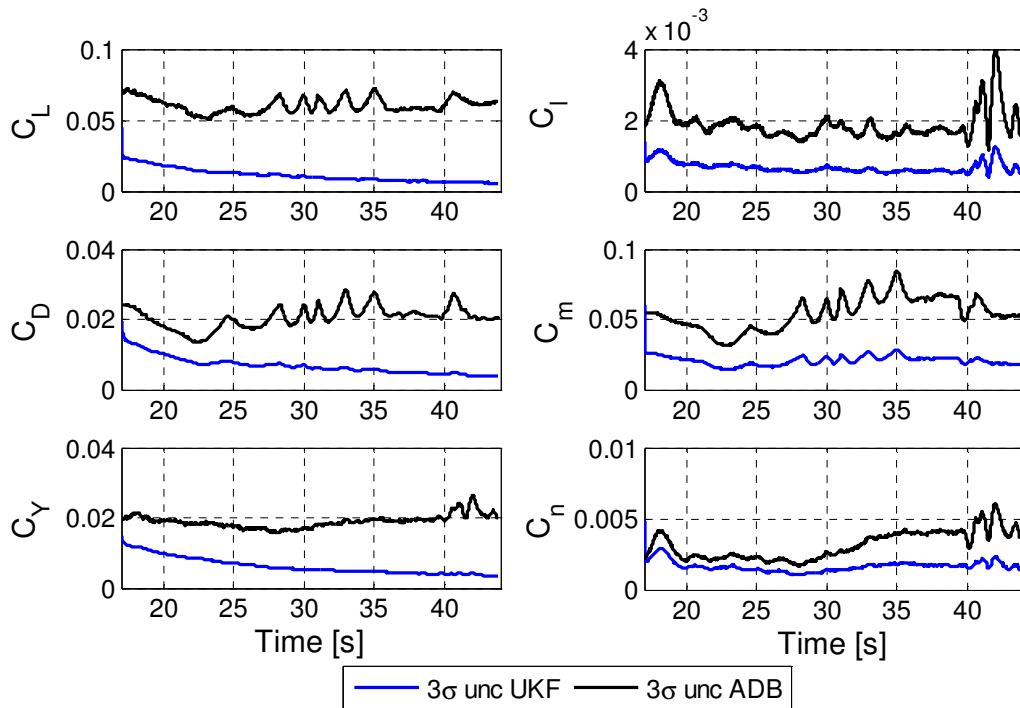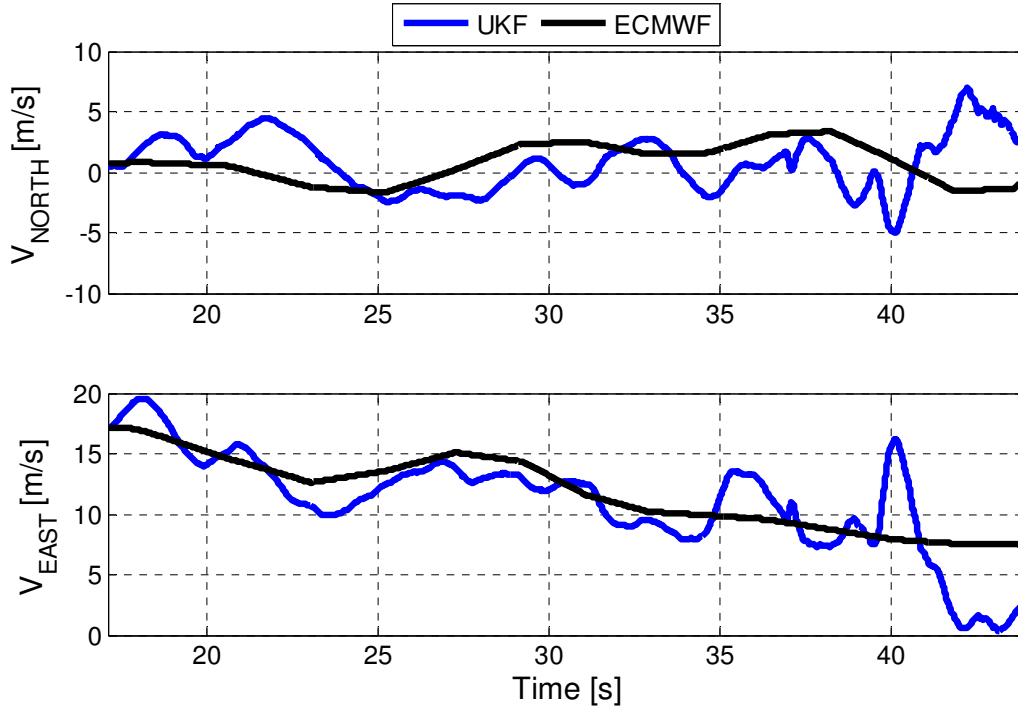

Figure 8.8 – Comparison between pre-flight and UKF estimation of the uncertainties on the aerodynamic coefficients along the DTFT1 trajectory

Figure 8.9 – Horizontal components of wind velocity (in NED reference frame) estimated by UKF and provided by ECMWF

Not shown for the sake of conciseness, the estimated values of Down component of wind velocity, static temperature and pressure were very close to the ECMWF predictions, whereas the filtered states of the vehicle were nearly indistinguishable from the in-flight measurements.

In the second identification step the analytical aerodynamic model was updated only for the longitudinal coefficients, because the flight trajectory was basically longitudinal and there was little excitation of lateral-directional dynamics. For DTFT1, both UKF and LS estimation techniques were used in this step.

Attention was focused on the gains in Eq. 75 and Eq. 81, namely ϑ_{sub} and ϑ_{sup}. 6 aerodynamic parameters were estimated in subsonic regime, 3 related to drag coefficient and 3 to lift, by using the flight measurements gathered from 17s through 36s flight time. Cramer Rao bounds enhanced that, no parameters could be estimated for the pitch moment coefficient in the subsonic regime, due to the low excitation of attitude dynamics. In transonic regime, from 38s to 44s, 10 parameters were estimated, related to the supersonic drag coefficient (3 parameters), lift coefficient (3 parameters) and pitch moment coefficient (4 parameters). The estimated parameters were basically related to zero-order terms and to the aerodynamic derivatives with

respect to α and δ_e. Each longitudinal coefficient was analysed independently and parameter estimation in subsonic and supersonic regimes was also carried out independently. Figure 8.10 shows the convergence characteristics of the UFK estimation of the parameters related to the lift coefficient in subsonic regime. Similar plots were obtained for the other coefficients.
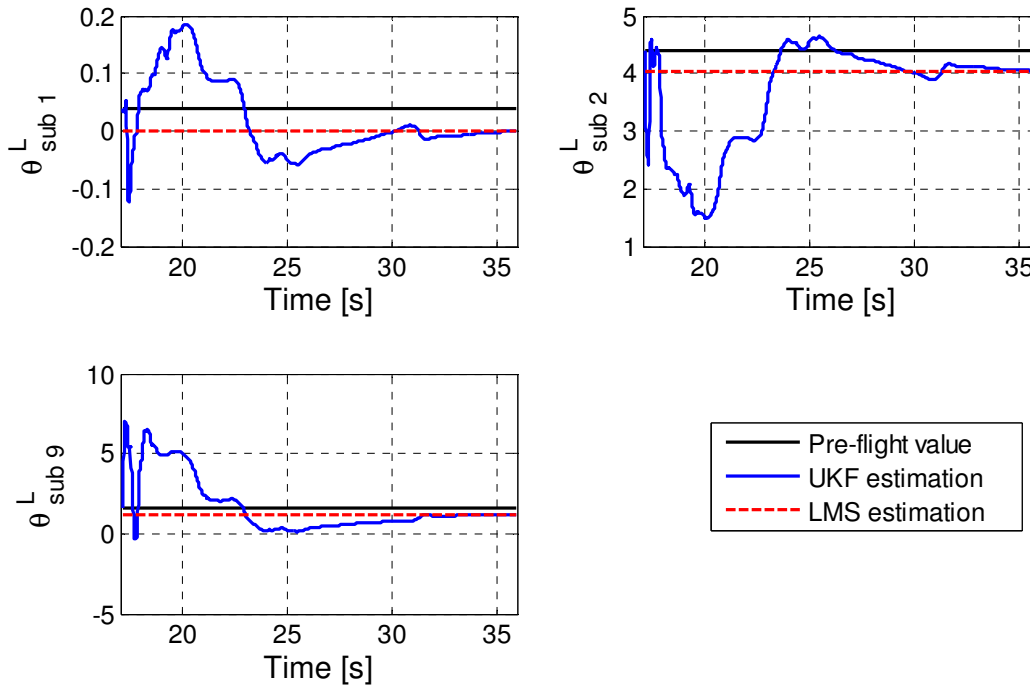

Figure 8.10 - Estimation of the subsonic lift parameters

The estimated parameters are listed in Table 8.1 and Table 8.2 for subsonic and supersonic regimes, respectively. The tables also show the pre-flight values of the parameters and the estimation uncertainties evaluated by the UKF. LS and UKF estimations are always very close. All the analytical model parameters which are not listed in the table were held constant to their pre-flight values.

Gain related to	Pre-flight value	UKF Estimation	LS Estimation	UKF Standard deviation
$C_{L\,0}$	0.04	5e-4	5e-4	1e-4
$C_{L\,\alpha}$	4.41	4.04	4.04	1e-3
$C_{L\,\delta e}$	1.59	1.23	1.23	1e-3
$C_{D\,0}$	0.059	0.048	0.051	1e-3
$C_{D\,\alpha}$	-6e-5	2e-4	3e-4	1e-5
$C_{D\,\alpha}^{2}$	4.12	3.11	2.81	0.05

Table 8.1 – Estimated aerodynamic parameters in subsonic regime

Gain related to	Pre-flight value	UKF Estimation	LS Estimation	UKF Standard deviation
$C_{L\,0}$	-0.32	0.19	0.19	3e-3
$C_{L\,\alpha}$	8.14	7.97	7.97	0.015
$C_{L\,\delta e}$	0.86	0.70	0.69	6e-3
$C_{D\,0}$	-1.29	-1.18	-1.18	5e-3
$C_{D\,\alpha}$	-0.13	-0.30	-0.22	0.02
$C_{D\,\alpha}{}^2$	4.81	6.32	7.16	0.11
$C_{m\,0}$	-0.06	4e-3	4e-3	7e-3
$C_{m\,\alpha}$	-0.22	-0.17	-0.17	0.01
$C_{m\,q}$	-4.15	-6.79	-6.67	4.56
$C_{m\,\delta e}$	-1.49	-0.98	-0.98	0.07

Table 8.2 - Estimated aerodynamic parameters in supersonic regime

8.3.2 DTFT2 Data Analysis

The DTFT2 mission allowed to validate on a different trajectory the post flight results of DTFT1 and to further refine the aerodynamic model by estimating also several lateral-directional parameters.

The time histories of longitudinal global aerodynamic coefficients estimated in the first identification step are plotted in Figure 8.11, denoted as UKF coefficients. In the same figure, the analogous trajectories provided by the analytical aerodynamic model identified from the DTFT1 data, denoted in the following as PFA1 model, are reported. For lift and drag coefficients the matching between UKF and PFA1 was very good in the time frames [30, 70] seconds and after 120 seconds. Instead, the PFA1 was not able to fit the UKF estimation between 70 and 120 seconds (especially for C_L). The PFA1 model was identified using the data of DTFT1. In that mission, the vehicle flew at an angle of attack of about 7 degrees in subsonic regime and for few seconds at angle of attack varying between about -5 and 7 degrees in supersonic regime. The PFA1 model was able to match the UKF estimation along the DTFT2 trajectory when the flight conditions were similar to the one experienced in DTFT1. When an extrapolation to other flight envelope points was requested, the model did not work very well, as it happened between 70 and 120 seconds. Concerning the pitching moment coefficient, PFA1 was very close to UKF estimation, but it was not able to reproduce exactly the about zero mean trajectory experienced in flight. In conclusion, the PFA1 model could be improved if more test points were used for the identification of its parameters.

The estimated trajectories of aerodynamic coefficients are also compared in Figure 8.12 with the one provided by the pre-flight ADB. Matching between ADB and UKF was generally good, but for C_m in most of the trajectory, C_D in the very last part of the trajectory and lateral directional coefficients in the time interval from 60s to 80s. Since in transonic regime the sideslip angle was always null, except for the interval from 60s to 80s, where it varies between 2 degrees and -2 degrees, it could be argued that ADB lateral directional coefficients seem to be too sensitive to sideslip angle variations in transonic regime. As for the pitching moment coefficient, the trajectory trends of the ADB was completely different from the UKF. The vehicle performed the mission in conditions very close to rotational equilibrium with respect to pitch, indeed the estimated pitch moment was about zero. On the contrary, the C_m profile provided by the ADB varied significantly and it was most of the time different from zero.

Based on these considerations, a refinement of the model was performed in the second identification step. 71 aerodynamic parameters were estimated (31 longitudinal and 40 lateral-directional) using the LS technique, and the obtained values are listed in Table 8.3 and Table 8.4.

The analytical aerodynamic model identified from DTFT2 data was used to compute the aerodynamic coefficients time histories along the DTFT2 trajectory. The obtained results are shown in Figure 8.13 (for the force coefficients) and Figure 8.14 (for the moment coefficients), where they are compared with the time histories estimated by the UKF in the first identification step. The matching was generally very good, both in subsonic and in supersonic regimes, for all the coefficients but the pitching moment, the mean value of which was different from zero in some parts of the trajectory. This problem could be due to some of the parameters which were not updated using the flight data. However also for this coefficient the identified model worked notably better than the pre-flight ADB. Moreover, model identification allowed to significantly reduce the aerodynamic uncertainties, thus supporting the development of enhanced flight control algorithms suited to reliably and accurately manage the vehicle trajectories in an extended flight envelope.
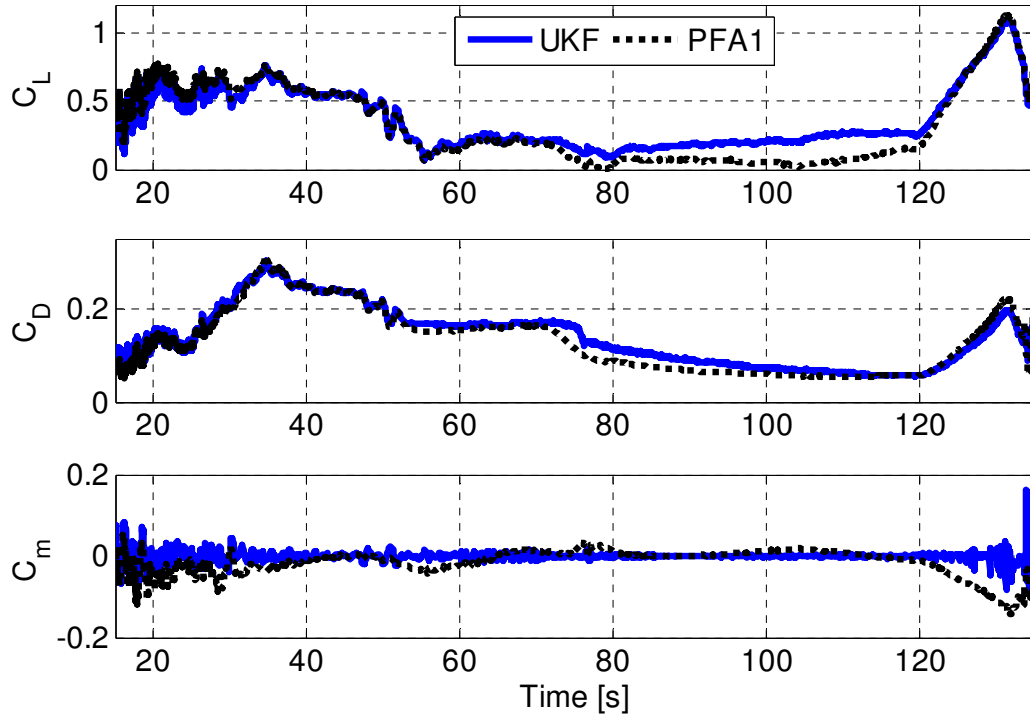
Figure 8.11 - Comparison between longitudinal coefficients estimated in the first step (UKF) and provided by the analytical aerodynamic model identified from DTFT1 data (PFA1)
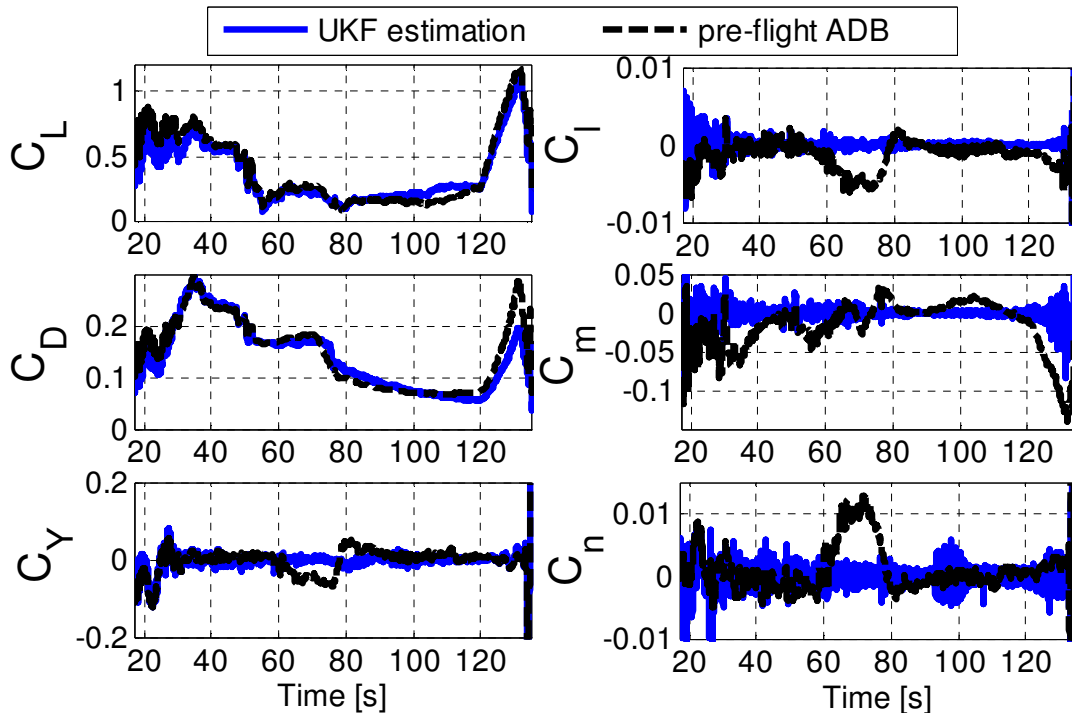

Figure 8.12 - Pre-flight ADB and estimated aerodynamic coefficients versus time

Aerodynamic Coefficient	Subsonic			Supersonic		
	Gain of Function	Estimated Value	Uncertainty Range (1σ)	Gain of Function	Estimated Value	Uncertainty Range (1σ)
C_L	$\vartheta^L_{sub\,1}$	0.08618	0.001593	$\vartheta^L_{sup\,1}$	-0.00169	0.0043904
	$\vartheta^L_{sub\,2}$	2.763	0.020501	$\vartheta^L_{sup\,2}$	8.1499	0.045735
	$\vartheta^L_{sub\,3}$	3.1858	0.053243	$\vartheta^L_{sup\,3}$	-23.482	0.64417
	$\vartheta^L_{sub\,4}$	-14.909	0.72507	-	-	-
	$\vartheta^L_{sub\,9}$	1.4244	0.001593	$\vartheta^L_{sup\,9}$	0.7604	0.014162
	$\vartheta^L_{sub\,10}$	2.9644	0.020501	-	-	-
C_D	$\vartheta^D_{sub\,1}$	0.05962	0.00085754	$\vartheta^D_{sup\,1}$	-1.3624	0.005843
	$\vartheta^D_{sub\,2}$	0.00049	2.328e-005	$\vartheta^D_{sup\,2}$	-1.4503	0.093297
	$\vartheta^D_{sub\,3}$	2.2953	0.025972	$\vartheta^D_{sup\,3}$	7.9961	0.10558
	$\vartheta^D_{sub\,4}$	0.7757	0.31419	-	-	-
	$\vartheta^D_{sub\,9}$	0.01161	0.02735	$\vartheta^D_{sup\,9}$	0.2377	0.02958
	$\vartheta^D_{sub\,10}$	3.7754	0.34646	-	-	-
C_m	$\vartheta^m_{sub\,1}$	-0.01048	0.002284	$\vartheta^m_{sup\,1}$	0.000974	0.0042446
	$\vartheta^m_{sub\,2}$	-0.01081	0.003891	$\vartheta^m_{sup\,2}$	-0.01824	0.0034904
	$\vartheta^m_{sub\,3}$	0.2852	0.062878	$\vartheta^m_{sup\,3}$	1.983	0.46174
	$\vartheta^m_{sub\,5}$	-10.073	4.9619	-	-	-
	$\vartheta^m_{sub\,6}$	1.5538	1.0268	-	-	-
	$\vartheta^m_{sub\,9}$	-0.2610	0.035673	$\vartheta^m_{sup\,9}$	-0.1207	0.017268
	$\vartheta^m_{sub\,10}$	-2.4723	0.31154	-	-	-

Table 8.3 – Estimated longitudinal aerodynamic parameters

Aerodynamic Coefficient	Subsonic			Supersonic		
	Gain of Function	Estimated Value	Uncertainty Range (1σ)	Gain of Function	Estimated Value	Uncertainty Range (1σ)
C_Y	$\vartheta^Y_{sub\,1}$	-1.4926	0.028766	$\vartheta^Y_{sup\,1}$	0.5956	0.039792
	$\vartheta^Y_{sub\,2}$	0.00045	0.00016305	$\vartheta^Y_{sup\,2}$	-50.557	2.9226
	$\vartheta^Y_{sub\,6}$	-14.469	1.0317	-	-	-
	$\vartheta^Y_{sub\,12}$	0.5394	0.033496	$\vartheta^Y_{sup\,12}$	145.6	2.517
	$\vartheta^Y_{sub\,13}$	-2.4808	0.097419	$\vartheta^Y_{sup\,13}$	1.9208	0.056646
	$\vartheta^Y_{sub\,15}$	1.4136	0.03013	$\vartheta^Y_{sup\,15}$	36.236	0.85527
	$\vartheta^Y_{sub\,16}$	-9.4546	0.31564	-	-	-
C_l	$\vartheta^l_{sub\,1}$	0.01149	0.004649	$\vartheta^l_{sup\,1}$	0.04745	0.003043
	$\vartheta^l_{sub\,2}$	-0.2928	0.056071	$\vartheta^l_{sup\,2}$	-17.483	1.0451
	$\vartheta^l_{sub\,3}$	-0.6212	0.054896	$\vartheta^l_{sup\,3}$	-2.1736	0.193
	$\vartheta^l_{sub\,4}$	-1.1229	0.5649	-	-	-
	-	-	0.003207	$\vartheta^l_{sup\,7}$	-0.8424	0.15954
	$\vartheta^l_{sub\,12}$	0.1267	0.006955	$\vartheta^l_{sup\,12}$	-0.2850	0.014899
	-	-	0.010674	$\vartheta^l_{sup\,13}$	0.03483	0.002209
	$\vartheta^l_{sub\,15}$	-0.05158	0.004649	-	-	-
	$\vartheta^l_{sub\,17}$	0.03185	0.056071	$\vartheta^l_{sup\,17}$	0.9995	0.021953
C_n	$\vartheta^n_{sub\,1}$	-0.01527	0.003319	$\vartheta^n_{sup\,1}$	-0.1036	0.0055153
	$\vartheta^n_{sub\,2}$	0.6422	0.053631	$\vartheta^n_{sup\,2}$	0.01066	0.0004218
	$\vartheta^n_{sub\,3}$	-0.9100	0.24872	-	-	-
	$\vartheta^n_{sub\,4}$	5.4934	0.63716	-	-	-
	$\vartheta^n_{sub\,6}$	12.454	1.4386	$\vartheta^n_{sup\,6}$	-400.95	12.479
	$\vartheta^n_{sub\,12}$	0.1141	0.008945	$\vartheta^n_{sup\,12}$	0.1061	0.003373
	$\vartheta^n_{sub\,13}$	-0.3344	0.066093	$\vartheta^n_{sup\,13}$	-9.4601	0.28657
	$\vartheta^n_{sub\,15}$	-0.03538	0.004323	$\vartheta^n_{sup\,15}$	-1.1273	0.027418

Table 8.4 - Estimated lateral-directional aerodynamic parameters
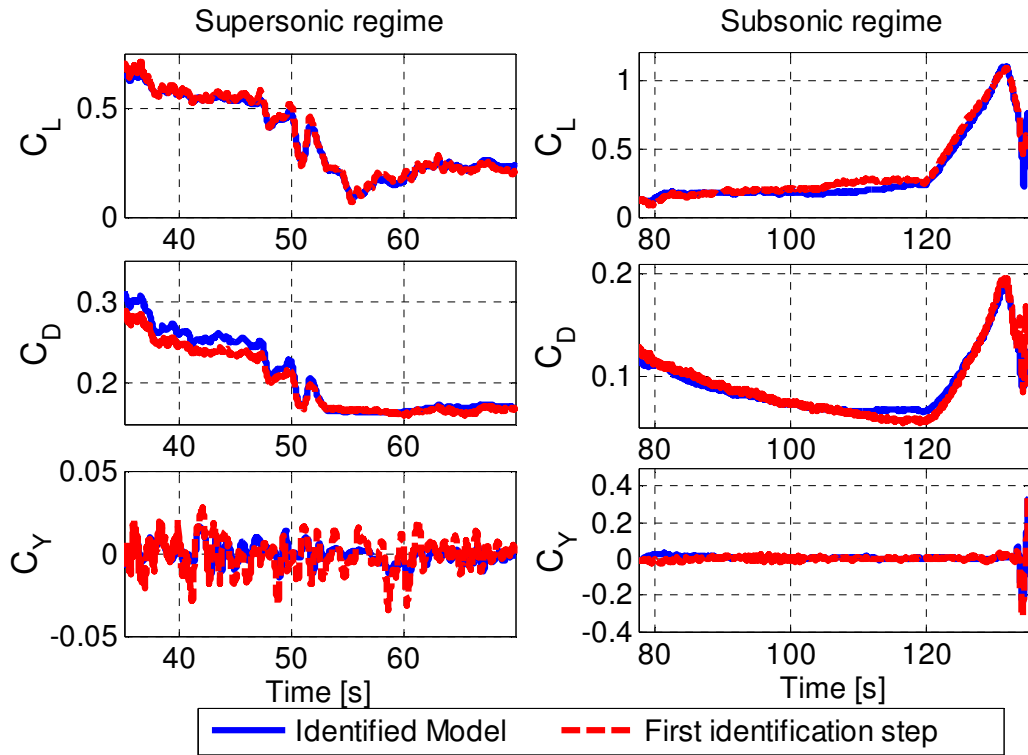
Figure 8.13 - Comparison between aerodynamic force coefficients estimated in first identification step and provided by the identified model
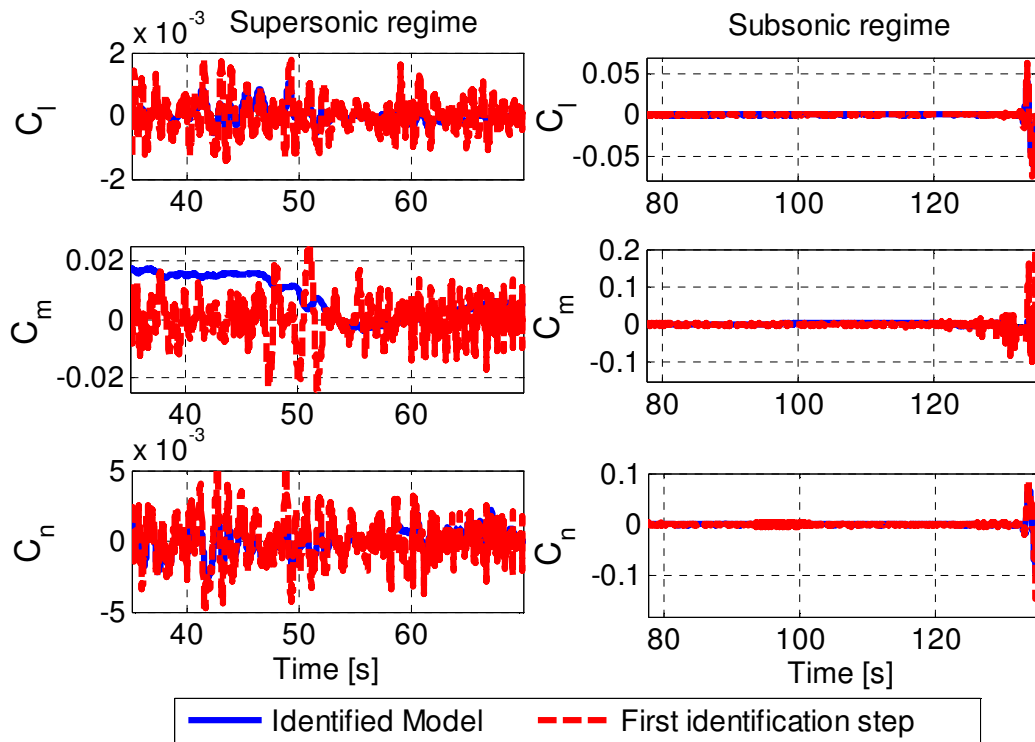
Figure 8.14 - Comparison between aerodynamic moment coefficients estimated in first identification step and provided by the identified model

8.4 Model Validation

For both the examined missions, the identification results were validated through an open loop simulation (that is, without considering the action of the flight control system). The in-flight measurements of aerodynamic effectors deflections, together with the estimated wind velocity, were provided as input to the vehicle simulation model, which also included the identified analytical aerodynamic model, and the simulation outputs were compared with the corresponding flight measurements.

The aerodynamic model identified from the DTFT1 data only provided lift and drag coefficients along the whole trajectory and pitch moment coefficient in supersonic regime. The coefficients which cannot be computed by the aerodynamic model, that is the subsonic pitch moment and the lateral-directional aerodynamic coefficients, were replaced by the time histories estimated in the first identification step. The output of the simulation for the DTFT1 mission are shown in Figure 8.15, where excellent agreement between flight data and simulation output is apparent. It is worth noting that, if the same verification was performed with the pre-flight ADB, the simulation results showed an unsteady behaviour of the vehicle, which is totally in disagreement with the actual flight measurement.

The aerodynamic model identified from the DTFT2 data allowed computing all the aerodynamic coefficients. If the complete aerodynamic model was used in the open loop simulation, the simulation outputs diverged from the flight measurements. If the aerodynamic force coefficients were computed through the identified model, whereas the moment coefficients were replaced by their time histories estimated in the first identification step, then simulation results were very close to the flight measurements, as shown in Figure 8.16 and Figure 8.17 and in Table 8.5, where the Theil's coefficients for this simulation are reported. Theil's coefficients are lower than 0.25 for all the measurements, confirming the good quality of the matching. These results corroborate the reliability of the estimated force model, whereas some more investigations are required on the aerodynamic moments model. It is worthy to note that the difficulty to validate the model for the aerodynamic moments (in particular the pitching moment) was already enhanced when simulated flight data were used to assess the identification methodology, as described in section 7.1.4.
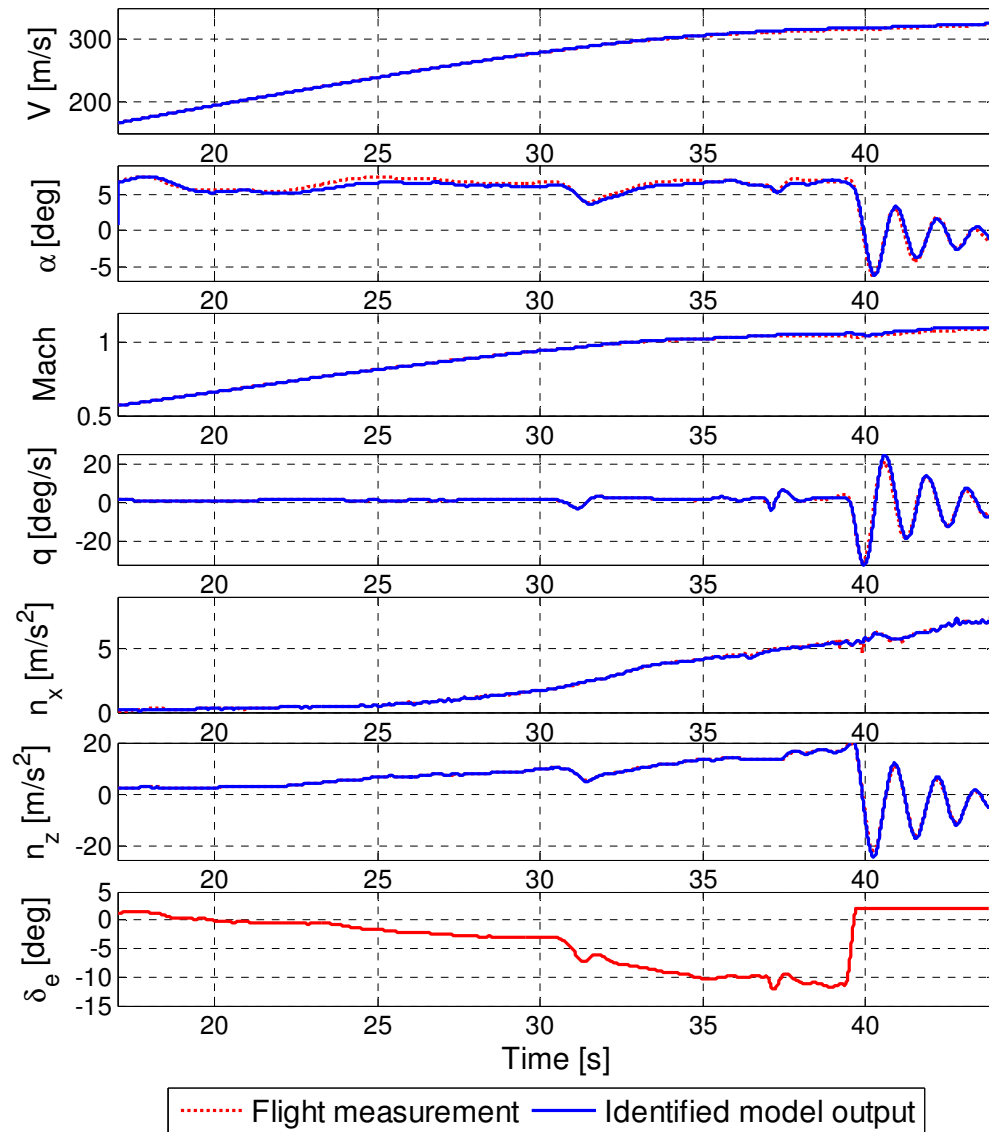
Figure 8.15 – Time histories comparison of flight measurements and estimated model responses for DTFT1
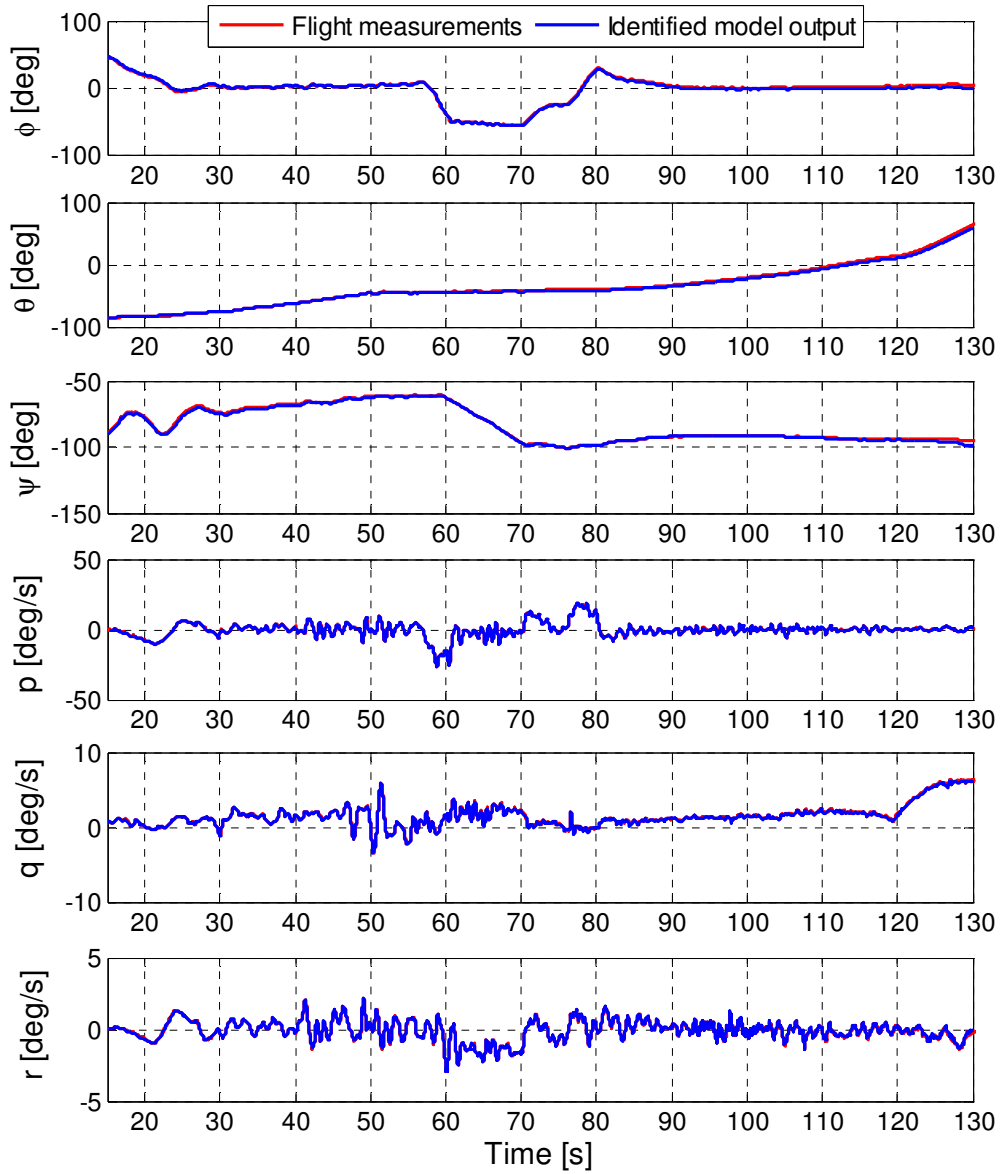
Figure 8.16 - Time histories comparison of flight measurements and estimated model responses for DTFT2 (Euler angles and angular rate)
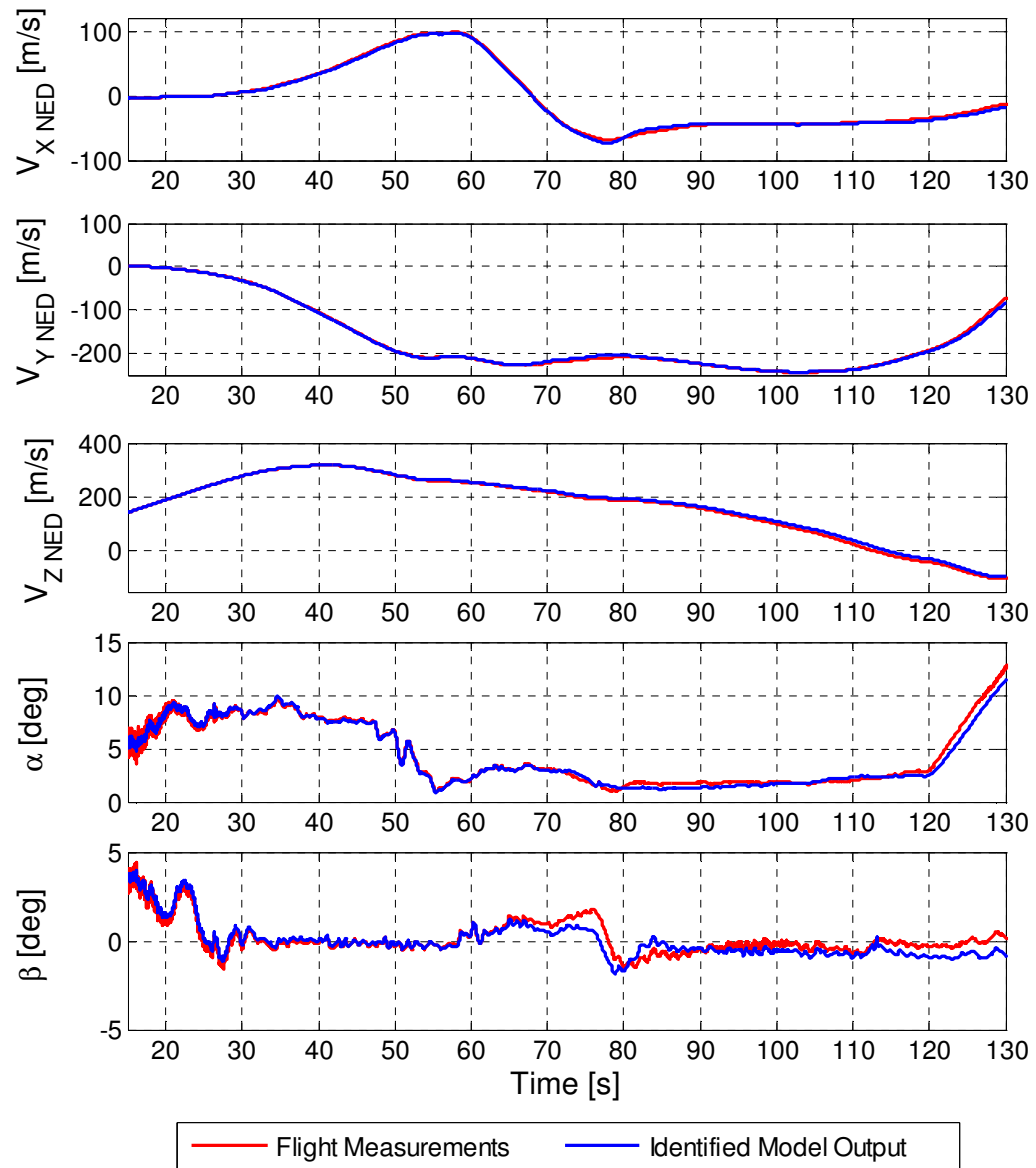
Figure 8.17 - Time histories comparison of flight measurements and estimated model responses for DTFT2 (velocity and aerodynamic angles)

Measurement	Theil's Coefficient
roll angle	0.0423
pitch angle	0.0202
yaw angle	0.0052
roll rate	0.0073
pitch rate	0.0141
yaw rate	0.0204
north velocity	0.0235
east velocity	0.0067
down velocity	0.0164
angle of attack	0.0369
angle of sideslip	0.2277

Table 8.5 – Theil's coefficients for the DTFT2 mission

9 CONCLUSIONS

An innovative methodology was presented in this thesis, which is able to face some of the open issues and challenges of aerospace vehicle system identification from flight data. The methodology was applied to determine the dynamical characteristics of a rotorcraft vehicle and the transonic aerodynamic model of an atmospheric re-entry space demonstrator. In the latter application, specific identification manoeuvres were not performed, due to safety constraints.

Proposed system identification methodology is carried out in the framework of a multi-step approach, which allows to decompose the complex starting problem in simplified sub-problems and to specify a suitable estimation technique compliant with each sub-problem objective, exploiting the advantage of both time-domain and frequency-domain methods. The straightforward combination of several consolidated estimation techniques brings to an identified model which is applicable in a wide frequency range. Furthermore, the proposed methodology is suitable to deal with problems where identification manoeuvres are minimised, indeed the identification can be executed only for the sub-model which is in fact identifiable.

The definition of the model structure is a critical task in system identification process. Indeed in the present thesis the selection of suitable models was performed for both the examined test cases, based on physical considerations and engineering judgment.

Another relevant peculiarity of the proposed approach concerns the exploitation of all the available a priori information and the rigorous management of all the uncertainties involved in the system identification procedure. As a result, a reliable, complete, and structured statistical characterisation of the identified model could be obtained.

The effectiveness of the system identification methodology was demonstrated through numerical assessments, which enhanced the capability to catch the true values of the model parameters and to reproduce the phenomena of interest. Moreover, the application to actual flight data of the CIRA FTB1 re-entry demonstrator allowed to validate and refine the available pre-flight aerodynamic model of the vehicle, in terms of nominal values update and significant reduction on model uncertainties.

Although more investigations are still needed, in particular concerning the identification of the nominal values for the aerodynamic moments, the obtained results are very promising and justify

the importance of flight tests and, in particular, of system identification from flight data. Indeed, the availability of an updated aerodynamic model represents a fundamental step for the development of the upgraded version of the Guidance, Navigation and Control system for the next missions of the same configuration, where the accuracy of estimates and the reliability of the model over an expanded flight envelope will be carefully analysed and assessed.

10 APPENDIX A: REFERENCE FRAMES

The following reference frames are used for modelling purposes in the present thesis [B30], [B47], [AR18].

- ## *NED Reference Frame*

The *North-East-Down* (NED) coordinate system is used in combination with flat non rotating Earth assumption in order to be considered an inertial reference system. This orthogonal reference frame has its origin on a point of the Earth surface, typically assumed to be 0m altitude with a vertical axis (*z*) directed positively towards the Earth centre and the horizontal plane with *x* axis directed through the North and *y* axis directed to East.

- ## *Body Reference Frame*

The *Body-fixed Reference* (BFR), indicated with the subscript *B*, is a right-handed triad, fixed with the vehicle, with the origin in its Centre of Mass. The longitudinal axis X_B is placed in the vehicle plane of symmetry, with its positive direction toward the nose, the Z_B axis is normal to X_B, placed in the same plane of symmetry, and direct positively downward, and the Y_B axis completes the triad, resulting positively oriented toward the right side. The vehicle attitude with respect to the Inertial Reference Frame is defined by three Euler angles:

- Ψ (*Yaw Angle*), the first rotation around the z-axis of the Inertial Reference Frame;

- Θ (*Pitch Angle*), the second rotation, around the y-axis of the Reference Frame obtained after the first rotation;

- Φ (*Roll Angle*), the last rotation, around the x-axis of the Reference Frame obtained after the second rotation.

The rotation matrix that allows to pass from the Inertial Reference Frame to the Body Reference Frame is the following:
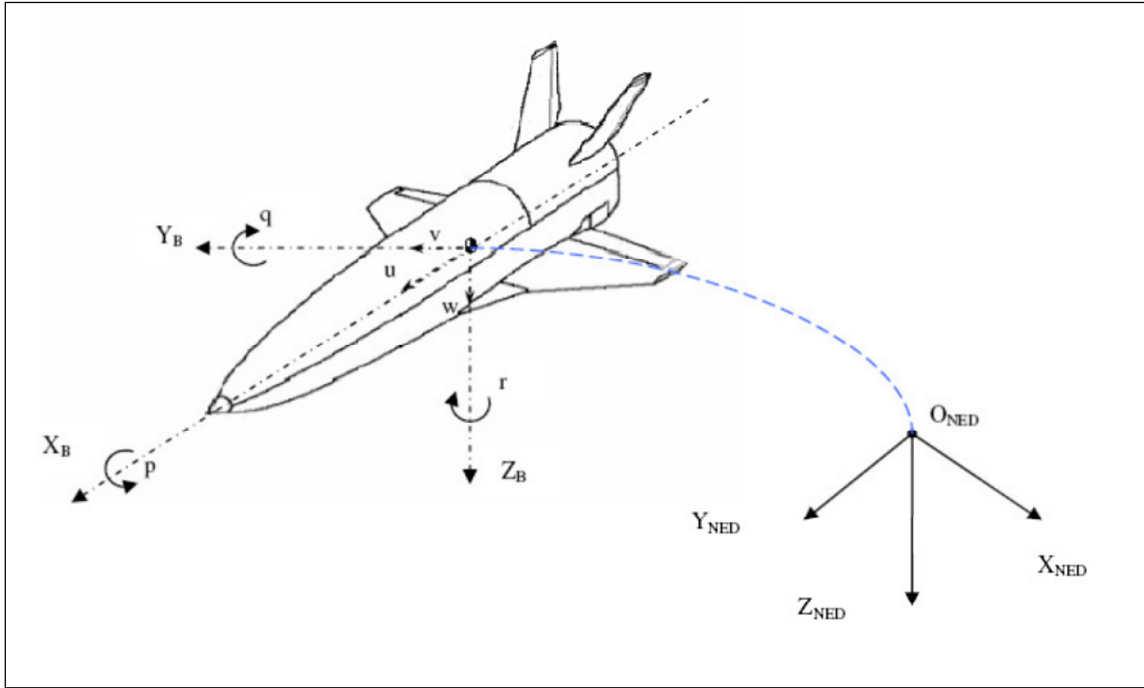
Figure 10.1 – NED and Body Reference Frames

$$\text{Eq. 131} \quad \mathbf{R}^{B}_{NED} = \begin{bmatrix} \cos\Theta\cos\Psi & \cos\Theta\sin\Psi & -\sin\Theta \\ \sin\Theta\sin\Phi\cos\Psi - \cos\Phi\sin\Psi & \sin\Theta\sin\Phi\sin\Psi + \cos\Phi\cos\Psi & \sin\Phi\cos\Theta \\ \sin\Theta\cos\Phi\cos\Psi + \sin\Phi\sin\Psi & \sin\Theta\cos\Phi\sin\Psi - \sin\Phi\cos\Psi & \cos\Phi\cos\Theta \end{bmatrix}$$

- ***Wind Reference Frame***

The Wind Reference Frame, indicated with the subscript *W*, presents the X_W directed oppositely to the free-stream velocity, the z-axis perpendicular to X_W, in the plane of symmetry of the vehicle, and the Y_W axis completing the triad in a right-handed way. In Figure 10.2 the aerodynamic angles are also indicated, that is, the Angle of Attack of the vehicle (α), defined as the angle between the projection of the direction of the free-stream velocity on the xz plane of the body frame, and the X_B axis itself, and the Angle of Sideslip (β), defined as the angle between the free-stream velocity and the xz plane of the body frame. α is positive when the vehicle noses-up, whereas β is positive when the free-stream comes from the right side of the pilot.

The rotation matrix that allows to pass from the Wind Reference Frame to the Body Reference Frame is the following:
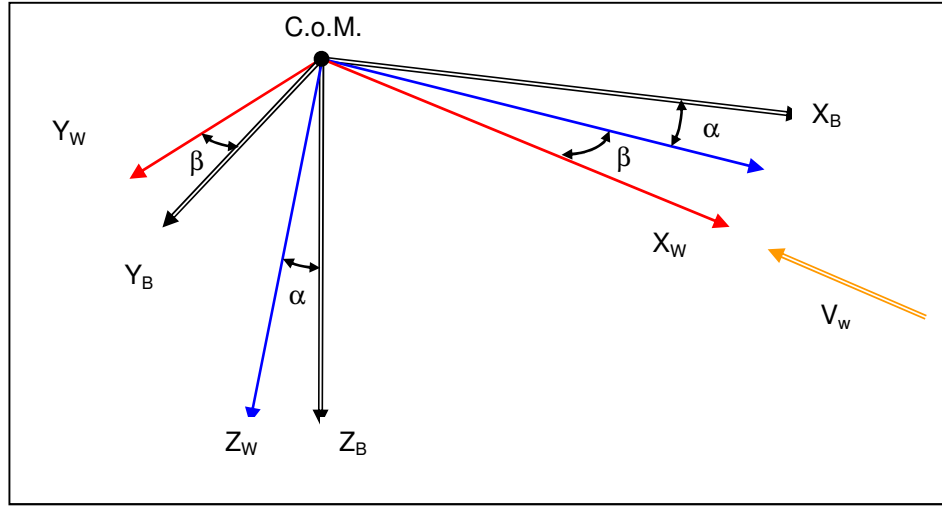
Figure 10.2 – Wind Reference Frame

$$\text{Eq. 132} \qquad \mathbf{R}_W^B = \begin{bmatrix} \cos\alpha\cos\beta & -\cos\alpha\sin\beta & -\sin\alpha \\ \sin\beta & \cos\beta & 0 \\ \sin\alpha\cos\beta & -\sin\alpha\sin\beta & \cos\alpha \end{bmatrix}$$

- ***Non-Rotating Shaft Reference Frame***

This Reference Frame is indicated with the subscript *S* and used for rotorcraft, only. Its centre is in the rotor hub, and can be obtained from the Body Reference Frame with a rotation i_θ around Y_B, followed by a rotation i_ϕ around the x-axis of the Reference Frame obtained after the first rotation, where i_θ and i_ϕ define the longitudinal and lateral tilt of the shaft with respect to the vehicle body axes.

The rotation matrix that allows to pass from the Body Reference Frame to the Non-Rotating Shaft Frame is the following:

$$\text{Eq. 133} \qquad \mathbf{R}_B^S = \begin{bmatrix} \cos i_\theta & 0 & -\sin i_\theta \\ \sin i_\theta \sin i_\varphi & \cos i_\varphi & \cos i_\theta \sin i_\varphi \\ \sin i_\theta \cos i_\varphi & \sin i_\varphi & \cos i_\theta \cos i_\varphi \end{bmatrix}$$
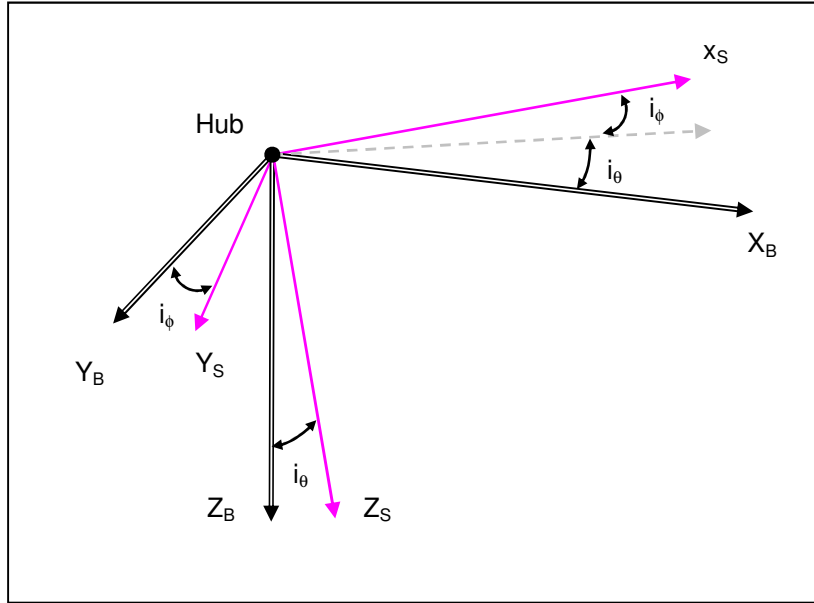
Figure 10.3 – Non-Rotating Shaft Reference Frame

- *Rotating Shaft Reference Frame*

This Reference Frame is indicated with the subscript *r* and used for rotorcraft, only. It is obtained starting from the Non-Rotating Shaft one with a $\pi/2-\psi$ rotation around Y_S, where ψ is the *Blade Azimuth Angle*, conventionally considered 0° when the blade is parallel to the tail of the vehicle, and measured in the direction of rotation.

The rotation matrix that allows to pass from the Non-Rotating Shaft Reference Frame to the Rotating Shaft Frame is the following:

$$\text{Eq. 134} \qquad \mathbf{R}_S^r = \begin{bmatrix} \sin\psi & \cos\psi & 0 \\ -\cos\psi & \sin\psi & 0 \\ 0 & 0 & 1 \end{bmatrix}$$

- *Multi-Blade Coordinates*

This coordinates system is introduced to compute the aerodynamic force produced by the rotor blades, consequently they are used for rotorcraft, only. The dynamics of a rotor system are periodic, using multi-blade coordinates an LTI approximation of these dynamics can be derived.

A periodic function can be fitted at several discrete points by using the discrete Fourier series. In the case of a helicopter rotor, these points are the azimuthal blade locations. Multi-blade coordinates use the N_b lowest Fourier coefficients, where N_b is the rotor's number of blades, to transform from rotor blade degrees of freedom in the rotating shaft reference frame to rotor disk modes in the non-rotating reference frame, while maintaining the total number of degrees of freedom. For example, the flap angle of the rotor blades are β_{f1}, β_{f2}, …, β_{fN}. The blade angles are transformed by the discrete Fourier series to the N_b non-rotating frame coefficients β_0, β_{1c}, β_{1s} …, β_{0d}, which represent the flapping modes of the rotor disk and are denoted as multi-blade coordinates. For $N_b = 4$, the following relation holds:

$$\text{Eq. 135} \qquad \begin{bmatrix} \beta_0 \\ \beta_{0d} \\ \beta_{1c} \\ \beta_{1s} \end{bmatrix} = \frac{1}{N_b} \begin{bmatrix} 1 & 1 & 1 & 1 \\ -1 & 1 & -1 & 1 \\ 2\cos\psi & 2\sin\psi & -2\cos\psi & -2\sin\psi \\ 2\sin\psi & -2\cos\psi & -2\sin\psi & 2\cos\psi \end{bmatrix} \begin{bmatrix} \beta_{f1} \\ \beta_{f2} \\ \beta_{f3} \\ \beta_{f4} \end{bmatrix}$$

The differential term β_{0d} only exists when there is an even number of blades. The multi-blade coordinates expansion of the flapping angle β_f will be given by

$$\text{Eq. 136} \qquad \beta_f(\psi) = \beta_0 + \beta_{1c}\cos\psi + \beta_{1s}\sin\psi$$

It is assumed that all of the rotor blades behave identically. Figure 10.4 illustrates the meaning of the multi-blade coordinates. The coning mode is represented by the collective coordinate β_0, whereas the longitudinal and lateral tilt modes are represented by the cyclic coordinates β_{1c} and β_{1s}, respectively.
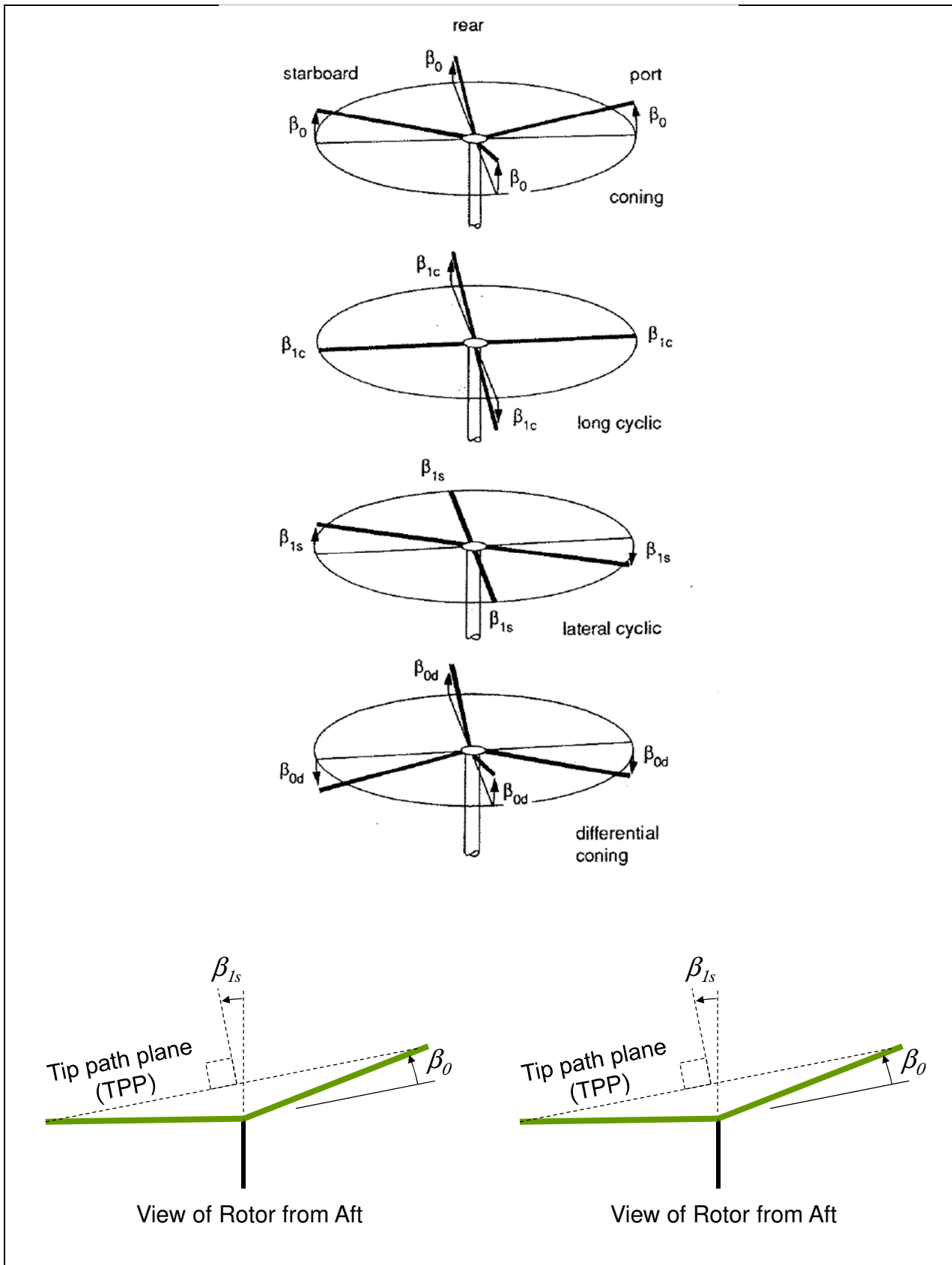
Figure 10.4 – Multi-blade coordinates system

11 AUTHOR REFERENCES

[AR1]   A. Vitale, F. Corraro, G. De Matteis, N. de Divitiis, *Identification from Flight Data of the Aerodynamics of an Experimental Re-entry Vehicle*, Advances in Modeling of Fluid Dynamics (ISBN 980-953-307-311-3), InTech, pp. 171-202, 2012.

[AR2]   A. Vitale, N. Genito, L. Garbarino, U. Ciniglio, F. Corraro, *A hybrid frequency-time domain technique for ground effect identification*, The Aeronautical Journal, Vol. 114, N° 1156, June 2010.

[AR3]   C. Lai, G. Cuciniello, F. Nebula, R. Palumbo, M. Russo, A. Vitale, F. Corraro, *A Stratospheric Balloon Integrated Navigation Facility*, Proceedings of 15th ESA Symposium on European Racket and Balloon Programmes and Related Research, Visby, Sweden, June 2007.

[AR4]   A. Vitale, U. Tancredi, L. Verde, E. Filippone, F. Corraro, *A Tool for Space Vehicle Uncertainty Ranges Estimation*, Proceedings of 55th International Astronautical Congress (IAC), Vancouver, Canada, October 2004.

[AR5]   G. Morani, F. Corraro, A. Vitale, *New Algorithm for Probabilistic Robustness Analysis in Parameter Space*, Journal of Aerospace Computing, Information, and Communication, Vol. 6, pp. 291-306, April 2009.

[AR6]   U. Tancredi, M. Grassi, F. Corraro, A. Vitale, E. Filippone, *A linear time varying approach for robustness analyses of a re-entry flight technology demonstrator*, Proceedings of the Institution of Mechanical Engineers, Part G, Journal of Aerospace Engineering, Vol. 226, N° 4, pp. 467-480, April 2012.

[AR7]   L. Garbarino, N. Genito, V. Baraniello, E. De Lellis, A. Vitale, *Low Cost Air Data System for UAV In-Flight Experimentation*, Proceedings of 23rd SFTE-EC Symposium, Amsterdam, The Netherlands, June 2012.

[AR8]   A. Vitale, N. Genito, L. Federico, F. Corraro, *Hybrid Approach for Rotorcraft Identification from Flight Data*, Proceedings of the 67th American Helicopter Society Annual Forum, Virginia Beach, VA, May 2011.

[AR9]   A. Vitale, F. Corraro, M. Bernard, G. De Matteis, *Unscented Kalman Filtering for Identification of a Re-entry Vehicle in Transonic Regime*, AIAA Journal of Aircraft, Vol. 46, No 5, pp. 1649-1659, September-October 2009.

[AR10] M. Bernard, G. De Matteis, F. Corraro, A. Vitale, *System Identification of a Sub-Orbital Re-entry Experimental Vehicle*, Proceedings of AIAA Atmospheric Flight Mechanics Conference, AIAA 2007-6719, Hilton Head, South Carolina, August 2007.

[AR11] A. Vitale, N. Genito, L. Federico, E. Filippone, F. Corraro, *Multi-Step Strategy for Rotorcraft Model Identification from Flight Data*, Proceedings of 21th SFTE (EC) Symposium, Vergiate, Itlay, October 2010.

[AR12] A. Vitale, F. Corraro, M. Bernard, G. De Matteis, *Identification of the Transonic Aerodynamic Model for a Re-entry Vehicle*, Proceedings of 15th IFAC Symposium on System Identification SYSID 2009, Saint-Malo, France, July 2009.

[AR13] A. Vitale, N. Genito, L. Federico, E. Filippone, U. Ciniglio, F. Corraro, *A Hybrid Time and Frequency Method for Rotorcraft Model Identification from Flight Data*, Proceedings of 29th IASTED International Conference on Modelling, Identification and Control (MIC 2010), Innsbruck, Austria, February 2010.

[AR14] N. de Divitiis, A. Vitale, *Fully Structured Aerodynamic Model for Parameter Identification of a Reentry Experimental Vehicle*, Journal of Spacecraft and Rockets (ISSN 0022-4560), Vol. 47, No 1, pp. 113-124, January-February 2010.

[AR15] A. Vitale, *Tool Avanzato di PFA per Missioni Sub-Transoniche*, CIRA-CF-07-1164, CIRA Internal Technical Report, 2007.

[AR16] F. Corraro, G. Cuciniello, G. Morani, F. Nebula, R. Palumbo, A. Vitale, *GNC Post Flight Analysis of the Italian Dropped Transonic Flight Tests*, Proceedings of IAF 63th International Astronautical Congress, Naples, Italy, October 2012.

[AR17] A. Vitale, F. Corraro, *Identification from Flight Data of the Italian Unmanned Space Vehicle*, Proceedings of 16th IFAC Symposium on System Identification SYSID 2012, Brussels, Belgium, July 2012.

[AR18] A. Vitale, L. Federico, E. Filippone, N. Genito, M. Russo, *Report Finale Progetto HeliIdent*, CIRA-CF-08-1495, CIRA Internal Technical Report, 2008.

[AR19] G. Morani, G. Cuciniello, F. Nebula, A. Vitale, R. Palumbo, *Post Flight Analysis of GNC Experiment for DTFT2 Mission*, CIRA-CF-11-0875, CIRA Internal Technical Report, 2011.

[AR20] A. Vitale, G. Cuciniello, F. Nebula, M. Russo, F. Corraro, *Post Flight Data Analysis of Guidance, Navigation and Control Experiment for DTFT1 Mission*, Proceedings of 2nd International ARA Days Conference, "10 Years After ARD", Arcachon, France, October 2008.

[AR21] F. Corraro, G. Cuciniello, E. Filippone, G. Morani, F. Nebula, M. Russo, A. Vitale, *CIRA Technologies and Flight Test Results for Innovative GN&C Systems in Terminal Area Energy Management*, Proceedings of 7th International ESA Conference on Guidance, Navigation & Control Systems, Tralee, County Kerry, Ireland, June 2008.

[AR22] F. Corraro, G. Cuciniello, G. Morani, F. Nebula, R. Palumbo, A. Vitale, *Advanced GN&C Technologies for TAEM: Flight Test Results of the Italian Unmanned Space Vehicle*, Proceedings of AIAA Guidance, Navigation, and Control Conference, Portland (OR), USA, Aug 2011.

[AR23] A. Vitale, G. Cuciniello, F. Nebula, M. Russo, *Post Flight Analysis of GNC Experiment for DTFT_1 Mission*, CIRA-CF-07-1282, CIRA Internal Technical Report, 2008.

12 BIBLIOGRAPHY

[B1]   R. V. Jategaonkar, *Flight Vehicle System Identification: A Time Domain Methodology*, AIAA Progress in Astronautics and Aeronautics, Reston, VA, 2006.

[B2]   M. B. Tischler, R. K. Remple, *Aircraft and Rotorcraft System Identification - Engineering Methods with Flight Test Examples*, AIAA Education Series, Reston, VA, 2006.

[B3]   K. C. Wang, K. W. Iliff, *Retrospective and Recent Examples of Aircraft Parameter Identification at NASA Dryden Flight Research Center*, Journal of Aircraft, Vol. 41, No. 4, pp. 752-764, July-August 2004.

[B4]   E. Warner, F. Norton, *Preliminary Report on Free Flight Tests*, NACA Report No. 70, 1919.

[B5]   E. A. Morelli, V Klein, *Application of System Identification to Aircraft at NASA Langley Research Center*, Journal of Aircraft, Vol. 42, No. 1, pp. 12-25, January-February 2005.

[B6]   P. G. Hamel, J. Kaletka, Advances in Rotorcraft System Identification, Progress in Aerospace Sciences, Vol. 33, No 3/4, pp. 259-294, 1997.

[B7]   C. A. A. M. van der Linden, J. A. Mulder, J. K. Sridhar, *Recent Developments in Aircraft Parameter Identification at Delft University of Technology - Optimal Input Design,* in Cook M. V. and Rycroft, M. J. (Eds), Aerospace Vehicle Dynamics and Control, Clarendon Press, Oxford, pp. 259-284, 1994.

[B8]   J. H. Breeman, H. Kannemans, M. Laban, *In-Flight Model Identification Research Aimed at Developing a Flight Simulator Model*, NATO Research and Technology Organization XI Symposium on System Identification for Integrated Aircraft Development and Flight Testing, Madrid, Spain, May 1998.

[B9]   J. J. Meijer, M. H. L. Hounjet, B. J. G. Eussen, B. B. Prananta, *NLR-TU Delft Experience in Unsteady Aerodynamics and Aeroelastic Simulation Applications*, in Numerical Unsteady Aerodynamics and Aeroelastic Simulation, AGARD R-822, Paper 11, March 1998.

[B10] D. Graham, D. T. McRuer, *Analysis of Nonlinear Control Systems*, Dover Publications, 1971.

[B11] M. B. Tischler, J. Kaletka, *Modeling XV-15 tilt-rotor aircraft dynamics by frequency and time-domain identification techniques*, AGARD, Rotorcraft Design for Operations, 1987.

[B12] R. Jategaonkar, F. Thielecke, *Evaluation of Parameter Estimation Methods for Unstable Aircraft*, Journal of Aircraft, Vol. 31, No. 3, pp. 510-519, 1994.

[B13] E. A. Morelli, *System Identification Programs for Aircraft (SIDPAC)*, Proceedings of AIAA Atmospheric Flight Mechanics Conference, Monterey (CA), August 2002.

[B14] P. Hamel, R. Jategaonkar, *Evolution of Flight Vehicle System Identification*, Journal of Aircraft, Vol. 33, No. 1, pp. 9-28, 1996.

[B15] C. L. Bottasso, F. Luraghi, G. Maisano, *Time-domain parameter estimation from flight test data for first-principle rotorcraft models*, Proceedings of XX AIDAA Congress, Milan, Italy, 2009.

[B16] R. E. Maine and K. W. Iliff, *Application of Parameter Estimation to Aircraft Stability and Control: The Output – Error Approach*, NASA, RP-1168, 1986.

[B17] K. W. Iliff, M. F. Shafer, *Extraction of Stability and Control Derivatives from Orbiter Flight Data*, NASA-TM-4500, June 1993.

[B18] M. Yanagihara, M. Shigemi, T. Suito, *Estimating Aerodynamics Characteristics of Automatic Landing Flight Experiment Vehicle Using Flight Data*, Journal of Aircraft, Vol. 36, No. 6, pp. 926-933, November-December 1999.

[B19] A. Abdulle, G. Wanner, *200 years of the least squares method*, Elemente der Mathematik, Vol. 57, pp. 45–60, Birkhauser Verlag, Basel, 2002.

[B20] R. K. Mehra, *Identification of Stochastic Linear Dynamics Systems Using Kalman Filter Representation*, AIAA Journal, Vol. 9, pp.28-31, January 1971.

[B21] L. Ljung, *Asymptotic Behavior of the Extended Kalman Filter as a Parameter Estimator for Linear Systems*, IEEE Trans. on Automatic Control, Vol. AC-24, No. 1, February 1979.

[B22] S. Brunke, M. E. Campbell, *Square Root Sigma Point Filtering for Real-Time, Nonlinear Estimation*, Journal of Guidance, Control and Dynamics, Vol. 27, No. 2, March-April 2004.

[B23] R. Van der Merwe, E. A. Wan, *The Square-Root Unscented Kalman Filter for State and Parameter-Estimation*, International Conference on Acoustic, Speech and Signal Processing, Salt Lake City, Utah, May 2001.

[B24] G. Chowdhary, R. Jategaonkar, *Aerodynamic Parameter Estimation from Flight Data Applying Extended and Unscented Kalman Filter*, AIAA-2006-6146 Proceedings of Atmospheric Flight Mechanics Conference and Exhibit, Keystone, Colorado, August 2006.

[B25] R. K. Mehra, *Optimal Inputs for Linear System Identification*, Preprints, JACC, Stanford, California, 1972.

[B26] E. A. Morelli, *Practical Input Optimization for Aircraft Parameter Estimation Experiments*, NASA-CR-191462, May 1993.

[B27] R. W. Borek, A. Pool, *Basic Principles of Flight Test Instrumentation Engineering*, AGARD AG-160, Vol. 1, No 2, March 1994.

[B28] H. Jonkers, *Application of the Kalman Filter to Flight Path Reconstruction from Flight Test Data Including Estimaiton of Instrumental Bias Error Corrections*, Ph. D. Thesis, Delft, 1976.

[B29] R. V. Jategaonkar, *Flight Vehicle System Identification – Engineering Utility*, Journal of Aircraft, Vol. 42, No. 1, January-February 2005.

[B30] B. Ninness, *Some System Identification Challenges and Approaches*, Proceedings of 15th IFAC Symposium on System Identification SYSID 2009, Saint-Malo, France, July 2009.

[B31]   R. E. Maine, K. W. Iliff, *The Theory and Practice of Estimating the Accuracy of Dynamic Flight-Determined Coefficients*, NASA-RP-1077, July 1981.

[B32]   S. J. Julier, J. K. Uhlmann, *New Extension of the Kalman Filter to Nonlinear Systems*, Proceedings of SPIE, Vol. 3068, pp. 182-193, 1995.

[B33]   E. A. Wan, R. van der Merwe, *The Unscented Kalman Filter for Nonlinear Estimation*, Proceedings of IEEE 2000 Adaptive Systems for Signal Processing, Communication and Control Symposium (AS-SPCC), Lake Louise, Canada, October 2000.

[B34]   M. C. Van Dyke, J. L. Schwartz, C. D. Hall, *Unscented Kalman Filtering for Spacecraft Attitude State and Parameter Estimation*, Proceedings of AAS/AIAA Space Flight Mechanics Meeting, Maui, Hawaii, February 2004.

[B35]   Y. Wu, D. Hu, M. Wu, X. Hu, *Unscented Kalman Filtering for Additive Noise Case: Augmented vs. Non-augmented*, Proceedings of American Control Conference, Portland, Oregon , June 2005.

[B36]   M. Bernard, G. De Matteis, *Sviluppo di una Metodologia Innovativa e Realizzazione di un Prototipo Software per l'Identificazione dei Parametri Aerodinamici di Velivoli Spaziali in Regime di Volo Subsonico, Transonico e Supersonico*, CIRA-CF-07-0034, CIRA Internal Technical Report, 2007.

[B37]   L. Ljung, *System Identification: Theory for the User*, Prentice Hall Inc, Englewood Cliffs, New Jersey, 1987.

[B38]   R. E. Maine, K. W. Iliff, *Identification of Dynamic Systems - Theory and Formulation*, NASA, RP-1138, 1985.

[B39]   E. A. Morelli, *Practical Aspects of the Equation-Error Method for Aircraft Parameter Estimation*, AIAA-2006-6144, AIAA Atmospheric Flight Mechanics Conference, Keystone Colorado, August 2006.

[B40]   E. A. Morelli, *Real-Time Parameter Estimation in the Frequency Domain*, Journal of Guidance, Control, and Dynamics, Vol. 23, No. 5, pp. 812-818, September-October 2000.

[B41] M. S. Smith, T. R. Moes, E. A. Morelli, *Real-Time Stability and Control Derivative Extraction Form F-15 Flight Data*, NASA/TM-2003-212027, September 2003.

[B42] R. Larsson, M. Enqvist, *Sequential Aerodynamic Model Parameter Identification*, Proceedings of 16th IFAC Symposium on System Identification SYSID 2012, Brussels, Belgium, July 2012.

[B43] A. Kornienko, *System Identification Approach for Determining Flight Dynamical Characteristics of an Airship from Flight Data*, Ph.D. thesis, University of Stuttgart, 2006.

[B44] B. Etkin, *Dynamics of Atmospheric Flight*, John Wiley & Sons, Inc, 1972.

[B45] B. L. Stevens, F. L. Lewis, *Aircraft Control and Simulation (2nd Ed.)*, John Wiley & Sons Inc., ISBN 0 471371459, Hoboken, New Jersey, 2003.

[B46] G. D. Padfield, *Helicopter Flight Dynamics*, Blackwell, 1996.

[B47] W. Johnson, *Helicopter Theory*, Princeton University Press, 1957.

[B48] N. K. Gupta, W. E. Jr. Hall, *System Identification Technology for Estimating Re-entry Vehicle Aerodynamic Coefficient*, Journal of Guidance and Control, Vol. 2, No. 2, pp. 139-146, March-April 1979.

[B49] V. Klein, J. C. Batterson, P. C. Murphy, *Determination of Airplane Model Structure From Flight Data by Using Modified Stepwise Regression*, NASA-TP-1916, 1981.

[B50] T. L. Trankle, S. D. Bachner, *Identification of a Nonlinear Aerodynamic Model of the F-14 Aircraft*, Journal of Guidance, Control, and Dynamics, Vol. 18, No. 6, pp. 1292-1297, November-December 1995.

[B51] N. K. Gupta, W. E. Jr. Hall, T. L. Trankle, *Advanced Methods of Model Structure Determination from Test Data*, Journal of Guidance and Control, Vol. 1, No. 3, pp. 197-204, May-June 1978.

[B52] H. Lamb, *On the Motion of Solids Through a Liquid*, Hydrodynamics (6th Ed.), Dover, New York, 1945.

[B53] G. J. Brauckmann, *X-34 Vehicle Aerodynamic Characteristics*, Journal of Spacecraft and Rockets, Vol. 36, No. 2, pp. 229-239, March-April 1999.

[B54] H. Kawato, S. Watanabe, Y. Yamamoto, K. Fujii, *Aerodynamic Performances of Lifting-Body Configurations for a Reentry Vehicle*, Journal of Spacecraft and Rockets, Vol. 42, No. 2, pp. 232-239, March-April 2005.

[B55] D. P. Rayme, *Aircraft Design: A Conceptual Approach*. AIAA, Reston, VA, 1996.

[B56] F. B. Hildebrand, *Introduction to Numerical Analysis*, Dover, New York, 1987.

[B57] G. C. Rufolo, P. Roncioni, M. Marini, R. Votta, S. Palazzo, *Experimental and Numerical Aerodynamic Data Integration and Aerodatabase Development for the PRORA-USV-FTB_1 Reusable Vehicle*, Proceedings of 4th AIAA/AHI Space Plane and Hypersonic Systems and Technologies Conference, Canberra, Australia, November 2006.

[B58] J. C. Hoff, M. V. Cook, *Aircraft Parameter Identification Using an Estimation-Before-Modelling Technique*, The Aeronautical Journal, Vol. 100, No. 997, pp. 259-268, August-September 1996.

[B59] R. A. Singer, *Estimating Optimal Tracking Filter Performance for Manned Maneuvering Targets*, IEEE Transactions on Aerospace and Electronic Systems, Vol. AES-6, No. 4, July 1970.

[B60] A. Gelb, *Applied Optimal Estimation*, M.I.T. Press, ISBN 0-262-20027-9, Cambridge, Massachusetts, 1989.

[B61] *WGS 84 TECHNICAL REPORT*, National Imagery and Mapping Agency (NIMA) Technical Report 8350.2, Third Edition, July 1997.

[B62] P. Berrisford, D. Dee, P. Poli, R. Brugge, K. Fielding, M. Fuentes, P. Kallberg, S. Kobayashi, S. Uppala, A. Simmons, *The ERA Interim Archive*, European Centre for Medium Range Weather Forecasts October 2011.

[B63] E. A. Morelli, V. Klein, *Accuracy of Aerodynamic Model Parameters Estimated from Flight Test Data*, Journal of Guidance, Control, and Dynamics, Vol. 20, No. 1, pp. 74-80, January–February 1997.

[B64] G. A. Ouellette, *Modeling the OH-6A using FLIGHTLAB and Helicopter Simulator Considerations*, M.Sc. Thesis, US Navy Postgraduate School, Monterey, 2002.

[B65] U. Ciniglio, F. Ferrara, *HELIDYN: un Modello, basato sul codice ARMCOP, per la Simulazione di Dettaglio della Dinamica dell'Elicottero*, CIRA-TR-95-0033, CIRA Internal Technical Report, 1995.

[B66] P. G. Hamel, *Advanced in Aerodynamics Modeling for Flight Simulation and Control Design*, International Association of Applied Mathematics and Mechanics: GAMM-Mitteilungen, Wiley-VCH, Berlin, Vol.23, No.1-2, 2000.

[B67] J. W. Fletcher, *Identification of UH-60 Stability Derivatives Models in Hover from Flight Test Data*, Journal of the American Helicopter Society, Vol. 40, No. 1, 1995.

[B68] M. Rohlfs, W. V. Grunhagen, J. Kaletka, *Nonlinear Rotorcraft Modeling and Identification*, RTO SCI Symposium on System Identification for Integrated Aircraft Development and Flight Testing, Madrid, Spain, May 1998.

[B69] J. A. Grauer, J. K. Conroy, Jr. J. E. Hubbard, D. J. Pines, *System Identification of a Miniature Helicopter*, AIAA-2008-6898, Proceedings of Atmospheric Flight Mechanics Conference and Exhibit, Honolulu, Hawaii, August 2008.

[B70] K. Hui, R. Srinivasan, *The Inclusion of Higher-Order Rotor Dynamics To Improve the Dynamic Model Of a Single Rotor Helicopter in Hover*, RTO SCI Symposium on System Identification for Integrated Aircraft Development and Flight Testing, Madrid, Spain, May 1998.

[B71] M. A. Lawler, C. M. Ivler, M. B. Tischler, Y. B. Shtessel, *System Identification of the Longitudinal/Heave Dynamics for a Tandem-Rotor Helicopter Including Higher-Order Dynamics*, AIAA-2006-6147 Proceedings of Atmospheric Flight Mechanics Conference and Exhibit, Keystone, Colorado, August 2006.

[B72] B. Mettler, T. Kanade, M. B. Tischler, *System Identification Modeling of a Model-Scale Helicopter*, Technical Report CMU-RI-TR-00-03, Robotics Institute, Carnegie Mellon University, Pittsburgh, January, 2000.

[B73] J. J. Howlett, *UH-60 Black Hawk Engineering Simulation Program: Volume I - Mathematical Model*, NASA-CR-166309, 1981.

[B74] R. T. N. Chen, *A Survey of Nonuniform Inflow Models for Rotorcraft Flight Dynamics and Control Applications*, NASA-TM-102219, 1989.